THE BPM DESIGN OPTIMIZATION AND IMPLEMENTATION OF 3-BRANCH WAVEGUIDE DEVICES

by

Michael A. Sekerka-Bajbus, rmc, B.Eng.(RMC)

Department of Electrical Engineering
McGill University
Montréal, Québec

July 1989

A thesis submitted to the Faculty of Graduate Studies and Research in partial fulfillment of the requirements for the degree of Master of Engineering.

ABSTRACT

The *Beam Propagation Method* (BPM) together with an accurate *Effective Index* model is used as a Computer Aided Design (CAD) tool for the analysis, design and optimization of integrated optical devices. The performance of both active and passive 3-branch $Ti:LiNbO_3$ waveguide devices as a function of various design parameters is investigated. Then, the device design required to match a specified performance is deduced, and the theoretical performance predictions are verified experimentally through device fabrication and measurements.

In particular, a 3-branch passive power divider, a linear mode confinement modulator, and an active 3-branch switch were studied through their design and implementation. The theoretically predicted performance parameters were found to agree well with the measured values.

RESUME

La méthode de propagation par rayon (BPM), employeé de paire avec un model précis d'index effectifs, est utilisée comme outil de conception assistée par ordinateur (CAD) pour l'analyse et l'optimisation de systèmes optiques intégrés. La performance de guides d'ondes à trois branches, actifs et passifs, est explorée en fonction de divers paramètres de construction. A partir de ceci, le design du système requis pour satisfaire la performance désirée est déduit, et les prédictions théoretiques de sa performance sont vérifiées expérimentalement. Plus spécifiquement, la conception d'un diviseur de puissance passif à trois branches, d'un modulateur à confinement de modes lineaires, et d'un commutateur actif a trois branches ont été étudiés.

ACKNOWLEDGEMENTS

I would like to express my gratiude to my supervisor, Professor Gar Lam Yip, for his guidance and encouragements during my studies, and for revising the first draft of this thesis.

I am especially grateful to Dr. Nobuo Goto, now with Toyohashi University, Japan, for his encouragement, and for teaching me the device fabrication techniques used in the experimental work described in this thesis.

I would also like to thank Dr. Kiyoshi Kishioka for the help received in the completion of this work.

I am grateful to Mr. K. Fraser for giving me access to "Opus" and "Odie", the two micro-vax computers in the Undergraduate Computer Laboratory, which were used to do the horrendous amount of 'number crunching' required for the BPM simulations.

I must also thank my fellow students for their encouragement and many fruitful discussions. In particular, the contributions from Peter C. Noutsios, John Nikolopoulos, Jeffrey Yu, Feng Xiang, and Jian-Yao Chen are gr atefully acknowledged.

Both the technical and secretarial staff provided me with their always friendly services and helped solve the ever occuring administrative problems.

This research was supported financially by the Natural Sciences and Engineering Research Council of Canada (NSERC) through a post-graduate scholarship, an operating grant, and a strategic grant.

TABLE OF CONTENTS

INTRODUCTION TO INTEGRATED OPTICS

The recent evolution of advanced fiber-optical communication with its emphasis on high data rate single-mode fiber transmission systems has established a need for guided wave devices to actively control various physical parameters of the light propagating in the fiber, or else control the route the light is taking in the system. Examples are the requirement for high speed, large bandwidth modulators, switches, mode splitters, wavelength demultiplexers, frequency shifters, polarization controllers, and tunable filters. Such functions can be realized off-fiber with optical waveguide components which appear like miniaturized microwave guiding circuits, imitating the light propagating properties of optical fibers. For this purpose, channels of a higher refractive index confine the optical waves in the substrate and guide them through the device. By using electro-optical substrates, the light in these channels can be phase or intensity modulated, or switched into other paths. This technology is commonly referred to as *Integrated Optics* (IO), the name implying the optical equivalent of electronic or microwave integrated circuits [1].

Three types of materials are currently used in integrated optical applications: Semi-conductor crystals, Inorganic oxide crystals, and organic polymers. Of these, only lithium niobate ($LiNbO_3$) components have reached a high level of development with respect to device fabrication technology, packaging, fiber coupling, and device performance [2]. This has led to a (at this stage) small number of integrated optical devices being commercially available. The product lines offered usually cover devices such as phase modulators, Mach-Zehnder intensity modulators, directional coupler switches, and switching arrays of various complexity [3]. Modulation bandwidths above 10GHz and cross-talk values of >20dB in switches with drive voltages of 10V are typical performance specifications. These devices are available for operating wavelengths of 850nm to 1500nm, and come pig-tailed with polarization maintaining single-mode fibers.

The emergence of commercial integrated optical devices in the last three years can, in part, be attributed to a better understanding of both the fabrication techniques and the light guiding behavior of complex IO structures. Waveguide fabrication in $LiNbO_3$ is dominated by titanium in-diffusion. Other fabrication processes such as proton exchange [4] and ion-implantation [5] have not reached the same level of development. Waveguiding structures in the substrate can be formed from complex patterns of evaporated titanium (Ti) by thermal in-diffusion of these metal patterns into the crystal. Titanium in-diffusion into $LiNbO_3$ has been extensively characterized [6-8]. Additional studies, such as on wavelength dispersion of the refractive index change [9], have recently improved our understanding of this process.

Electrode materials and fabrication also strongly influence the performance and stability (dc-drift) of electro-optic devices. To avoid light absorption by the metal electrodes, a lower-index buffer layer is generally used to separate them from the crystal surface. The material properties of the buffer layer, commonly made of SiO_2, also influence the stability of the device [10]. The fabrication of drift free devices, however, still poses some difficulties. Transparent indium-tin-oxide electrodes, which do not require a buffer layer, have recently been used to improve device performance and stability [11].

Parallel to progress in material and fabrication technology, new device modelling techniques have improved our understanding of complex integrated optical structures and their light guiding behavior. The classical approach to describing the light propagating characteristics of IO devices is based on the *Coupled Mode theory* [12,13]. Other approaches, such as perturbation methods [14], variational methods [15], local guided modes [16], transverse resonance techniques [17] or finite element analysis [18], have also been used. Simple approximate treatments of the waveguide problem such as the *WKB* [19], the *Effective Index* [20], and the *Equivalent Step-index Methods* [21] have also been successfully employed.

These methods are usually sufficient to reveal the fundamental device properties. They are, however, often insufficient to analyze complex waveguide and electrode structures. More recently, a new device modelling technique based on the *Effective Index Method* and the *Beam Propagation Method* (BPM) has been used to accurately simulate IO devices. The BPM algorithm, originally developed to describe laser beam propagation in the atmosphere [22] and later very successfully used to analyze multi-mode fibers [23-25], permits a unified treatment of both guided and radiation modes in weakly guiding waveguides. It is thus ideally suited to analyzing complicated waveguide structures (e.g. couplers, waveguide bends, gratings) [26-28] and has recently been used for the design oriented analysis and optimization of IO devices [2].

A novel method to accurately calculate the electric field created by complex electrode configurations, accounting for the presence of a low-index buffer layer, has also improved the modelling of electro-optic devices [29].

Progress in fiber pig-tailing techniques [30] and packaging of $LiNbO_3$ devices [31] has not been as rapid as in other aspects of integrated optics, and continued research in these areas will be essential to a successful commercial exploitation of IO technology.

Although the main application of integrated optics was originally considered to be in advanced communication systems, it has also had a substantial impact on the area of advanced signal processing [32] and of sensors [31,33,34]. In particular, the realization of fiber-optic gyroscopes, employing IO components, for aircraft navigation systems, and the use of IO technology to overcome electro-magnetic interference problems in phased-array radars are being investigated.

Chapter Description

The feasibility of active and passive 3-branch waveguide devices in $Ti:LiNbO_3$ was established by M. Bélanger in 1986 [35]. The theoretical model used in his work was based on a field matching technique which was sufficient to reveal the fundamental device properties. However, quantitative agreement between experimental and theoretical results could not be established.

The goal of this thesis is to establish a more sophisticated theoretical design tool for the design oriented analysis and optimization of integrated optical devices. Such a tool is necessary for a successful commercial exploitation of IO technology. This is realized by using the novel *Beam Propagation Method* together with an accurate *Effective Index* modelling of the IO structure. The modelling of active devices is further improved by using a new approach to solving the electrode problem which accounts for the attenuating effect of the low-index buffer layer between the metal electrodes and the substrate surface on the electric field. This BPM design approach is extremely flexible and can very easily be adapted to simulate a large variety of IO devices. It can consequently be considered the core of a Computer Aided Design (CAD) tool for future use in our laboratory. In particular, the ability to accurately study the performance of IO devices is useful before actually proceeding to an experimental (and costly) investigation of a proposed device design.

The accuracy of this new design method will be established by optimizing active and passive 3-branch waveguide devices for single-mode operation, with the aim of improving on the experimental results achieved by M. Bélanger. In particular, design analysis and optimization results for a passive 3-branch power divider, a linear mode confinement modulator, and an active 3-branch switch are presented.

The thesis is organized in the following manner. Chapter I describes the Beam Propagation Method. The Effective Index model and the novel approach to solving the electrode problem are presented in Chapter II, and integrated with the BPM. The design optimization procedure is also described. In Chapter III, the accuracy of the BPM approach is established by comparing the theoretical performance predictions of a passive 3-branch power divider with previously published experimental results. Chapters IV and V describe the design optimization and the experimental verification of a ridge waveguide linear mode confinement modulator and a 3-branch active optical switch. Good qualitative and quantitative agreement between theory and experiment was established. Chapters III, IV, and V are slightly expanded versions of papers submitted for publication. References and Figures are included at the end of each Chapter. The experimental techniques used in fabricating the devices are described in detail in references [35] and [36]. A brief review of the whole work, together with comments on the future use of the BPM are presented in the conclusion.

References:

1 Miller,S.E., 'Integrated Optics: an introduction,' *Bell Syst. Tech. J.*, 48, pp.2059, 1969.

2 Thylén, L., 'Integrated Optics in LiNbO3: Recent developments in devices for telecommunications' *J. Lightwave Techn.*, LT-6, 6, pp. 847-861, 1988.

3 Becker, R.A., 'Commercially available integrated optics products and services,' *Proc. S.P.I.E. Integrated Optical Circuit Engineering VI*, 993, pp. 246-250, 1988.

4 Wong, K.K., 'Integrated optical waveguides and devices fabricated by proton exchange: a review,' *Proc. S.P.I.E. Integrated Optical Circuit Engineering VI*, 993, pp. 13-25, 1988.

5 Destefanis, G.L., Gailliard, J.P., Ligeon, E.L., Valette, S., Farmery, B.W., Townsend, P.D., and Perez, A., 'The formation of waveguides and modulators in LiNbO3 by ion-implantation,' *J. Appl. Phys.*, 50, p.7898, 1978.

6 Minakata, M., Saito, S., Shibata, M., and Miyazawa, S., 'Precise determination of refractive index changes in Ti-diffused LiNbO3 optical waveguides,' *J. Appl. Phys.*, 49, pp. 4677-4682, 1978.

7 Burns, W.K., Klein, P.H., and West, E.J., 'Ti diffusion in Ti:LiNbO3 planar and channel optical waveguides,' *J. Appl. Phys.*, 50, pp.6175-6182, 1979.

8 Naitoh, H., Nunoshita, M., and Nakayama, T., 'Mode control of Ti-diffused LiNbO3 slab optical waveguides,' *App. Optics*, 16, pp. 2546-2549, 1977.

9 Fouchet, S., Carenco, A., Daguet, C., Guglielmi, R., and Riviere, L., 'Wavelength dispersion of Ti induced refractive index change in LiNbO3 as a function of diffusion parameters,' *J. Lightwave Techn.*, LT-5, 5, pp. 700-708, 1987.

10 Yamada, S., and Minakata, M., 'DC drift phenomena in LiNbO3 optical waveguide devices,' *Japan. J. Phys.*, 20, pp. 733-737, 1981.

11 Gee, C.M., Thurmond, G.D., Blauvelt, H., and Yen, H.K., 'Minimizing dc drift in LiNbO3 devices,' *Appl. Phys. Lett.*, 47, pp.211-213, 1985.

12 Marcatili, E., 'Improved coupled mode equations for dielectric waveguides,' *IEEE J. Quant. Electr.*, QE-22, pp. 988-993, 1986.

13 Hardy, A. and Streifer, W., 'Coupled mode theory of parallel waveguides,' *J. Lightwave Techn.*, LT-3, pp. 1135-1147, 1985.

14 Thylén, L. and Stensland, L., 'Electrooptic approach to an integrated optics spectrum analyzer,' *Appl. Optics*, 20, 10, pp.1825-1832, 1981.

15 Sharma, A., Sharma, E., Goyal, I.C., and Ghatak, A.K., 'The variational technique for diffused directional couplers,' *Opt. Commun.*, 34, pp.39-42, 1980.

16 Thurston, R.N., Kapon, E., and Siberberg, Y., 'Analysis of mode separation in multi-channel branching waveguides,' *IEEE J. Quantum Electron.*, QE-23, pp. 1245-1255, 1987.

17 Ctyroky, J., Hofman, M., Janta, J., and Schrofel, J., '3-D analysis of $LiNbO_3$:Ti channel waveguides and directional couplers,' *IEEE J. Quantum Electron.*, QE-20, pp. 400-409, 1984.

18 Goel, K., Wooten, E.. and Chang, W.S.C., 'Design considerations for low switching voltage crossing channel switches,' *J. Lightwave Techn.*, LT-6, 6, pp. 881-885, 1988.

19 Suhara, T., Handa, Y., Nishihra, H., and Koyama, J., 'Analysis of optical channel waveguides and directional couplers with graded-index profiles,' *J. Opt. Soc. Amer.*, 69, pp.807-815, 1979.

20 Hocker, G.B., and Burns, W.K.. 'Mode dispersion of diffused channel waveguides by the effective index method,' *Appl. Opt.*, 16, 1, pp.113-118, 1977.

21 Marcatili, E., 'Dielectric rectangular waveguide and directional coupler for integrated optics,' *Bell. Syst. Tech. J.*, 48, pp. 2071-2073, 1969.

22 Fleck, J.A., Morris, J.R., and Feit, M.D., 'Time-dependent propagation of high energy laser beams through the atmosphere,' *Appl.Phys.*, 10, pp.129-160, 1976.

23 Feit, M.D., and Fleck, J.A., 'Light propagation in graded-index fibers,' *Appl. Optics*, 17, 24, pp.3990-3998, 1978.

24 Feit, M.D., and Fleck, J.A., 'Calculation of dispersion in graded-index multimode fibers by a propagating-beam method,' *Appl. Optics*, 18, 16, pp.2843-2851,1979.

25 Feit, M.D., and Fleck, J.A., 'Mode properties and dispersion for two optical fiber-index profiles by the propagating beam method,' *Appl. Optics*, 19, 18, pp.2240-2246, 1980.

26 Yevick, D. and Thylén, L., 'Analysis of gratings by the beam-propagation method,' *J. Opt. Soc. Amer.*, 72, pp.1084-1089, 1982.

27 Beats, R. and Lagasse, P.E., 'Calculation of radiation loss in integrated-optic tapers and Y-junctions,' *Appl. Optics*, 21, pp. 1972-1978, 1982.

28 Neyer, A., Mevenkamp, W., Thylén, L., and Lagerström, B., 'A BPM analysis of active and passive waveguide crossings,' J. Lightwave *Techn.*, LT-3, pp. 635-642, 1985.

29 Thylén, L. and Granestrand, P., 'Integrated Optic electrooptic device electrode analysis: the influence of buffer layers,' *J. Opt. Commun.*, 7, 1, pp. 11-14, 1986.

30 Murphy, E.J., 'Fiber attachment for guided wave devices,' *J. Lightwave Techn.*, LT-6, 6, pp.862-871, 1988.

31 Lawrence, M., Booth, R.C., and Beaumont, A.R., 'Some practical applications of $LiNbO_3$ integrated optics technology,' *Proc. S.P.I.E. Integrated Optical Circuit Engineering VI*, 993, pp. 246-250, 1988.

32 Taylor, H.F., 'Application of guided-wave optics in signal processing and sensing,' *Proc. IEEE*, 75, 11, pp. 1524-1535, 1987.

33 Bergh, R.A., Lefevre, H.C., and Shaw, H.J., 'An overview of fiber-optic gyroscopes,' *J. Lightwave Techn.*, LT-2, 2, pp. 91-107, 1984.

34 Bristow, J.P.G., Wey, A.C.T., Keur, M., Lukas, G., Ott, D.M., and Sriram, S., 'Integrated Optical circuit engineering for optical gyroscopes,' *Proc. S.P.I.E. Integrated Optical Circuit Engineering V*, 835, pp. 272-277, 1987.

35 Bélanger, M., *Theoretical and Experimental studies on active and passive 3-branch waveguides and their derivatives*, Ph.D. Thesis, Dept. of Elec. Eng., McGill University, Montréal, Canada, 1986.

36 Masuda, M. and Yip, G.L., *Fabrication techniques of thin film optical waveguides using McGill facilities*, Dept. of Elec. Eng., McGill University, Montréal, Canada, 1980.

CHAPTER I. DEVELOPMENT OF THE BEAM PROPAGATION METHOD

I-1. Introduction

In 1976, M.D. Feit and J.A. Fleck proposed a new algorithm for solving the scalar Helmholtz equation [1]. This algorithm, which was originally developed to describe laser beam propagation in the atmosphere and later successfully used to analyze multi-mode fibers, has since become known as the *Beam Propagation Method* (BPM). It permits a unified treatment of both the guided and the radiation modes in weakly guiding waveguides. More recently, this method has also been applied to the analysis and design of integrated optical devices.

There are currently two formulations of the BPM. The first, more commonly used one, is based on the *Parabolic* or *Fresnel approximation* of the scalar Helmholtz equation. It can be applied to problems in which the optical fields vary slowly along the propagation direction in distances of the order of a wavelength. A similar form of the BPM can be developed from the full scalar Helmholtz equation for problems where the Fresnel approximation is not valid. In most applications, however, both formuations yield the same physical results.

In the following sections, the two formulations of the Beam Propagation Method will be derived and their numerical implementation discussed.

I-2. The BPM based on the Fresnel equation

Consider the propagation of a single frequency light beam in an optical fiber. For weak guidance, the field in the fiber is satisfied by the scalar Helmholtz equation

$$\frac{\partial^2 \mathcal{E}}{\partial x^2} + \frac{\partial^2 \mathcal{E}}{\partial y^2} + \frac{\partial^2 \mathcal{E}}{\partial z^2} + \frac{\omega^2}{c^2} n^2 \mathcal{E} = 0, \qquad (I.1)$$

where $\mathcal{E}(x,y,z,t) = \mathcal{E}(\omega,x,y,z)\ \exp(i\omega t)$ is the electric field at angular frequency ω (the time dependence of the field will be implied in the following); c the speed of light in a vacuum, and $n(x,y,z,\omega)$ the refractive index at point $\mathbf{x}=(x,y,z)$.

The following discusses the solution method proposed by M.D. Feit and J.A. Fleck [1] for solving (I.1) when $n(\mathbf{x})$ has small variations from a reference value n_0 (typically the refractive index of the fiber cladding):

$$n(\omega,\mathbf{x}) \approx n_0.$$

Let the field at the entry to the fiber (z=0) be given by

$$\mathcal{E}(x,y,0) = \mathcal{E}_0(x,y)$$

which satisfies the radiation condition at $+\infty$, and consider a solution of (I.1) in the form

$$\mathcal{E}(\mathbf{x},\omega) = E(\mathbf{x},\omega)\ \exp(-ikz), \qquad (I.2)$$

where

$$k = \frac{\omega}{c} n_0. \qquad (I.3)$$

The amplitude function $E(\mathbf{x},\omega)$ is assumed to vary slowly with z (with respect to the wavelength λ). Substituting (I.2) into (I.1) results in

$$-2ik \frac{\partial E}{\partial z} + \frac{\partial^2 E}{\partial z^2} + \Delta_\perp E + \frac{\omega^2}{c^2} (n^2 - n_0^2)\ E = 0, \qquad (I.4)$$

where $\Delta_\perp$ denotes the traverse Laplacian, and

$$\begin{cases} E(x,y,0) = E_0(x,y) = \mathcal{E}_0(x,y); \\ E(x,y,z) \text{ satisfies the radiation condition at } z=+\infty \end{cases} \quad (I.5)$$

are applicable boundary conditions.

If we neglect the $\frac{\partial^2 E}{\partial z^2}$ term in equation (I.4) due to the slow variation of E with respect to z, we get the classical *parabolic* or *Fresnel approximation* of the scalar Helmholtz equation:

$$-2ik \frac{\partial E}{\partial z} + \Delta_\perp E + \frac{\omega^2}{c^2} (n^2 - n_0^2)\, E = 0,$$

$$-2ik \frac{\partial E}{\partial z} + \Delta_\perp E + k^2(n^2/n_0^2 - 1)\, E = 0. \quad (I.6)$$

Taking $E(x,y,z_n)$ to be the complete solution of (I.6) at $z=z_n$, then E at $z_{n+1} = z_n + \Delta z$ may be obtained formally by integration with respect to z:

$$\frac{\partial E}{\partial z} = -\frac{i}{2k} \left[\Delta_\perp + k^2(n^2/n_0^2 - 1) \right] E ,$$

$$\int_{z_n}^{z_n + \Delta z} \frac{dE}{E} = -\frac{i}{2k} \int_{z_n}^{z_n + \Delta z} \left[\Delta_\perp + k^2(n^2/n_0^2 - 1) \right] dz,$$

$$E(z_n + \Delta z) = \exp\left\{ -\frac{i}{2k} \left[\Delta z\, \Delta_\perp + \int_{z_n}^{z_n + \Delta z} k^2(n^2/n_0^2 - 1)\, dz \right] \right\} E(z_n). \quad (I.7)$$

If we define the operator

$$\delta\bar{n} = \frac{1}{\Delta z} \int_{z_n}^{z_n + \Delta z} k^2(n^2/n_0^2 - 1)\, dz, \quad (I.8)$$

then the solution (I.7) at $z=\Delta z$ can be replaced to second order accuracy with the symmetrized split operator form (see Appendix I-1)

$$E(x,y,\Delta z) = \exp\left[-\frac{i}{4k}\Delta z\ \Delta_\perp\right]\exp\left[-\frac{i}{2k}\Delta z\ \delta\bar{n}\right]\exp\left[-\frac{i}{4k}\Delta z\ \Delta_\perp\right]E(x,y,0). \tag{I.9}$$

Thus, the algorithm for propagating a field through a medium of index $n(x,\omega)$ consists of first propagating the field over a distance $\Delta z/2$ in a homogeneous medium of index n_0, i.e., solving the equation

$$\frac{\partial E}{\partial z} = -\frac{i}{2k}\Delta_\perp E \tag{I.10}$$

which has the solution

$$E(x,y,\Delta z/2) = \exp\left[-\frac{i}{4k}\Delta z\ \Delta_\perp\right]E(x,y,0),$$

then incrementing the phase according to the change in refractive medium, which is equivalent to solving

$$-2ik\frac{\partial E}{\partial z} + k^2(n^2/n_0^2 - 1)\ E = 0, \tag{I.11}$$

and completing the sequence by propagating the field a further $\Delta z/2$. At each step the initial condition is the terminal condition of the previous one. Equation (I.10), i.e. steps 1 and 3, can be solved by Fourier transform with respect to (x,y), while step 2 is an ordinary differential equation.

Although, to order Δz^3 (see Appendix I-1), no approximations have been made to obtain (I.9), the Fresnel equation is only an approximation to the full scalar wave equation. The propagation algorithm given above is only valid for fields which vary slowly along the propagation direction in distances of the order of a wavelength. For applications where this condition cannot be satisfied, an equivalent BPM algorithm, based on the full scalar Helmholtz equation but containing some additional approximations, has to be used. This second formalism of the BPM will be presented in the following section.

I-3. The BPM based on the full scalar Helmholtz equation

A beam propagation algorithm based on the full scalar Helmholtz equation can be derived in the following manner [2]. Consider again a single frequency light beam propagating in a weakly guiding optical fiber. If we rewrite the scalar wave equation (I.1) as

$$\frac{\partial^2 \mathcal{E}}{\partial z^2} + \left[\Delta_\perp + (\frac{\omega}{c} n)^2\right] \mathcal{E} = 0, \tag{I.12a}$$

then the solution of (I.12a) at z=Δz can be expressed formally as:

$$\mathcal{E}(x,y,\Delta z) = \exp\left[\pm i\ \Delta z \left[\Delta_\perp + (\frac{\omega}{c} n)^2\right]^{1/2}\right] \mathcal{E}(x,y,0), \tag{I.12b}$$

where $\Delta_\perp$ denotes the transverse Laplacian.

The square root in equation (I.12b) can be rewritten in the form

$$\left[\Delta_\perp + (\frac{\omega}{c} n)^2\right]^{1/2} = \frac{\Delta_\perp}{\left[\Delta_\perp + (\frac{\omega}{c} n)^2\right]^{1/2} + \frac{\omega}{c} n} + (\omega/c)\ n. \tag{I.13}$$

If $n=n(\omega,\mathbf{x})$ in the first right-hand term of equation (I.13) is replaced with the reference value n_o, (I.13) becomes

$$\left[\Delta_\perp + (\frac{\omega}{c} n)^2\right]^{1/2} \cong \frac{\Delta_\perp}{(\Delta_\perp + k^2)^{1/2} + k} + k + k\ [(n/n_o) - 1] \tag{I.14}$$

with

$$k = \frac{\omega}{c} n_o. \tag{I.15}$$

With the time dependence of $\mathcal{E}(\omega,\mathbf{x})$ implied, the electric field can again be expressed as

$$\mathcal{E}(\mathbf{x},\omega) = E(\mathbf{x},\omega)\ \exp\ (-ikz), \tag{I.16}$$

and substituting this expression in equation (I.12b) and using the above approximation yields

$$E(x,y,\Delta z) = \exp\left\{\pm i\ \Delta z \left[\frac{\Delta_\perp}{(\Delta_\perp + k^2)^{1/2} + k} + k\,[(n/n_0) - 1]\right]\right\} E(x,y,0). \qquad (I.17)$$

The exponent in equation (I.17) has thus been separated into two terms, the left-hand one containing the derivatives and the right hand term made up of only scalar elements. In this form, the split operator formalism derived in Appendix I-1 can be applied directly. Erasing the solution propagating in the negative z direction, i.e. taking the negative sign in (I.17), and choosing a symmetrized operator form equivalent to equation (I.9) yields immediately

$$E(x,y,\Delta z) = \exp\left\{-i\ \frac{\Delta z}{2}\left[\frac{\Delta_\perp}{(\Delta_\perp + k^2)^{1/2} + k}\right]\right\} \exp\left\{-i\ \Delta z\ k\ [(n/n_0) - 1]\right\}$$

$$\exp\left\{-i\ \frac{\Delta z}{2}\left[\frac{\Delta_\perp}{(\Delta_\perp + k^2)^{1/2} + k}\right]\right\} E(x,y,0) + O(\Delta z^3). \qquad (I.18)$$

As for the beam propagation method based on the Fresnel approximation, the propagation algorithm given above consists of propagating the field at z=0 a distance $\Delta z/2$, then updating the phase of the wave front, and finally completing the sequence by propagating the field a further distance $\Delta z/2$. The operator

$$\exp\left\{-i\ \frac{\Delta z}{2}\left[\frac{\Delta_\perp}{(\Delta_\perp + k^2)^{1/2} + k}\right]\right\}, \qquad (I.19)$$

which governs the propagation of the beam, is thus equivalent to solving the scalar wave equation in a homogeneous medium of refractive index n_0 on a distance $\Delta z/2$ with E(x,y,0) as the initial condition. If the $\Delta_\perp$ term in the denominator of (I.19) is neglected in comparison with k, one recovers the propagation operator obtained from the Fresnel approximation of the scalar Helmholtz equation.

The accuracy of the phase operator can be improved by using the mean index change [3]

$$\delta\bar{n} = \frac{1}{\Delta z}\int_{z_n}^{z_n+\Delta z} k(n/n_0-1)\,dz, \qquad (I.20)$$

over the distance Δz instead of $n=n(\Delta z)$. Numerically, equation (I.20) can be evaluated using a numerical integration technique such as Simpson's rule or a quadrature method. Equations (I.9) and (I.18) are implemented by Fourier transforming the electric field before applying each exponential operator containing derivatives and inverse transforming the resulting expression before applying the phase operator.

Although both BPM formalisms (the Fresnel approximation or the full scalar wave equation) can be applied to most practical fiber problems without changing the physical results, the Fresnel approximation may break down in cases where plane waves with large angular deviations from the z axis are present in the beam. In particular, misleading results can be obtained if the Fresnel approximation is used to study mode coupling in bent or otherwise perturbed waveguides [2]. Since it is no more difficult to generate a numerical solution with equation (I.18) and (I.19) than with the parabolic approximation, the BPM formalism based on the full scalar wave equation is generally preferred for optical fiber applications.

The derivation of the BPM can be adapted, with some effort, for anisotropic media [4]. Since these cases generally involve a nondiagonal dielectric tensor, the Helmholtz equation is used in its matrix form.

The resulting propagation and phase operators, which are applied to a two-component electric field vector, contain matrices in their exponents and are defined by their perturbation series expansions.

I-4. Numerical implementation of the BPM

A numerical representation of the propagation operator in (I.9) can be found by expressing E(x,y,z) as a finite two-dimensional Fourier series [1,2]

$$E(x,y,z) = \sum_{m=-N/2+1}^{N/2} \sum_{n=-N/2+1}^{N/2} \mathbb{E}_{mn}(z) \exp\left(\frac{2\pi}{L} i(mx+ny)\right) \tag{I.21}$$

which is periodic on a square of length $L = N\Delta x = N\Delta y$ of the computational grid in x-y space. This representation will be exact if both E(x,y) and its Fourier spectrum $\mathbb{E}(k_x,k_y)$ vanish outside the interval $(0 \le x,y \le L)$ and $k_{x,y} \le k_{max} = (N/2)(2\pi/L)$, respectively.

Substituting (I.21) into (I.10) yields

$$\begin{aligned} 2ik \sum_{m=-N/2+1}^{N/2} \sum_{n=-N/2+1}^{N/2} \frac{\partial}{\partial z} \mathbb{E}_{mn}(z) \exp\left(\frac{2\pi}{L} i(mx+ny)\right) = \\ = \sum_{m=-N/2+1}^{N/2} \sum_{n=-N/2+1}^{N/2} \Delta_{\perp} \left[\mathbb{E}_{mn}(z) \exp\left(\frac{2\pi}{L} i(mx+ny)\right)\right], \end{aligned} \tag{I.22}$$

and for any valid (m,n)

$$2ik \frac{\partial}{\partial z} \mathbb{E}_{mn}(z) \exp\left(\frac{2\pi}{L} i(mx+ny)\right) = \Delta_{\perp} \left[\mathbb{E}_{mn}(z) \exp\left(\frac{2\pi}{L} i(mx+ny)\right)\right]$$

$$2ik \frac{d\mathbb{E}_{mn}}{\mathbb{E}_{mn}} \exp\left(\frac{2\pi}{L} i(mx+ny)\right) = -(m^2+n^2) \left(\frac{2\pi}{L}\right)^2 dz \exp\left(\frac{2\pi}{L} i(mx+ny)\right).$$

Integrating from 0 to Δz we get an exact expression for $\mathbb{E}_{mn}(\Delta z)$ in Fourier space with $\mathbb{E}_{mn}(0)$ as the initial condition:

$$\mathbb{E}_{mn}(\Delta z) = \mathbb{E}_{mn}(0) \exp\left[\frac{i}{2k} \left(\frac{2\pi}{L}\right)^2 (m^2+n^2)\Delta z \right]$$

$$\mathbb{E}_{mn}(\Delta z) = \mathbb{E}_{mn}(0) \exp\left[\frac{i}{2k} \left(k_x^2 + k_y^2 \right) \Delta z \right], \qquad \text{(I.23)}$$

where k_x and k_y are the traverse wavenumbers

$$k_x = (2\pi m)/L, \qquad k_y = (2\pi n)/L. \qquad \text{(I.24)}$$

It follows from the Sampling Theorem [5] that, if $E(x,y)$ and its spectrum $\mathbb{E}(k_x,k_y)$ remain finite and bounded, the Fourier coefficients $\mathbb{E}_{mn}$ can be evaluated exactly in terms of the sampled values $E(u,v)$, and that there will be a one-to one correspondence between the coefficients $\mathbb{E}_{mn}$ of the Fourier series and the elements $\mathbb{E}^D_{mn}$ of the discrete Fourier transform (see Appendix I-2)

$$\mathbb{E}^D_{mn} = \sum_{u=0}^{N-1} \sum_{v=0}^{N-1} E(u,v) \exp\left[-\frac{2\pi}{N} i(mu+nv) \right], \qquad \text{(I.25)}$$

where $E(u,v) = E(u\Delta x, v\Delta y)$ is evaluated at points $x=u\Delta x$ and $y=v\Delta y$ on the computational grid, with $L=N\Delta x=N\Delta y$.

This implies that a solution of (I.6) and thus the application of the propagation operators in (I.9) is exact if $E(x,y)$ and $\mathbb{E}_{mn}$ remain negligible at the boundaries of their respective computational grids in x-y and Fourier space. For practical purposes, the only error introduced by the BPM algorithm is associated with evaluating the phase term (I.8) numerically on a finite interval, and with the error of order Δz^3 introduced by approximating (I.7) by a symmetrized split operator form.

In the same manner, the numerical implementation of the BPM propagation operator based on the full scalar wave equation is obtained as [2]

$$\mathbb{E}_{mn}(\Delta z) = \mathbb{E}_{mn}(0) \exp \left[i \Delta z \left(\frac{k_x^2 + k_y^2}{\left[-(k_x^2+k_y^2) + k^2\right]^{1/2} + k} \right) \right]. \qquad (I.26)$$

If the $k^2_{x,y}$ terms in the denominator are neglected, equation (I.26) recovers the form of the BPM propagation operator in the Fresnel approximation (equation I.23).

The numerical implementation of the BPM is thus performed by first Fourier transforming the initial field $E(x,y,0)$, then applying the propagation operator over a distance $\Delta z/2$, according to equations (I.23) or (I.26), and inverse Fourier transforming the result. The Fourier transforms can most efficiently be implemented with the Fast Fourier transform algorithm (FFT) [5]. The propagation of the field over the distance $\Delta z/2$ is then followed, in a second step, by multiplication of $E(x,y,\Delta z/2)$ with the phase factor $\exp(-i\ \Delta z\ \delta\bar{n})$, in accordance with equations (I.8) or (I.20), hence

$$E'(x,y,\Delta z/2) = \exp(-i\ \Delta z\ \delta\bar{n})\ E(x,y,\Delta z/2). \qquad (I.27)$$

In the third and final step, the BPM sequence is completed by propagating $E'(x,y,\Delta z/2)$ another distance $\Delta z/2$.

A large number of problems in fiber optics can be solved by direct application of either equation (I.9) or (I.20). Examples are the propagation of light in selectively excited graded index or elliptic fibers [2,6], light propagation through grating structures [7], mode-coupling in bent or otherwise perturbed waveguides [8-10], and the coupling of semiconductor laser light through a microlens-taper system into a single-mode fiber [11]. The BPM has also found application in the analysis of optical fiber solitons in the presence of optical losses and of third-order nonlinearity [12,13], and in the analysis of semiconductor laser behavior [14].

Several authors have considered the applicability of the BPM [15,16]. The most useful discussion was that by L. Thylén [16] in which he derived a number of relations which describe the limitations of the BPM, high-lignting their origin within the formulation of the algorithm. His results can conveniently be incorporated into a BPM computer program to check the applicability of the method and establish a practical value for Δz. Typical waveguide structures without gratings in $LiNbO_3$ support a step size Δz of 10 to 50μm.

I-5. Absorbers

The use of discrete Fourier transforms in the BPM algorithm implies a periodic continuation of the computational window $L=N\Delta y$. If the electric field propagates towards the edge of the computational grid, it will be folded back to the opposite side of the window and superposed onto the propagating field during succeeding steps of the algorithm, causing high-frequency numerical instability of the solution. This can be avoided by absorbing the field at the edge of the grid, either by setting the field to zero at a few points close to the edge of the window, or by inserting a large imaginary component in the refractive index at these points, thus simulating the effect of a lossy cladding [2].

J. Saijonma and D. Yevick [10] discuss the absorber problem in connection with their investigation of loss in bent optical waveguides and fibers. They found that in cases where the electric field at the absorber boundary reaches large values, abrupt absorption of the electric field introduces a large high-frequency diffraction component in the propagating field.

This difficulty can be avoided by using an appropriate function to gradually attenuate the field at the grid boundaries. A suitable absorber function is [10]:

$$\text{absorb}(y) = \begin{cases} 1, & |y| < |y_a| \\ 1/2\,\{1 + \cos^{\gamma}[\pi\,(y-y_b)/y_a-y_b)]\} & |y_a| \le |y| \le |y_b| \\ 0, & |y_b| < |y| < |y_R| \end{cases} \tag{I.28}$$

where y_R is the grid boundary, y_a is the inner edge of the absorber, and y_b is the outer edge ($y=0$ is the center of the computational window). The parameters y_a, y_b, and γ have to be chosen empirically for each application and step size.

In problems where the electric field propagates towards the edge of the computational grid, the accuracy of the solution can be verified by comparing the results for different absorber parameters.

I-6. Power evaluation using BPM data

The Beam Propagation method provides a complete solution of the optical field propagating though an optical fiber. In multi-mode fiber applications, it is often desirable to study mode coupling and frequency dispersion in the fiber. For this purpose, methods for extracting the necessary mode data (propagation constants, mode eigenfunctions, etc.) from the BPM field have to be developed. Such calculations are usually performed by exciting the waveguide with one of its modal eigenfunctions and then projecting the optical field obtained after each BPM step onto a set of numerically generated normal or local modal eigenfunctions [2,17-19].

For our purposes, a method of evaluating the power in a particular mode propagating through an integrated optical device is required. This can be achieved by over-lapping the output field Ψ_{out} obtained from the BPM with the normalized guided mode ϕ_{in} of the waveguide [10] (obtained either analytically or, should analytical solutions for the modes not exist for the particular index distribution used, from the BPM calculation of the field in a straight waveguide of appropriate dimensions and index distribution, e.g. the effective index, see section II.2). Accordingly,

$$P_{out} = \left| \int \Psi_{out} \, \phi^{*}_{in} \, dy \right|^2 \qquad (I.29)$$

where ϕ^{*}_{in} is the complex conjugate of ϕ_{in}. For multi-mode devices it is necessary to calculate the power propagating in each mode separately by overlapping the output modal field obtained from the BPM with a normalized guided mode of appropriate order m.

I-7. Summary

The *Beam Propagation Method*, as introduced by M.D. Feit and J.A. Fleck and based on the full scalar wave equation, is given in split operator notation as

$$E(x,y,\Delta z) = \exp\left\{-i \frac{\Delta z}{2} \left[\frac{\Delta_\perp}{(\Delta_\perp + k^2)^{1/2} + k} \right] \right\} \exp\left\{-i \, \delta\bar{n} \, \Delta z \right\}$$

$$\exp\left\{-i \frac{\Delta z}{2} \left[\frac{\Delta_\perp}{(\Delta_\perp + k^2)^{1/2} + k} \right] \right\} E(x,y,0). \qquad (I.30)$$

For fields which vary slowly along the propagation direction in distances of the order of a wavelength, it is sufficient to approximate the scalar Helmholtz equation by the Fresnel equation. For this case, the BPM algorithm takes the form

$$E(x,y,\Delta z) = \exp\left[-\frac{i}{4k}\Delta z\ \Delta_\perp\right]\exp\left[-\frac{i}{2k}\Delta z\ \delta\bar{n}\right]\exp\left[-\frac{i}{4k}\Delta z\ \Delta_\perp\right]E(x,y,0). \tag{I.31}$$

The numerical implementation of the BPM is governed by equations (I.23) though (I.26), and involves the extensive use of Fourier transforms. The latter can most efficiently be performed using the Fast Fourier Transform (FFT), which significantly reduces the amount of calculations required for one propagation step.

The main advantage of the BPM is undoubtedly its ability to describe both the guided and the radiating parts of the optical field in a uniform formalism. It is limited, however, to problems where the refractive index distribution has only small variations from a reference value n_0. The effect of the reflected field on the forward propagating direction is also neglected.

Appendix I-1: Proof of second-order accuracy of the split-operator solution of the propagation equation [1]

The propagation equation (I.6)

$$\frac{\partial E}{\partial z} = - \frac{i}{2k} \left[\Delta_\perp + k^2(n^2/n_0^2-1) \right] E, \qquad \text{(AI.1)}$$

was solved in section I-2 by formal integration to give

$$E(z_n+\Delta z) = \exp\left\{- \frac{i}{2k} \left[\Delta z \, \Delta_\perp + \int_{z_n}^{z_n+\Delta z} k(n^2/n_0^2-1)\right]\right\} E(z_n) \qquad \text{(AI.1a)}$$

and was then, to second order accuracy, replaced by a symmetric split operator form

$$E(z_n+\Delta z) = \exp\left[- \frac{i}{4k} \Delta z \, \Delta_\perp \right] \exp\left[- \frac{i}{2k} \Delta z \, \delta\bar{n} \right] \exp\left[- \frac{i}{4k} \Delta z \, \Delta_\perp \right] E(z_n). \qquad \text{(AI.1b)}$$

To prove this, consider, for simplicity, the equation

$$\frac{\partial E}{\partial z} = (\Delta_\perp + \mathcal{X}) \, E = a(z) \, E \qquad \text{(AI.2)}$$

where $\Delta_\perp$ is the transverse Laplacian and $\mathcal{X}(z)$ is an appropriate operator. The operators $\Delta_\perp$ and $\mathcal{X}(z)$ do not necessarily commute. The solution of (AI.1) is obtained formally by integration as

$$E(z) = \exp\left[\int_0^z a(z') \, dz'\right] E(0). \qquad \text{(AI.3)}$$

The exponent in (AI.3) can be expanded in terms of a Taylor series as

$$\exp\left[\int_0^z a(z')\ dz'\right] = 1 + \int_0^z a(z')\ dz' + \frac{1}{2}\left[\int_0^z a(z')\ dz'\right]^2 + \frac{1}{3!}\left[\int_0^z a(z')\ dz'\right]^3 + \ldots$$

Since

$$\int_0^z a(z')\ dz'\left[\int_0^{z'} a(z'')\ dz''\right]^m = \int d\left[\int_0^{z'} a(z'')\ dz''\right]\left[\int_0^{z'} a(z'')\ dz''\right]^m = \frac{1}{m+1}\left[\int_0^z a(z')\ dz'\right]^{m+1},$$

the terms in the above Taylor series can be replaced as

$$\exp\left[\int_0^z a(z')\ dz'\right] = 1 + \int_0^z a(z')\ dz' + \int_0^z a(z')\ dz' \int_0^{z'} a(z'')\ dz'' + \frac{1}{2}\int_0^z a(z')\ dz'\left[\int_0^{z'} a(z'')\ dz''\right]^2 + \ldots$$

and finally

$$\exp\left[\int_0^z a(z')\ dz'\right] = 1 + \int_0^z a(z')\ dz' + \int_0^z a(z')\ dz' \int_0^{z'} a(z'')\ dz'' + \int_0^z a(z')\ dz' \int_0^{z'} a(z'')\ dz'' \int_0^{z''} a(z''')\ dz''' + O(z^4). \quad \text{(AI.4)}$$

Substituting for a(z) gives

$$\exp\left[\int_0^z a(z')\ dz'\right] = 1 + \Delta_\perp z + \int_0^z \mathfrak{X}(z')\ dz' + \Delta_\perp^2 \frac{z^2}{2} + \Delta_\perp \int_0^z dz' \int_0^{z'} \mathfrak{X}(z'')\ dz'' + \int_0^z \mathfrak{X}(z')\ z'\ \Delta_\perp\ dz' + \int_0^z \mathfrak{X}(z')\ dz' \int_0^{z'} \mathfrak{X}(z'')\ dz'' + O(z^3).$$

(AI.5)

Similarly, the split operator form equivalent to (I.9) can be expanded in terms of a perturbation series. The individual factors are, to second order,

$$\exp\left[\frac{1}{2} \Delta_\perp z \right] = 1 + \frac{1}{2} \Delta_\perp z + \frac{1}{8} \Delta_\perp^2 z^2 \text{ , and}$$

$$\exp\left[\int_0^z \mathcal{X}(z')\, dz' \right] = 1 + \int_0^z \mathcal{X}(z')\, dz' + \int_0^z \mathcal{X}(z')\, dz' \int_0^{z'} \mathcal{X}(z'')\, dz'',$$

so that the split operator expression of (AI.3) expands to

$$\exp\left[\frac{1}{2} \Delta_\perp z \right] \exp\left[\int_0^z \mathcal{X}(z')\, dz' \right] \exp\left[\frac{1}{2} \Delta_\perp z \right] =$$

$$\left[1 + \frac{1}{2} \Delta_\perp z + \frac{1}{8} \Delta_\perp^2 z^2\right]\left[1 + \int_0^z \mathcal{X}(z')\, dz' + \int_0^z \mathcal{X}(z')\, dz' \int_0^{z'} \mathcal{X}(z'')\, dz''\right]$$
$$\left[1 + \frac{1}{2} \Delta_\perp z + \frac{1}{8} \Delta_\perp^2 z^2\right]$$

$$= 1 + \Delta_\perp z + \frac{1}{2} \Delta_\perp^2 z^2 + \int_0^z \mathcal{X}(z')\, dz' + \int_0^z \mathcal{X}(z')\, dz' \int_0^{z'} \mathcal{X}(z'')\, dz''$$
$$+ \frac{z}{2} \int_0^z \mathcal{X}(z')\, dz' \Delta_\perp + \frac{1}{2} \Delta_\perp z \int_0^z \mathcal{X}(z')\, dz' + O(z^3). \qquad \text{(AI.6)}$$

Subtracting (AI.6) from (AI.5) yields

$$\exp\left[\int_0^z a(z')\, dz' \right] - \exp\left[\frac{1}{2} \Delta_\perp z \right] \exp\left[\int_0^z \mathcal{X}(z')\, dz' \right] \exp\left[\frac{1}{2} \Delta_\perp z \right] =$$

$$- \Delta_\perp \int_0^z dz' \left[\frac{z}{2} \mathcal{X}(z') - \int_0^{z'} dz'' \mathcal{X}(z'') \right] - \int_0^z dz' \mathcal{X}(z') \left[\frac{z}{2} - z' \right] \Delta_\perp + O(z^3)$$
$$\text{(AI.7)}$$

If the split operator expression (AI.6) is to be a representation of (AI.3) to second order, the integral terms on the right-hand side of (AI.7) must either vanish or be of order z^3. Clearly, these terms vanish if $\mathcal{X}(z)$ is a constant. If $\mathcal{X}(z)$ can be represented as a Taylor series in z

$$\mathcal{X}(z) = \mathcal{X}(0) + \mathcal{X}'(0)\, z + \frac{1}{2}\, \mathcal{X}''(0)\, z^2 + \ldots ,$$

the integral terms are of order z^3 which can be verified easily by substitution of the Taylor series in (AI.7) and taking the integrals.

Thus, the solution of the propagation equation (I.6) can be written to second order accuracy in a symmetrically split operator form as

$$\exp\left[\int_0^z \left[\Delta_\perp + k^2(n^2/n_0^2 - 1)\right] dz'\right] =$$

$$\exp\left[\frac{1}{2}\,\Delta_\perp z\right] \exp\left[\int_0^z k^2(n^2/n_0^2 - 1)\; dz'\right] \exp\left[\frac{1}{2}\,\Delta_\perp z\right].$$

Appendix I-2: The Discrete Fourier Transform

The field E(x,y,z) can be expressed as a finite two-dimensional Fourier series [1,2]

$$E(x,y,z) = \sum_{m=-N/2+1}^{N/2} \sum_{n=-N/2+1}^{N/2} \mathbb{E}_{mn}(z) \exp\left(\frac{2\pi}{L}\, i(mx+ny)\right) \qquad \text{(AI-2.1)}$$

which is periodic on a square of length $L = N\Delta x = N\Delta y$ of the computational grid in x–y space, i.e. implying a periodic extension of the field outside the region of concern. This representation will be exact if both E(x,y) and its Fourier spectrum $\mathbb{E}(k_x,k_y)$ are strictly bandwidth limited, i.e. they vanish outside the interval $(0\le x,y\le L)$, and $k_{x,y} \ge k_{max} = (N/2)(2\pi/L)$, respectively.

The *Sampling Theorem* [5] permits the field E to be represented in terms of sampled values $E(u,v) = E(u\Delta x, v\Delta y)$ at equally spaced points on the computational grid. The sampled field values are then given as

$$E(u,v,z) = \sum_{m=-N/2+1}^{N/2} \sum_{n=-N/2+1}^{N/2} \mathbb{E}_{mn}(z) \exp\left(\frac{2\pi}{N}\, i(mu+nv)\right) \qquad \text{(AI-2.2)}$$

Consider for clarity only one transverse direction. Defining new coefficients $E^D(u)$ and E^D_m in terms of E(u,v) and $\mathbb{E}_m$ as

$$\begin{aligned} E^D(u+N/2) &= E\,(u\Delta x), && u=-N/2 \ldots N/2-1 \\ E^D_m &= (-1)^m\, \mathbb{E}_m, && m=0 \ldots N/2-1 \qquad \text{(AI-2.3)} \\ E^D_{m+N} &= (-1)^m\, \mathbb{E}_m, && m=-N/2 \ldots -1, \end{aligned}$$

then

$$E(u) = \sum_{m=-N/2+1}^{N/2} \mathbb{E}_m(z) \exp\left(\frac{2\pi}{N}\, i(mu)\right) \qquad \text{(AI-2.4)}$$

translates to the inverse discrete Fourier transform

$$E^D(u) = \sum_{m=0}^{N-1} \mathbb{E}_m^D \exp\left[\frac{2\pi}{N} i(mu)\right], \qquad \text{(AI-2.5)}$$

with

$$\mathbb{E}_m^D = \frac{1}{N} \sum_{u=0}^{N-1} E(u) \exp\left[-\frac{2\pi}{N} i(mu)\right] \qquad \text{(AI-2.6)}$$

being the discrete Fourier transform. From the Sampling theorem it follows also that there will be a one-to one correspondence between the coefficients $\mathbb{E}_m$ of the Fourier series and the elements $\mathbb{E}_m^D$ of the discrete Fourier transform.

The generalization to two dimensions becomes

$$\mathbb{E}_{mn}^D = \frac{1}{N^2} \sum_{u=0}^{N-1} \sum_{v=0}^{N-1} E^D(u,v) \exp\left[-\frac{2\pi}{N} i(mu+nv)\right], \qquad \text{(AI-2.7)}$$

where $E^D(u,v) = E^D(u\,\Delta x, v\,\Delta y)$ is evaluated at points $x=u\Delta x$ and $y=v\Delta y$ on the computational grid.

References:

1 Fleck, J.A., Morris, J.R., and Feit, M.D., 'Time-dependent propagation of high energy laser beams through the atmosphere,' *Appl.Phys.*, 10, pp.129-160, 1976.

2 Feit, M.D., and Fleck, J.A., 'Light propagation in graded-index fibers,' *Appl. Optics*, 17, 24, pp. 3990-3998, 1978.

3 Danielsen, P. and Yevick, D., 'Improved analysis of the propagating beam method in longitudinally perturbed optical waveguides,' *Appl. Opt.*, 21, 23, pp. 4188-4182, 1982.

4 Thylén, L. and Yevick, D., 'Beam propagation method in anisotropic media,' *Appl. Opt.*, 21, 15, pp. 27512754, 1982.

5 Brigham, E.O., *The Fast Fourier Transform*, Prentice-Hall, Englewood Cliffs, New Jersey, 1974.

6 Saijonmaa, J., Halme, S., and Yevick, D., 'Beam propagation in elliptical fibers,' *Optical and. Quantum Electr.*, 14, pp. 225-236, 1982.

7 Yevick, D. and Thylén, L., 'Analysis of gratings by the beam-propagation method,' *J. Opt. Soc. Amer.*, 72, pp.1084-1089, 1982.

8 Danielsen, P. and Yevick, D., 'Propagating beam analysis of bent optical waveguides,' *J. Opt. Comm.*, 4, pp. 494-498, 1983.

9 Saijonmaa, J., Yevick, D., and Hermansson, B., 'An analysis of single-mode fiber bending loss,' *Proc. of IOOC*, Tokyo, 27-30 June, 1983.

10 Saijonma, J., and Yevick, D., 'Beam propagation analysis of loss in bent optical waveguides and fibers,' *Opt. Soc. Am.*, 73, 12, pp.1785-1791, 1983.

11 Hermansson, B., Yevick, D., and Saijonmaam J., 'A propagating beam method analysis of the coupling of semiconductor laser light into tapers,' *Proc. of ECOC*, Oct. 23-26, Geneva, 1983.

12 Yevick, D. and Hermansson, B., 'Soliton analysis with the propagating beam method,' *Opt. Comm.*, 47, pp.101-106, 1983.

13 Hermansson, B., Thylén, L., and Yevick, D., 'A propagating beam method analysis of nonlinear effects in optical waveguides,' *Opt. and Quantum. Electr.*, 16, 6, pp. 524-534, 1985.

14 Meissner, P., Patzak, E., and Yevick, D., 'A self-consistent model of stripe geometry lasers based on the beam propagation method,' *J. Quant. Electr.*, QE-20, 8, pp. 899-905, 1984.

15 Van Roey, J., van der Donk, J., and Lagasse, P.E.: 'Beam-propagation method: analysis and assessment,' *J. Opt. Soc. Am.*, 71, pp.803-810, 1981.

16 Thylén, L., 'The beam propagation method: an analysis of its applicability,' *Opt.Quant. Elec.*, 15, pp.433-439, 1983.

17 Feit, M.D., and Fleck, J.A., 'Calculation of dispersion in graded-index multimode fibers by a propagating-beam method,' *Appl. Optics*, 18, 16, pp.2843-2851,1979.

18 Feit, M.D., and Fleck, J.A., 'Mode properties and dispersion for two optical fiber-index profiles by the propagating beam method,' *Appl. Optics*, 19, 18, pp.2240-2246, 1980.

19 Yevick, D. and Danielsen, P., 'Numerical investigation of mode coupling in sinusoidally modulated parabolic graded index planar waveguides,' *Appl. Optics*, 21, 15, pp. 2727-2733, 1982.

CHAPTER II. APPLICATION OF THE BPM TO INTEGRATED OPTICAL DEVICES

II-1. Introduction

The Beam Propagation Method described in the previous section is only valid for small changes in refractive index from a reference value n_0. It is obvious that the large index change between the integrated optical device and air cannot be treated in this fashion.

One possibility of overcoming this problem consists of taking n_0 as a periodic extension (Figure II-1) of the refractive index step between the guide and air [1]. The theoretical derivation of the BPM given in chapter I remains valid except that the solutions of equation (I.1) are no longer plane waves but the eigenmodes of a step index slab waveguide. In this manner, a correct description of the fields in both air and in the guide can be obtained so that, for example, the radiation loss from the guide into air can be calculated. TE or TM like fields can be treated by choosing either the TE or TM modes of the periodic slab waveguides. TE-TM mode conversion can obviously not be calculated. This approach, however, means that in one transverse direction one has to use matrix multiplication for the decomposition of the field into slab eigenmodes instead of the Fast Fourier Transform (FFT). The practical applicability of the BPM rests, however, on the use of Fast Fourier Transforms. It is their computational speed and numerical stability that make the large number of propagation steps required by the BPM feasible.

A more powerful way of overcoming the guide/air interface problem is achieved by combining the *Effective Refractive Index Method* [2] with the BPM approach. In such a formulation, the integrated optical guide is replaced with a series of slab waveguides where their effective refractive index corresponds to the index variation in the depth (x-) direction. This reduces the three dimensional guide shown in Figure II-2 to a corresponding two dimensional structure which no longer contains large refractive index steps. Provided this structure satisfies the usual restrictions of the BPM, it can be solved using a two dimensional (y,z) BPM algorithm. It should be pointed out that this reduction to two dimensions greatly reduces the necessary amount of computer memory and processor time, since the BPM now only requires a one-dimensional FFT. TE or TM modes are chosen while calculating the effective index distribution $n_{eff}(y,z)$.

The use of the Effective Index Method only allows the analysis of mono-mode guides in the depth direction. This condition can be satisfied in most integrated optic circuits. Also, radiation from the guide into air or into the substrate can not be described. However, in many cases one can neglect the radiation into the air or into the substrate due to the planar character of integrated optical devices. This means that an accurate three dimensional modelling of, for example, radiation loss is not possible.

This method does, however, give insights into the propagation of light through integrated optic structures and is well suited for the design oriented analysis of both active and passive integrated optical devices [3].

II-2. Effective index modelling of diffused waveguides

An approximate solution for the three dimensional scalar wave equation

$$\frac{\partial^2 \mathcal{E}}{\partial x^2} + \frac{\partial^2 \mathcal{E}}{\partial y^2} + \frac{\partial^2 \mathcal{E}}{\partial z^2} + \frac{\omega^2}{c^2} n^2 \mathcal{E} = 0 \tag{II.1}$$

can be found by imposing a product solution

$$\mathcal{E}(x,y,z) = E(y,z)\ \Psi(x), \tag{II.2}$$

and separating variables leads immediately to

$$\frac{\partial^2 E}{\partial x^2} + \frac{\partial^2 E}{\partial y^2} + \frac{\omega^2}{c^2} n_{eff}^2\ E = 0 \tag{II.3}$$

and

$$\frac{d^2\Psi}{dx^2} + k_0[n^2(x,y,z) - n_{eff}(y,z)]\ \Psi = 0. \tag{II.4}$$

In the above equations, $n_{eff}(y,z)$ has the meaning of an effective index distribution in the y-z plane for a particular (usually the fundamental) mode of a planar waveguide with an index distribution n(x,y,z) at every surface point (y,z). The refractive index profile n(x,y,z) is taken from diffusion theory. n_{eff} could be calculated directly from equation (II.4) using some numerical procedure such as a shooting method. The effective index theory developed for diffused waveguides by Burns and Hocker [4] is, however, a more effective way of calculating n_{eff} for our BPM applications.

For titanium diffused channel waveguides the refractive index profile, neglecting sideways diffusion, can be written as [4]

$$n(x) = n_b + \Delta n_s\ f(x) \tag{II.5}$$

where n_b is the substrate index, Δn_s the Ti induced surface index change, and $f(x)$ an appropriate function describing the diffusion profile variation with respect to the depth coordinate. $f(x)$ is usually chosen to be an error-function, an exponential or Gaussian distribution depending on the actual diffusion conditions used in the fabrication process.

As shown in Hocker *et al.*, the effective index n_{eff} of a homogeneous slab waveguide equivalent to the diffused guide can be found by solving the dispersion relation

$$2k_0\int_0^{x_t} (n(x)^2 - n_{eff}^2)^{1/2}dx = (2m+\frac{3}{2})\ \pi, \qquad m=0,1,... \tag{II.6}$$

where m=0 for a single mode waveguide, and x_t is the so-called turning point defined by

$$n(x_t) = n_{eff} \ . \tag{II.7}$$

It is not desirable to introduce normalized parameters in the dispersion relation since, for applications to active integrated devices, the diffusion profile $n(x)$ will be perturbed by the index change δn induced electro-optically (see section II-3).

II-2.1 Effective index modelling of ridge waveguides

A ridge waveguide can be fabricated by ion beam milling a ridge structure out of a previously Ti indiffused slab waveguide. In an effective index model, this ridge waveguide is replaced by three homogeneous slab waveguides of effective indices n_{eff}^{ridge} and n_{eff}^{mil} , as shown in Figure II-3. The dispersion relation given as equation (II.6) can be used to calculate the effective index n_{eff}^{ridge} of the ridge guide. For the milled region, n_{eff}^{mil} can be calculated by modifying the lower integration limit in the dispersion equation to reflect the milling depth x_{mil}, thus

$$2k_0 \int_{x_{mil}}^{x_t} (n(x)^2 - n_{eff}^2)^{1/2}\, dx = (2m+\frac{3}{2})\, \pi, \qquad m=0,1,... \qquad (II.8)$$

with $n(x_t) = n_{eff}$ as before.

II-3. Electro-optic index change

Electro-magnetic wave propagation in a crystal is characterized by the so-called indicatrix or index ellipsoid. The orientation of this ellipsoid model is related to the crystal axes (equal to the principal axis of the ellipsoid) and the half-lengths of the principal axes are, in turn, related to the principal indices of refraction. The indicatrix is used mainly to determine the refractive indices associated with the two normal modes, polarized along the prinipal axis of the ellipsoid, of a plane wave propagating along an arbitrary direction. The ellipsoid is expressed as [5]

$$\frac{x^2}{n_x^2} + \frac{y^2}{n_y^2} + \frac{z^2}{n_z^2} = 1, \qquad (II.9)$$

where n_x, n_y, and n_z are the refractive indices in the x-, y-, znd z-directions.

Active integrated optical devices operate by taking advantage of the electro-optic index change δn induced in certain optical materials by an electric field applied across the crystal. The electric field induces a change in the optical dielectric properties of the crystal which in turn leads to a deformation of the indicatrix or index ellipsoid. The electro-optic change in refractive index δn induced by an applied electric field E is given as [5]

$$\Delta\left(\frac{1}{n^2}\right) = r\ E + R^2\ E^2. \qquad \text{(II.10)}$$

The first term is linearly dependent on the applied electric field E and is known as the *Pockels effect*, whereas the second, quadratically dependent term, is the *Kerr electro-optic effect*. The former is also dependent on the polarization of the applied electric field. The electro-optic index change alters the shape, size and orientation of the ellipsoid. The general expression for the deformed indicatrix is given as

$$a_{11}x^2 + a_{22}y^2 + a_{33}z^2 + 2a_{23}yz + 2a_{31}zx + 2a_{12}xy = 1. \qquad \text{(II.11)}$$

The coefficients a_{ij} are determined by

$$\begin{bmatrix} a_{11}-1/n_x^2 \\ a_{22}-1/n_y^2 \\ a_{33}-1/n_z^2 \\ a_{23} \\ a_{31} \end{bmatrix} = \begin{bmatrix} r_{11} & r_{12} & r_{13} \\ r_{21} & r_{22} & r_{23} \\ r_{31} & r_{32} & r_{33} \\ r_{41} & r_{42} & r_{43} \\ r_{51} & r_{52} & r_{53} \end{bmatrix} \begin{bmatrix} E_x \\ E_y \\ E_z \end{bmatrix}, \qquad \text{(II.12)}$$

where r_{ij} are called the electro-optic or Pockels constants, E_x, E_y, and E_z are the components of the applied electric field, and n_x , n_y , n_z the refractive indices in the appropriate directions. If the applied field is zero, equation (II.11) reduces to (II.9).

Some of the most popular electro-optic crystals used for active integrated optic devices are: lithium niobate ($LiNbO_3$), lithium tantalate ($LiTaO_3$), potassium dihydrogen phosphate or KDP (KH_2PO_4), ammonium dihydrogen phosphate or ADP, and gallium arsenide (GaAs) [5].

In particular, integrated electro-optic devices in $LiNbO_3$ with titanium indiffused channel waveguides have in recent years [6] reached a high status of development.

The electro-optic tensor for $LiNbO_3$ is [5]

$$\begin{bmatrix} 0 & -r_{22} & r_{13} \\ 0 & r_{22} & 0 \\ 0 & 0 & r_{33} \\ 0 & r_{51} & 0 \\ r_{51} & 0 & 0 \\ -r_{22} & 0 & 0 \end{bmatrix} \quad ; \quad \begin{array}{l} r_{13} = 8.6 \\ r_{33} = 30.8 \\ r_{22} = 3.4 \\ r_{51} = 28 \end{array} \quad [10^{-12}\ m/V].$$

With $n_x = n_y = n_o$, $n_z = n_e$, and $E_x = E_y = 0$, equations (II.11) and (II.12) lead to

$$(n_o^{-2} + r_{13}E_z)\ x^2 + (n_o^{-2} + r_{13}E_z)\ y^2 + (n_e^{-2} + r_{33}E_z)\ z^2 = 1. \qquad \text{(II.13)}$$

If we compare equation (II.13) with (II.9), we see that the effect of $(r_{13}E_z)$ is to change the index of refraction n_o for a wave polarized along the x-axis, so that the new index is given by $n_o + \Delta n_x$. Since, in practice, the products $(r_{13}\ E_z)$ and $(r_{33}\ E_z)$ is much smaller than n_o or n_e, the approximation $\Delta(1/n^2) \cong -2\ \Delta n/n^3$ [7] can be used to express (II.13). Taking

$$\frac{1}{(n_o + \Delta n_x)^2} = n_o^{-2} + \Delta\left[\frac{1}{n_o^2}\right] \cong n_o^{-2} + \left[\frac{-2\ \Delta n_x}{n_o^3}\right] = (n_o^{-2} + r_{13}E_z) \qquad \text{(II.14)}$$

and solving for Δn_x yields for the indicatrix

$$\frac{x^2}{\left[n_o - \frac{n_o^3}{2} r_{13}E_z\right]^2} + \frac{y^2}{\left[n_o - \frac{n_o^3}{2} r_{13}E_z\right]^2} + \frac{z^2}{\left[n_e - \frac{n_e^3}{2} r_{33}E_z\right]^2} = 1. \qquad \text{(II.15)}$$

The corresponding refractive index changes induced by applying E_z are:

$$n_x = n_o - 1/2\, r_{13}\, n_o^3\, E_z$$
$$n_z = n_e - 1/2\, r_{33}\, n_e^3\, E_z. \tag{II.16}$$

The polarization of the optical field is usually chosen parallel to the c-axis of the crystal to maximize the electro-optic constant and thus the induced index change.

The electric field distribution E in the substrate can be obtained analytically by conformal mapping for electrodes placed directly on the $LiNbO_3$ surface [8]. Metallic electrodes, however, attenuate the optical waves, and in practice, the electrodes have to be separated from the crystal surface by a thin, low-index buffer layer. The buffer layer, on the other hand, attenuates the electric field strength because of its lower index compared to that of $LiNbO_3$. A conformal mapping solution of the applied field distribution is then not possible anymore and a numerical approach has to be used.

A semi-analytical treatment of the potential problem in the presence of a buffer layer is, however, possible [9] and will be adopted for our purposes.

Consider the electrode configuration shown in Figure II-4. The electrodes are separated from the crystal surface by a buffer layer of SiO_2 of thickness d_0. In both regions (SiO_2 and $LiNbO_3$), the potential φ is given by

$$\varepsilon_x \frac{\partial^2 \varphi}{\partial x^2} + \varepsilon_y \frac{\partial^2 \varphi}{\partial y^2} = 0, \tag{II.17}$$

where $\varepsilon_x = \varepsilon_y = 4$ (SiO_2) in the buffer layer, and 28 and 43 [10], respectively, in the $LiNbO_3$.

The boundary conditions are:

$$\begin{cases} \varphi\ (x\ \infty,\ y) = 0, \\ \text{at the electrodes, } \varphi(0,y) = U, \text{ the applied voltage,} \\ \text{between the electrodes, the normal derivative } \dfrac{\partial\varphi}{\partial n} \text{ is zero.} \end{cases} \tag{II.18}$$

The interface conditions at $x=d_0$ are the continuity of the potential

$$\varphi_1(d_0,y) = \varphi_0(d_0,y), \tag{II.19}$$

and of the displacement vector in the x direction

$$\varepsilon_x \frac{\partial\varphi_1}{\partial x}(d_0,y) = \varepsilon_1 \frac{\partial\varphi_0}{\partial x}(d_0,y). \tag{II.20}$$

The change in the dielectric constant induced by the titanium diffusion into the $LiNbO_3$ crystal is considered negligible. Equation (II.9) has analytical solutions in the buffer and crystal regions, and the application of the boundary conditions yields relations describing the potential throughout both regions in terms of the potential at the buffer-$LiNbO_3$ interface and at the electrode surface, respectively, and a relation linking the potential at the electrode surface to that at the buffer-$LiNbO_3$ interface.

The problem of calculating the potential in the crystal can thus be solved in two steps. First, the variation of the potential at the buffer-$LiNbO_3$ interface is calculated in terms of the potential at the electrode surface, and then the potential function at the electrode surface is determined separately. The potential throughout the crystal is then given immediately from the analytical solutions of Laplace's equation in terms of the potential at the buffer-$LiNbO_3$ interface.

It can be shown by direct substitution into equation (II.17) that the potential in the $LiNbO_3$ region ($x>d_0$) is given by [9]

$$\varphi_1(x,y) = \int d\nu\ \phi_1(d_0,\nu)\ e^{i2\pi\nu y}\ e^{-2\pi|\nu|(x-d_0)\sqrt{\varepsilon y/\varepsilon x}}, \qquad (II.21)$$

where ϕ is the Fourier transform of φ with respect to the y direction. (It is easily verified that the above expression satisfies Laplace's equation and the boundary conditions at $x=d_0$ and $x\ \infty$). Thus, if the transformed potential $\phi_1(d_0,\nu)$ at the buffer/$LiNbO_3$ interface is known, the potential throughout the $LiNbO_3$ crystal is determined analytically by equation (II.21).

Next, a relationship between the potential at the buffer/$LiNbO_3$ interface and the electrode surface can be found by applying a Fourier transform with respect to the y direction to equation (II-17) in the buffer region, which yields

$$\frac{\partial^2\phi_0}{\partial x^2} - (2\pi\nu)^2\phi_0 = 0 \qquad (II.22)$$

with $\phi_0(x,\nu)$ the Fourier transformed potential of $\varphi_0(x,y)$:

$$\varphi_0(x,y) = \int d\nu\ \phi_0(x,\nu)\ e^{i2\pi\nu y}, \qquad (II.23)$$

and ν the spacial frequency in the y direction. The interface conditions in Fourier space become:

$$\begin{aligned} \phi_1(d_0,\nu) &= \phi_0(d_0,\nu) \\ \varepsilon_x \frac{\partial\phi_1}{\partial x}(d_0,\nu) &= \varepsilon_i \frac{\partial\phi_0}{\partial x}(d_0,\nu). \end{aligned} \qquad (II.24)$$

The analytical solution of equation (II.22) in the buffer region is

$$\phi_0(x,\nu) = G_1(\nu)\ \exp(-2\pi|\nu|x) + G_2(\nu)\ \exp(+2\pi|\nu|x), \qquad (II.25)$$

and the interface conditions become

$$\phi_1(d_0,\nu) = \phi_0(d_0,\nu) = G_1(\nu)\ \exp(-2\pi|\nu|d_0) + G_2(\nu)\ \exp(+2\pi|\nu|d_0) \qquad (II.26)$$

and

$$\varepsilon_x \frac{\partial \phi_1}{\partial x} (d_0, \nu) = \varepsilon_1 \Big\{ G_1(\nu) \; [-2\pi|\nu|] \; \exp(-2\pi|\nu| \; d_0) + \qquad \text{(II.27)}$$

$$G_2(\nu) \; [+2\pi|\nu|] \; \exp(+2\pi|\nu| \; d_0) \Big\}.$$

Calculating the derivative from (II.21) and solving for G_1 and G_2 in equations (II.26) and (II.27) yields immediately:

$$G_1(\nu) = \frac{1}{2} \exp(+2\pi|\nu|d_0) \; \phi_1(\nu, d_0) \left\{1 + \sqrt{\varepsilon x \varepsilon y} \,/\, \varepsilon_1\right\} \qquad \text{(II.28)}$$

$$G_2(\nu) = \frac{1}{2} \exp(-2\pi|\nu|d_0) \; \phi_1(\nu, d_0) \left\{1 - \sqrt{\varepsilon x \varepsilon y} \,/\, \varepsilon_1\right\}, \qquad \text{(II.29)}$$

and thus (II.26) becomes

$$\phi_0(0, \nu) = \phi_1(d_0, \nu) \left\{\cosh(2\pi|\nu|d_0) + \sinh(2\pi|\nu|d_0) \sqrt{\varepsilon x \varepsilon y} \,/\, \varepsilon_1\right\}. \qquad \text{(II.30)}$$

(II.30) is the desired relation between the Fourier transform of the potential φ_0 at the electrode surface and $\varphi_1 = \varphi_0$ at the buffer/$LiNbO_3$ interface. Thus if the potential at the electrode surface is known, (II.30) can be used to calculate the corresponding potential at the buffer layer/ $LiNbO_3$ interface, and thus the potential throughout the crystal can be calculated immediately from equation (II.21).

It still remains to determine the potential $\varphi_0(0, y)$ in the presence of the buffer layer. A solution of the potential in region -1 can be written similarly to equation (II-21) as

$$\varphi_{-1}(x, y) = \int d\nu \; \phi_0(0, \nu) \; e^{i2\pi\nu y} \; e^{2\pi|\nu|x}. \qquad \text{(II.31)}$$

The interface condition in Fourier space between regions -1 and 0 is the continuity of D_x at x=0, thus

$$\varepsilon_{00} \frac{\partial \phi_{-1}}{\partial x} = \varepsilon_1 \frac{\partial \phi_0}{\partial x}. \qquad \text{(II.32)}$$

Calculating the derivatives $\partial/\partial x$ gives:

$$\varepsilon_{00}\phi_0(0,\nu)\ (2\pi|\nu|) = \varepsilon_1 \Big\{G_1(\nu)(-2\pi|\nu|)\ \exp(-2\pi|\nu|\ 0) +$$
$$G_2(\nu)(+2\pi|\nu|)\ \exp(+2\pi|\nu|\ 0)\Big\}$$

$$\varepsilon_{00}\phi_0(0,\nu)|\nu| = \varepsilon_1 \Big\{G_1(\nu)(-|\nu|) + G_2(\nu)(+|\nu|)\Big\},$$

substituting for G_1 and G_2 yields

$$\varepsilon_{00}\phi_0(0,\nu)|\nu| = -\varepsilon_1|\nu|\ \phi_1(d_0,\nu)\Big\{\sinh(2\pi|\nu|d_0) + \alpha\cosh(2\pi|\nu|d_0)\Big\}, \tag{II.33}$$

with $\alpha = \sqrt{\varepsilon x \varepsilon y}/\varepsilon_1$. Next, using equation (II-30) to replace $\phi_1(d_0,\upsilon)$ in (II.33) and inverse Fourier transforming gives the relation

$$\int d\nu\ |\nu|\ \phi_0(0,\nu)\ e^{i2\pi\nu y} \quad \cdot \tag{II.34}$$

$$\cdot\ \left[\varepsilon_1 \frac{\sinh(2\pi|v|d_0) + \alpha\cosh(2\pi|v|d_0)}{\cosh(2\pi|v|d_0) + \alpha\sinh(2\pi|v|d_0)} + \varepsilon_{00}\right] = 0.$$

It can be recognized from a similar treatment of the electrode problem in the absence of a buffer layer (see Appendix II-1) that as d_0 goes to zero, $\phi_0(0,\nu)$ will approach the potential $\phi_0^B(0,\nu)$, the transformed potential at the electrode surface in the absence of a buffer layer, and thus

$$\phi_0(0,\nu) = \frac{\phi_0^B(0,\nu)}{\left[\varepsilon_1 \dfrac{\sinh(2\pi|v|d_0) + \alpha\cosh(2\pi|v|d_0)}{\cosh(2\pi|v|d_0) + \alpha\sinh(2\pi|v|d_0)} + \varepsilon_{00}\right]}. \tag{II.35}$$

Finally, if the electrode potential in the absence of a buffer layer can be found, the potential distribution throughout the buffer layer and the $LiNbO_3$ crystal is given analytically by equations (II.21), (II.25), (II.30), and (II.35).

The potential distribution at the electrode surface in the absence of a buffer layer has to be found numerically. A technique for calculating this potential is outlined in [9,11]. It is based on an iterative procedure using Fast Fourier transforms (FFT) to calculate the potential and its normal derivative, and to modify them until the appropriate boundary conditions are satisfied. It consists in principle of the following steps (in the absence of a buffer layer):

1. initial guess of the surface potential $\varphi(0,y)$.

2. FFT this potential.

3. multiply by $-2\pi|\nu|$ and use an inverse FFT to obtain the corresponding normalized electric displacement D_x/ε_{00} at the surface.

4. modify D_x/ε_{00} by setting all values between the electrodes to zero (Neuman type boundary condition).

5. FFT the resulting potential and divide by $-2\pi|\nu|$.

6. Inverse FFT to obtain the modified surface potential. Set the potential on the electrodes to the applied voltage and use an interpolation scheme [12] to make the potential continuous between the electrodes.

7. Repeat the iteration from step 2 until the potential and the electric displacement D_x/ε_{00} satisfy their boundary conditions.

The above procedure converges relatively fast even for very crude initial guesses (usually within 3-4 iterations for a 256 point FFT with a tolerance of 10^{-3}) and can be used for a variety of electrode structures (electrode arrays etc.).

Once the surface potential for a particular electrode configuration is determined, the analytical expressions given previously can be used to calculate the potential distribution (and thus the electric field) at various points in the crystal and for various buffer layer thicknesses.

It is thus possible to calculate the electro-optically induced index change at any point in the crystal for any planar electrode/buffer layer configuration.

II-4. Effective index modelling for active devices

The theory developed in the previous sections must now be integrated with the design of the BPM algorithm. The effective index model is used to reduce the original three dimensional device structure to an effective planar waveguide model in the y-z plane. The optical field evolution is then described by a two dimensional scalar Helmholtz equation which can be solved by a one-dimensional BPM algorithm. Since the optical fields for most integrated optical applications vary slowly along the propagation direction in distances of the order of a wavelength, it is sufficient to approximate the scalar Helmholtz equation by the Fresnel equation. The corresponding BPM algorithm will hence be used for our purposes.

The BPM requires the definition a computational grid in the y direction on which the Fast Fourier transforms are performed. At each grid point y_p, the effective index $n_{eff}(y_p)$ has to be calculated from the dispersion relations given earlier where, below the electrodes, the initial diffusion profile $\Delta n\ f(x)$ is perturbed by the electro-optic effect

$$n(x) = n_b + \Delta n_s\ f(x) + \delta n(x)_{electro-optic} \qquad (II.36)$$

This approach effectively replaces the index profile in the x direction (depth) at each grid point by an effective homogeneous slab waveguide as indicated in Figure II-5.

A Gaussian diffusion profile in the presence of an electro-optical index perturbation in z-cut $LiNbO_3$ is shown in Figure II-6, where the electric field was taken at its maximum below an edge of the center electrode. The resulting effective index variation in the y direction for the 3-electrode structure defined in Figure II-4 is shown in Figure II-7. The normalized electric field E_x for various electrode parameters is shown in Figures II-8a through 8d. Reducing the electrode gap, the center electrode width and the buffer layer thickness increases the electric field strength. Electrode design considerations will be discussed further in chapters IV and V.

II-5. Design optimization procedure

The BPM algorithm combined with the Effective Index Method, together with an accurate representation of electro-optically induced index changes, provides a powerful tool for analyzing both active and passive integrated optical devices. Guided and radiation modes are treated in a uniform manner by the BPM so that very accurate performance data of a particular integrated device can be expected. The theoretical model presented in the previous sections can, in principle, be considered the core of a Computer Aided Design (CAD) tool[1] for integrated optical devices. Provided that accurate data from characterizations of the particular fabrication processes are available, the performance of an integrated device can be simulated, and the influence of certain design parameters on its characteristics determined. The resulting data can then be used to design the required masks for the photo-lithografic fabrication steps to provide an optimal (or desired) performance of the device. The CAD procedure is illustrated in the flowchart given as Figure II-9. The accuracy and usefulness of this design procedure will be investigated in the following chapters.

---

[1] The BPM modelling technique was implemented on a IBM AT personal computer using Microsoft Fortran 4.0. Most simulations were, however, carried out on two micro vax computers to take advantage of their higher processor speed and multi-tasking ability. The typical computing time required per BPM simulation (256 point Fast Fourier Transform) on the IBM AT is 15-30 minutes, depending of the stepsize Δz used and the distance the field is to be propagated (typically 5-9mm).

Appendix II-1: The electrode problem in the absence of a buffer layer

Consider the electrode configuration shown in Figure II-4, but without the buffer layer. The potential φ^B in the regions 1 and -1 is again a solution of Laplace's equation. Thus, in region 1, the potential function can be written as (see equation II.21)

$$\varphi_1^B(x,y) = \int d\nu\ \phi_1^B(0,\nu)\ e^{i2\pi\nu y}\ e^{-2\pi|\nu|x\ \sqrt{\varepsilon y/\varepsilon x}}, \qquad \text{(AII.1)}$$

and in region -1 (see equation II.31) as

$$\varphi_{-1}^B(x,y) = \int d\nu\ \phi_{-1}^B(0,\nu)\ e^{i2\pi\nu y}\ e^{2\pi|\nu|x}. \qquad \text{(AII.2)}$$

The interface conditions are again the continuity of the potential φ^B and of the electric displacement D_x:

$$\begin{aligned} \varphi_1^B(0,y) &= \varphi_{-1}^B(0,y) \\ \varepsilon_x \frac{\partial\varphi_1^B}{\partial x}(0,y) &= \varepsilon_{00} \frac{\partial\varphi_{-1}^B}{\partial x}(0,y). \end{aligned} \qquad \text{(AII.3)}$$

Substituting (AII.1) and (AII.2) into (AII.3) and calculating the derivatives yields immediately for x=0

$$\varepsilon_x \int d\nu\ \phi_1^B(0,\nu)\ e^{i2\pi\nu y}\ (-2\pi|\nu|\ \sqrt{\varepsilon y/\varepsilon x}) =$$

$$\varepsilon_{00} \int d\nu\ \phi_{-1}^B(0,\nu)\ e^{i2\pi\nu y}\ 2\pi|\nu|.$$

And since $\phi_1^B(0,\nu) = \phi_{-1}^B(0,\nu)$, we can write the above equation as

$$\int d\nu\ |\nu|\ \phi_1^B(0,\nu)\ e^{i2\pi\nu y} \left[\sqrt{\varepsilon_x\ \varepsilon_y} + \varepsilon_{00}\right] = 0. \qquad \text{(AII.4)}$$

For the left hand side of (AII.4) to be equal to zero, the integral

$$\int d\nu\ |\nu|\ \phi_1^B(0,\nu)\ e^{i2\pi\nu y} \qquad \text{(AII.5)}$$

must equal zero since the term in the square bracket is simply a scaling factor.

Equation (AII.5) is equivalent to equation (II.34) for the same electrode configuration without the buffer layer:

$$\int d\nu \; |\nu| \; \phi_0(0,\nu) \; e^{i2\pi\nu y} \quad \cdot \tag{II.34}$$

$$\cdot \quad \left[\varepsilon_1 \frac{\sinh(2\pi|v|d_0) + \alpha \cosh(2\pi|v|d_0)}{\cosh(2\pi|v|d_0) + \alpha \sinh(2\pi|v|d_0)} + \varepsilon_{00} \right] = 0.$$

with $\alpha = \sqrt{\varepsilon x \varepsilon y} \,/\, \varepsilon_1$

It can thus be recognized by comparing (II.34) with (AII.5) that as d_0 goes to zero, $\phi_0(0,\nu)$ will approach the potential $\phi_0^B(0,\nu)$, the transformed potential at the electrode surface in the absence of a buffer layer, and thus

$$\phi_0(0,\nu) = \frac{\phi_0^B(0,\nu)}{\left[\varepsilon_1 \dfrac{\sinh(2\pi|v|d_0) + \alpha \cosh(2\pi|v|d_0)}{\cosh(2\pi|v|d_0) + \alpha \sinh(2\pi|v|d_0)} + \varepsilon_{00} \right]} \,. \tag{AII.6}$$

References:

1 Van Roey, J., van der Donk, J. and Lagasse, P.E., 'Beam-propagation method: analysis and assessment,' *J. Opt. Soc. Am.*, 71, 7, pp. 803-809, 1981.

2 Neyer, A., Mevenkamp, W., Thylén, L., and Lagerström, B., 'A BPM analysis of active and passive waveguide crossings,' *J. Lightwave Tech.*, LT-3, pp. 635-642, 1985.

3 Thylén, L., 'Integrated optics: Recent developments in devices for telecommunications,' *J. Lightwave Techn.*, LT-6, 6, pp. 847-861, 1988.

4 Hocker, G.B., and Burns, W.K.. 'Mode dispersion of diffused channel waveguides by the effective index method,' *Appl. Opt.*, 16, 1, pp. 113-118, 1977.

5 Kaminow, I.P., *An Introduction to Electrooptic Devices*, Springer Verlag, Berlin, W. Germany, 1974.

6 Alferness, R.C., 'Guided-wave devices for optical communication,' *IEEE J. Quant. Electron*, QE-17, pp. 946-959, 1981.

7 Gottlieb, M., Ireland, C.L.M., and Ley, J.M., *Electro-optic and Acousto-optic Scanning and Deflection*, Marcel Dekker Inc., New York, 1983.

8 Rahmer, O.G., 'Integrated optic electrooptic modulator electrode analysis,' *IEEE J. Quantum Electron.*, QE-18, pp. 820-825, 1982.

9 Thylén, L. and Granestrand, P., 'Integrated optic electrooptic device electrode analysis: the influence of buffer layers,' *J. Opt. Commun.*, 7, 1, pp. 11-14, 1986.

10 Weast, R.C., *Handbook of lasers*, CRC Press, Cleveland, 1971.

11 Hartmann, C.S. and Secrest, B.G., 'End effects in interdigital surface wave transducers,' *IEEE Ultrasonic Symposium*, pp. 413-416, 1972.

12 A spline interpolation scheme was used in this case. See for example:
Press, W.H., Flannery, B.P., Teukolsky, S.A., and Vetterling, W.T., *Numnerical Recipes*, Cambridge University Press, Cambridge, 1986.

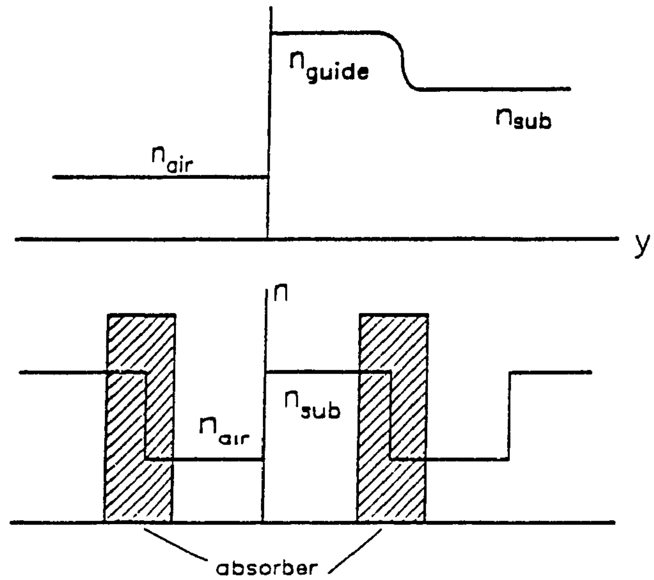

Figure II-1 *Illustration of assuming a periodic extention of the refractive index step between the guide and air [1].*

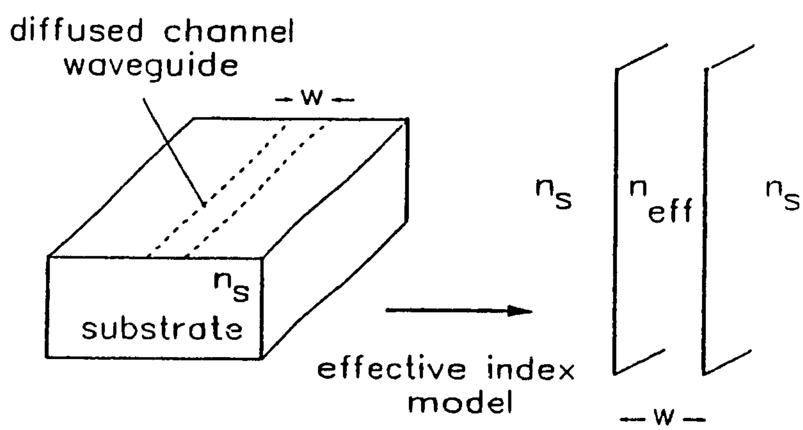

Figure II-2 *Illustration of the effective index model of a channel waveguide.*

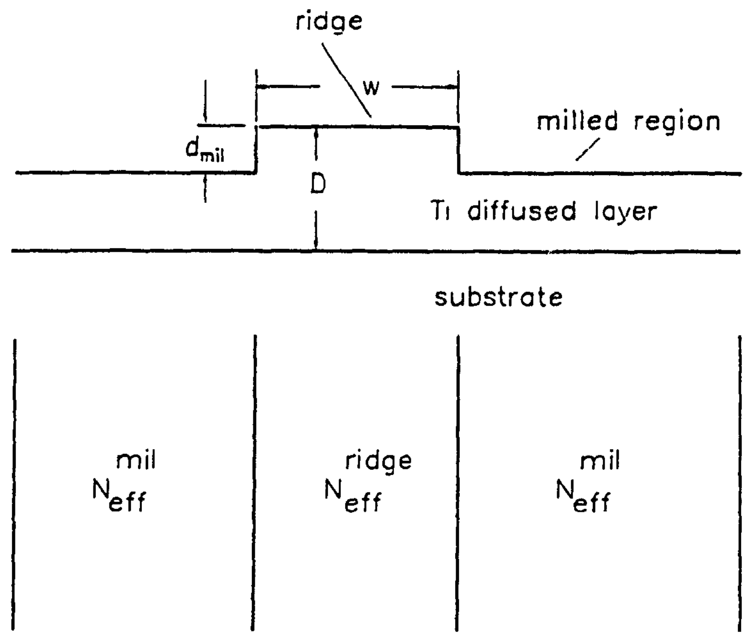

Figure II-3 *Ridge waveguide and corresponding effective index model.*

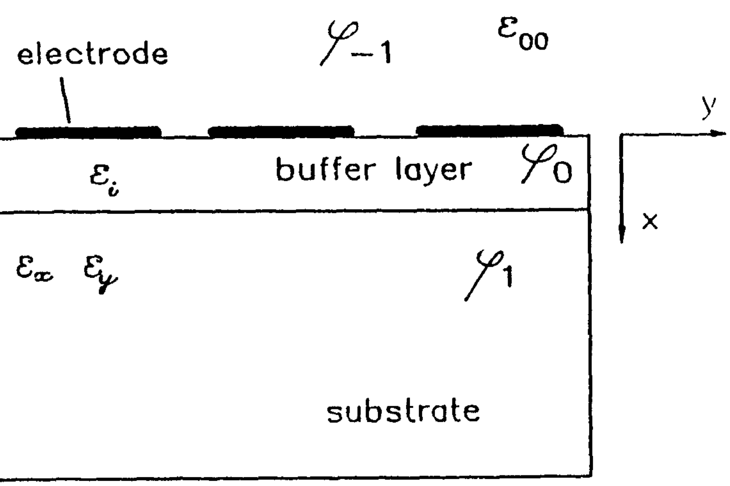

Figure II-4 *Electrode configuration including buffer layer.*

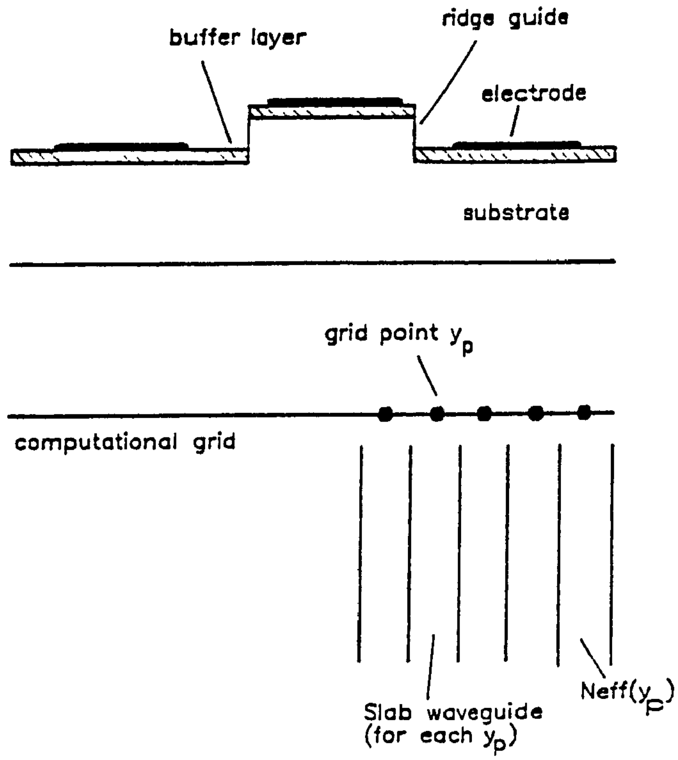

Figure II-5 *Illustration of the effective index model and the computational grid.*

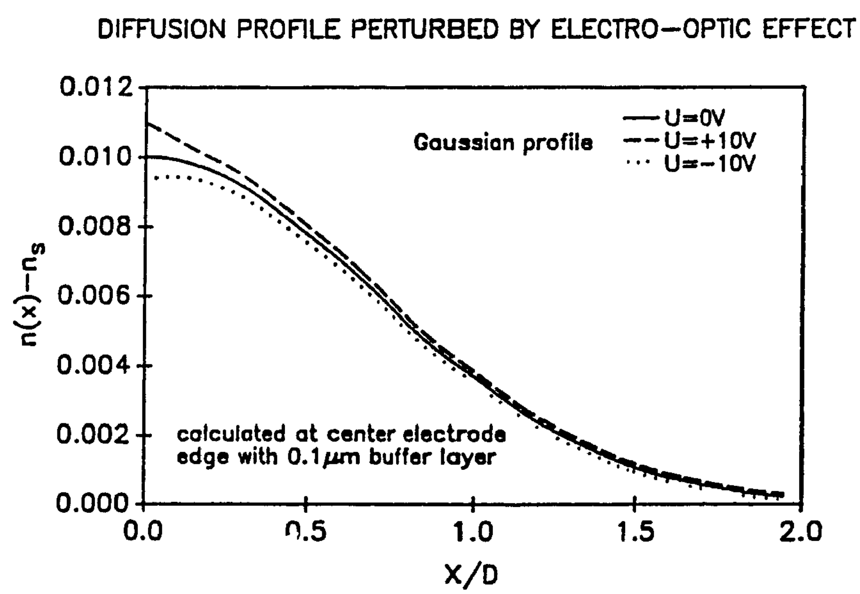

Figure II-6 *Gaussian diffusion profile perturbed by the electro-optic effect.*

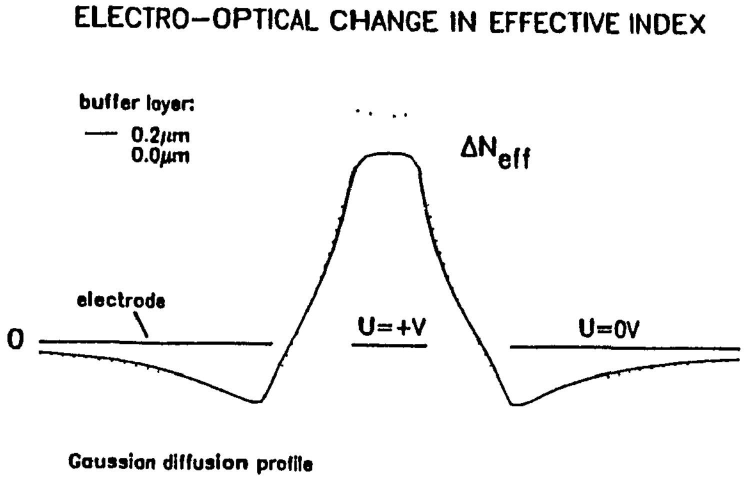

Figure II-7 *Electro-optically induced change in effective index.*

(a) (b)

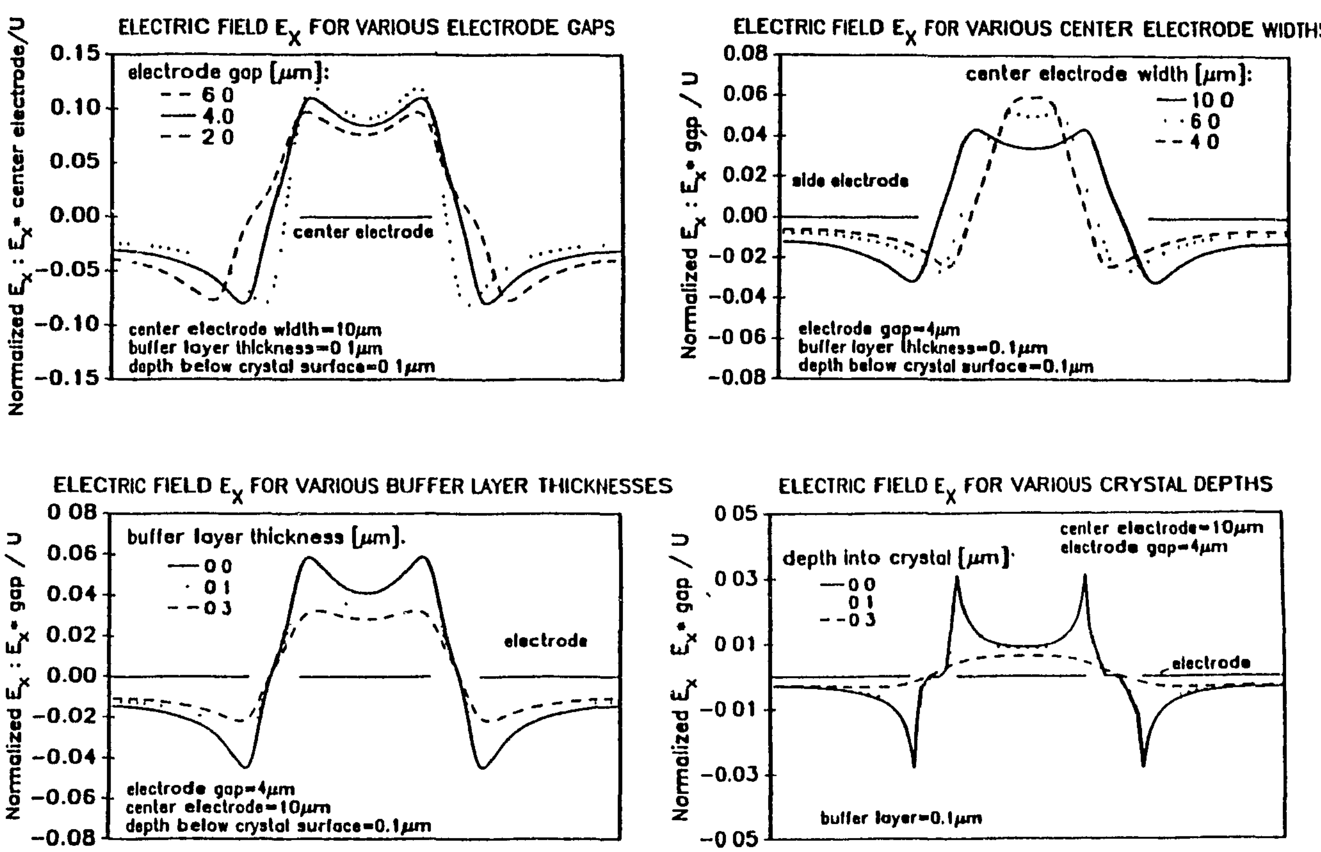

(c) (d)

Figure II-8 *Normalized electric field E_x for various: (a) electrode gaps, (b) center electrode widths, (c) buffer layer thicknesses, and (d) depths into substrate.*

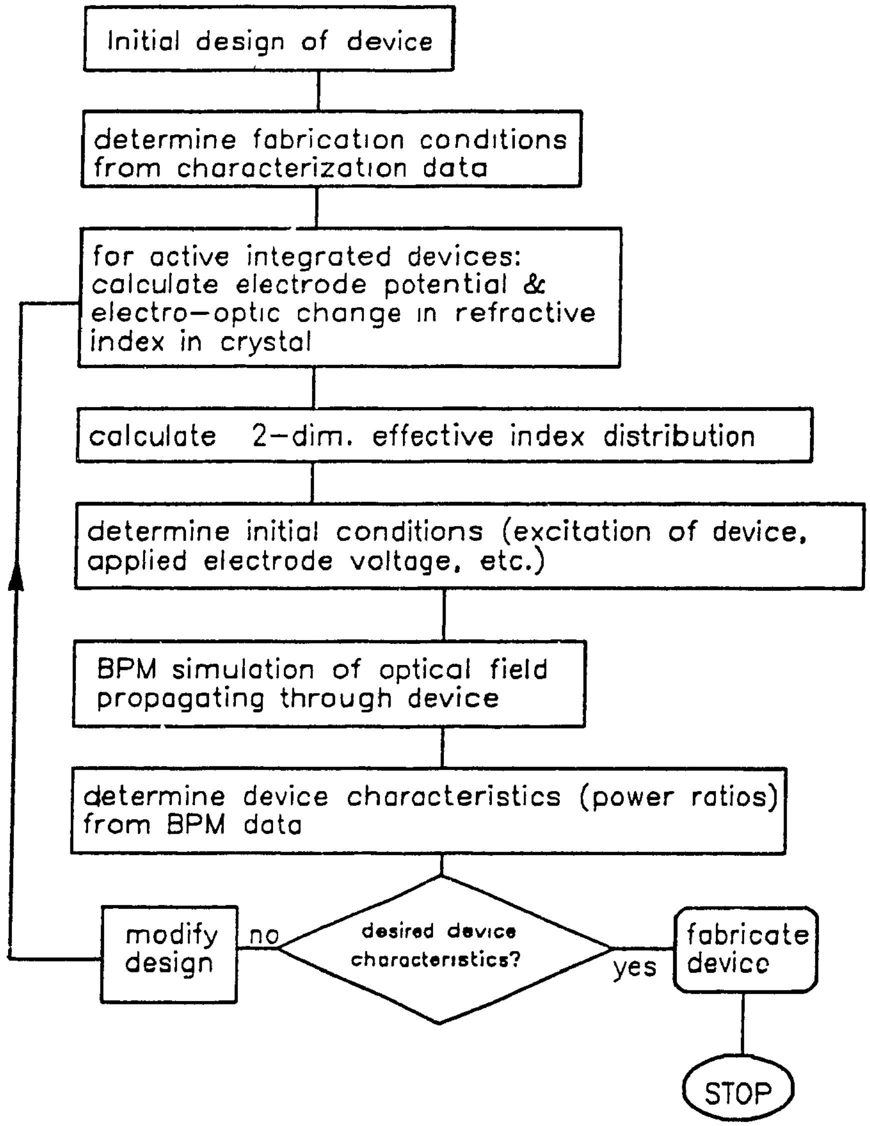

Figure II-9 *Flow-chart of the BPM optimization procedure.*

CHAPTER III. DESIGN ANALYSIS OF SYMMETRIC AND ASYMMETRIC PASSIVE 3-BRANCH POWER DIVIDERS

III-1. Introduction

Branching waveguides form very promising and basic structures in integrated optical circuits. Both active and passive Y-junctions in $LiNbO_3$ have been investigated as power dividers, TE-TM splitters, switches and modulators [1,2]. The use of 3-branch junctions for optical power division has also been investigated [3-5]. In these structures, a uniform index distribution in the branches leads to more power being transmitted into the central branch. Equal power division among the three branches can be achieved by selectively depositing a dielectric cladding on the outer waveguide regions, thereby increasing the effective index of the respective channel waveguides slightly.

The previous theoretical model used to calculate the optical field and the power distribution in the device was based on a field-matching technique [4]. The accuracy of the new BPM design technique will be established by comparing its results to the theoretical and experimental ones previously published by Haruna *et. al.* [5]. Design curves for a symmetric 3-branch passive power divider with equal power division are presented. Also, the idea of controlling the power distribution in the branches by means of a dielectric cladding is expanded to include the asymmetric case where the cladding thickness on arm 1 differs from that on arm 3. This allows asymmetric power division ratios such as 1:3:2 to be achieved. The design curves for asymmetric power division are also presented.

III-2. Principle of Operation

The geometry and dimensions of this device are given in Figure III-1. The shaded areas denote a dielectric cladding of thickness d_1 (on arm 1) and d_3 (on arm 3). The channel waveguides were fabricated by K^+-ion exchange in a soda-lime glass substrate (n_b=1.512) through an Al mask immersed in KNO_3 at 370°C for one hour. This yields single-mode channel waveguides with an estimated diffusion depth D of 1.53μm and a surface index increase of 0.0107 [6]. The index profile in the depth coordinate is Gaussian. To increase the index in the taper and branch regions of arm 1 and 3, a layer of Corning glass (7059, $n_c \cong$ 1.544) was RF sputtered onto the relevant regions.

Using these fabrication data, the effective index of the diffused channel guides can be calculated by solving the dispersion relation for an equivalent inhomogeneous slab waveguide (equation II.8). The effective index n_{eff} obtained can then be substituted in the dispersion relation for a homogeneous slab waveguide to obtain the equivalent index n_f [7]. The increase in the effective index in the waveguide regions under the cladding is obtained by solving the dispersion relation for the TM modes in the homogeneous slab guide of thickness d_2, covered on top by a uniform cladding of thickness d_1 and index n_c, and then free space, and bounded below by an infinite medium of index n_b (substrate) [4]:

$$k_2 \left[1 - \frac{k_2}{\gamma_3} \tan k_2 d_2 \right] \left[\tan k_1 d_1 + \frac{k_1}{\gamma_4} \right]$$

$$- k_1 \left[1 - \frac{k_2}{\gamma_3} \tan k_2 d_2 \right] \left[\tan k_1 d_1 + \frac{k_1}{\gamma_4} \right] = 0, \qquad \text{(III.1)}$$

where

$$k_1 = (k_0^2 n_f^2 - \beta^2)^{1/2}$$
$$k_2 = (k_0^2 n_c^2 - \beta^2)^{1/2}$$
$$\gamma_3 = (\beta^2 - k_0^2)^{1/2}$$
$$\gamma_4 = (\beta^2 - k_0^2\, n_b^2)^{1/2}.$$

β is the propagation constant of the fundamental mode in the slab characterized by the equivalent index n_f.

The optical field distribution in the device is then calculated by propagating an eigenmode along this effective index model using the Beam Propagation Method, and finally calculating the power in each arm. This permits a detailed study of the power transmission properties as a function of various device parameters, in particular, the influence of different cladding thicknesses on the device performance.

III-3. BPM Results

The increase in effective index due to the dielectric cladding on the outer branches is plotted in Figure III-2 for different thicknesses. The increase in effective index does not vary linearly with $d_{1,3}$. It increases more rapidly for thicker cladding layers. This means that if a large change in effective index is desired, even small variation in cladding thickness will significantly alter the power division ratio.

The power distribution in the individual branches and the ratio of the outer to central branch power as a function of the cladding thickness are given in Figure III-3 for the symmetric case ($d_1=d_3$). The cladding thickness required for equal power division among the three branches is estimated, from Figure III-3, to be 0.215μm. This compares favourably to the experimental result of 0.2μm published in [5]. The optical field distribution in the device for the equal power division case is shown in Figure III-4. The theoretical behavior of the power distribution in the branches (Figure III-3), calculated by BPM, compares to the results published in [5]. The increase of the total power transmitted through the device with increasing cladding thickness, indicated in Figure 3 of [5], can physically not be justified. The BPM calculations indicate higher scattering losses in the device as more and more power is forced into the outer two branches (decrease in P_{tot} in Figure III-3), which is consistent with physical intuition.

In a similar manner, the use of an asymmetric cladding of arm 1 and arm 3 ($d_1 \neq d_3$) allows other power division ratios to be achieved. Figure III-5a through 5c show the power distribution in the individual branches as a function of the cladding thickness on arm 3, with d_1=1000Å, 2500Å, and 3000Å, respectively. The plots of the total power P_{tot} transmitted through the device pass through a maximum when the cladding on arm 1 equals that on arm 3 (symmetric case).These curves can be used to design power dividers with asymmetric division ratios. For example, a cladding of 1000Å and 1450Å on arm 1 and 3, respectively, allows the input of power to be divided according to 1:3:2. The field distribution in the device for this splitting condition is shown in Figure III-6.

III-4. Discussion and Conclusion

In this chapter, we have demonstrated that, with the previously published characterization data [6] on the K^+-ion exchanged slab waveguides and employing the Effective Index and Beam Propagation Methods, highly accurate theoretical models can be set up for design calculations. The theoretical cladding thickness of 0.215μm compares extremely well with the measured value of 0.2μm for equal power division. The beam propagation simulations presented in Figures III-4 and III-6 offer an interesting visual observation of the beam evolution in the designed devices. The design procedure outlined here can also be applied to power dividers made by proton-exchange or Ti in-diffusion into $LiNbO_3$. Corresponding Ti:$LiNbO_3$ design curves are included in chapter V, where the possibility of using a dielectric cladding to overcome the switching bias of an active 3-branch switch will be investigated.

This passive 3-branch power divider should prove to be a useful device for optical power division from one fiber into three according to a specified ratio. The design method developed here allows the appropriate fabrication parameters to be determined easily and very accurately. The results presented in this chapter led to publication [8].

References:

1 Saski, H., and De La Rue, R.M.,'Electro-optic Y-junction modulator/switch,' *Electron. Lett.*, 12, pp. 459-460, 1976.

2 Masuda, M., and Yip, G.L., 'An optical TE-TM mode splitter using a $LiNbO_3$ branching waveguide,' *Appl. Phys. Lett.*, 37, pp.20-22. 1980.

3 Bélanger, M., Yip, G.L., and Haruna, M., 'Passive planar multibranch optical power divider: some design considerations,' *Appl. Opt.*, 22, pp.2382-2389, 1983.

4 Bélanger, M., and Yip, G.L., 'A passive three-branch optical power divider in $LiNbO_3$,' *Fiber and Integrated Optics*, 5, 1, pp. 65-79, 1984.

5 Haruna, M., Bélanger, M., and Yip, G.L., 'Passive 3-branch optical power divider by K^+-ion exchange in glass,' *Electron. Lett.*, 21, 12, pp.535-536, 1985.

6 Yip, G.L., and Albert, J., 'Characterization of planar optical waveguides by K^+-ion exchange in glass,' *Opt. Lett.*, 10, pp. 151-153, 1985.

7 Tamir, T., *Integrated Optics*, Springer Verlag, New York, 23, 1974.

8 Yip, G.L. and Sekerka-Bajbus, M.A., 'Design of symmetric and asymmetric passive power dividers by the beam propagation method,' *Electron. Lett.*, 24, 25, pp. 1584-1586, 1988.

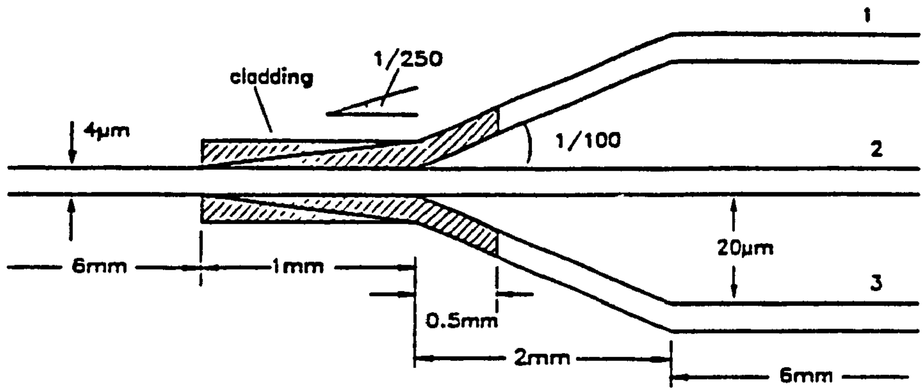

Figure III-1 *Device configuration.*

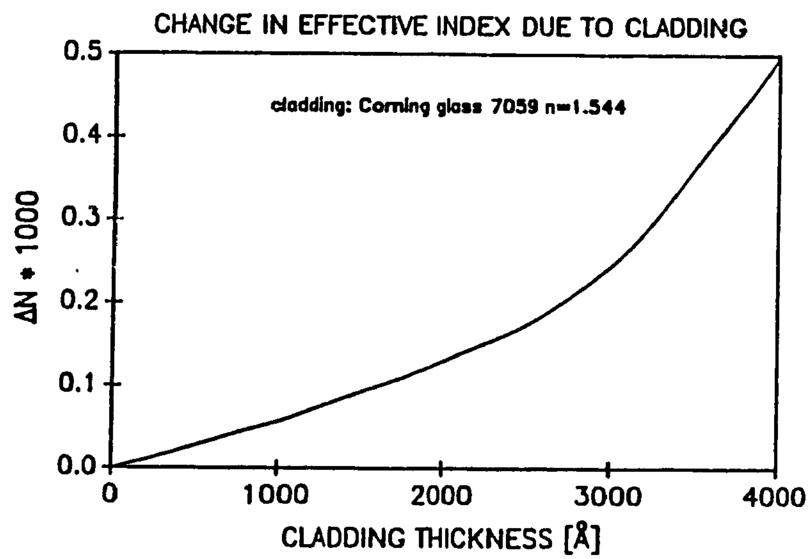

Figure III-2 *Change in effective index due to a dielectric cladding of thickness d.*

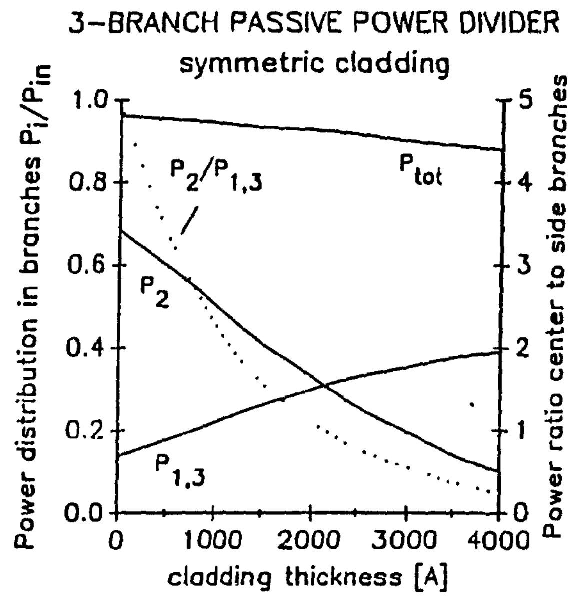

Figure III-3 *Symmetric case: power distribution in individual branches and ratio of center to outer branch power.*

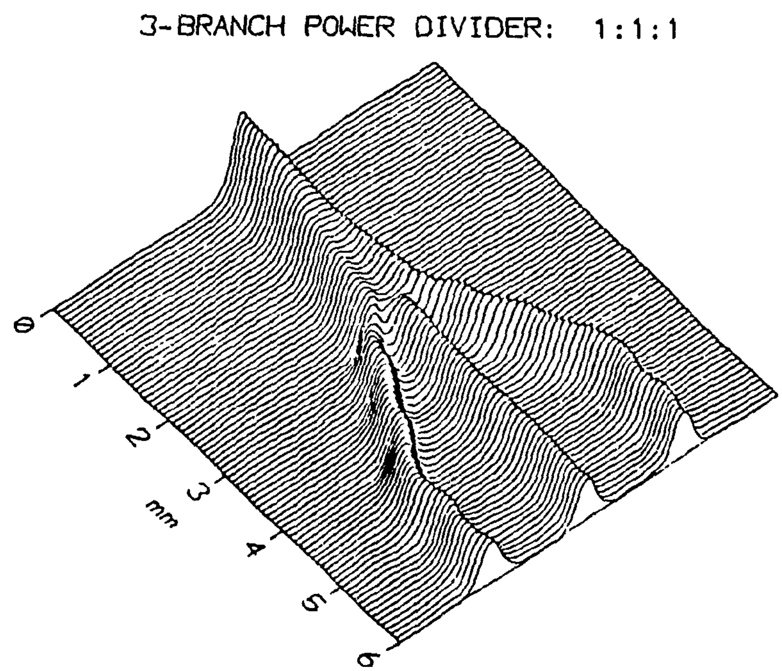

Figure III-4 *Optical field distribution for equal power division.*

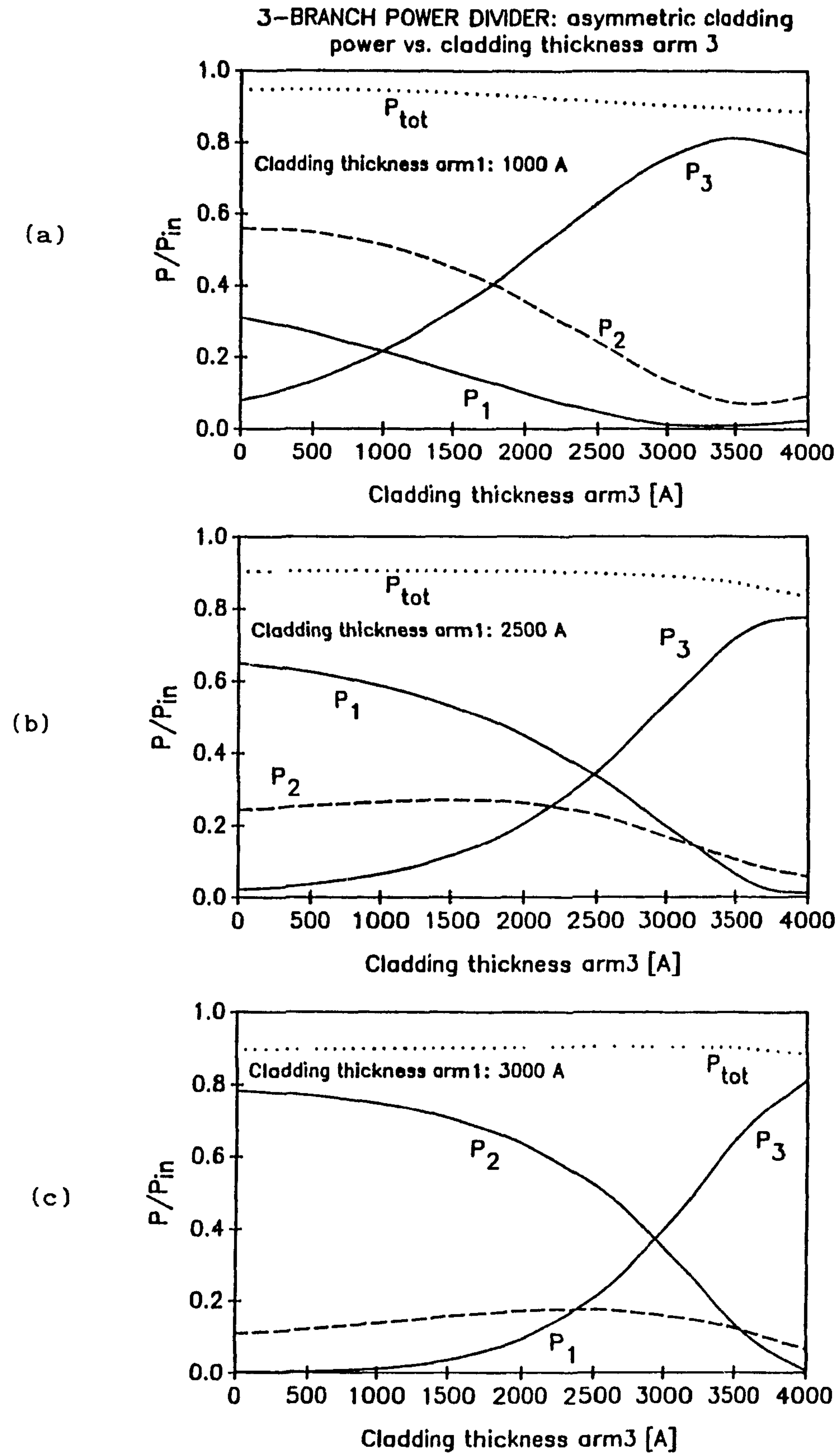

Figure III-5 *Asymmetric case: power distribution in individual branches as a function of d_3 for (a) d_1=1000Å, (b) d_1=2500Å, and (c) d_1=3000Å.*

3-BRANCH POWER DIVIDER: 1:3:2

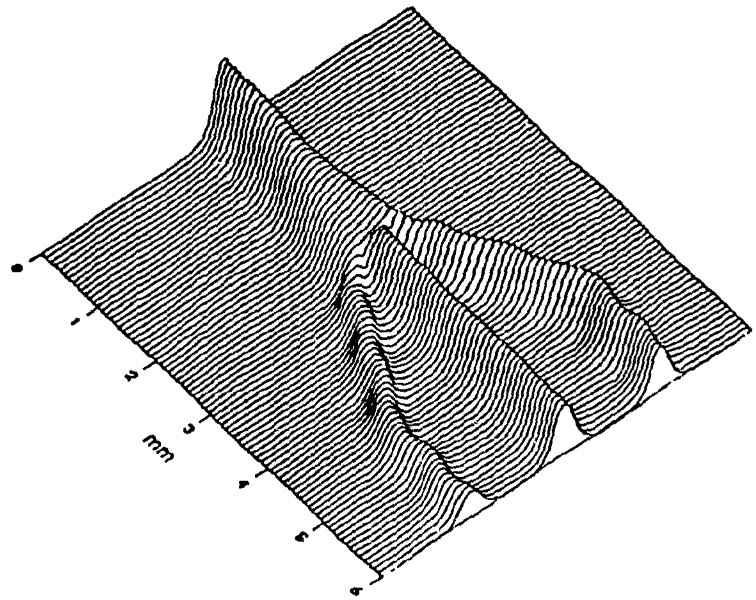

Figure III-6 *Optical field distribution for a division ratio of 1:3:2.*

CHAPTER IV. Design Optimization Of A Ti:$LiNbO_3$ Ridge Waveguide Linear Mode Confinement Modulator Fabricated by Ion-beam Milling

IV-1. Introduction

Electro-optic modulators and switches form very basic devices in optical communication systems. Several types of high-speed phase and intensity modulators on $LiNbO_3$ for the external modulation of laser diodes in fiber-optic systems have recently been investigated [1-3]. While these devices generally exhibit a large bandwidth and require small drive voltages, their output intensity does not vary linearly with the drive signal. Also, high-speed base-band operation of these devices (for reasons of drive voltage) require device lengths of several millimeters and thus do not permit high packing densities.

In the past, mode extinction (cut-off) modulators with linear modulation characteristics have been studied [4,5]. These devices operate by electro-optically bringing a section of a channel waveguide above or below cut-off, thus modulating the optical power transmitted through the device. This, however, makes the device sensitive to variations in the material and the fabrication conditions. This device type also has the tendency to excite unwanted substrate modes in the OFF-state of the modulator. Some power in the substrate modes can be recoupled into the output waveguides, hence limiting the extinction ratio.

Recently, the feasibility of a novel linear mode confinement modulator in Ti in-diffused z-cut $LiNbO_3$ with a modulation depth[1] of over 90% was shown [6]. A similar ridge waveguide device fabricated by reactive ion-beam etching (RIBE) with a poorer performance of 67% and a drive voltage of ±20V was also reported [7]. Unlike the linear cut-off modulators mentioned earlier, these devices do not require operation around the cut-off point which greatly relaxes the fabrication conditions. Furthermore, the device geometry and dimensions allow for a high packing density.

When conceived, the ridge waveguide device reported in [7] was expected to perform better than the one described in [6] because of the stronger confinement of the optical waves by the ridge waveguiding structure made by RIBE. The subsequent poorer performance (67% modulation depth) was believed to be mainly due to a non-optimal design and an excessively thick buffer layer for the electrodes, which reduces the electro-optical effects for the same applied voltage.

In this chapter, the experimental improvement of the ridge waveguide device, now fabricated by ion-beam milling (not RIBE), to a modulation depth of over 97% with a drive voltage of only ±8V is discussed. Results of design calculations aiming at optimizing the modulator design for single-mode operation are also presented.

IV-2. Principle of Operation

The device configuration of the line modulator is shown in Figure IV-1. The device consists of two channel waveguides (regions 1 & 3)

---

1 modulation depth = $(P_{max} - P_{min}) / P_{max} * 100\%$

connected by an intermediate slab waveguide (region 2). As the optical waves enter the slab region from the input ridge guide, the guided modal field starts to diverge so that, at the mouth of the output guide, the overlap between the excited optical field and the guided modal field of the output guide is reduced, resulting in only a fraction of the input power being transmitted into the output guide. A variable lateral confinement of the modes in the slab waveguide, and thus an increase in the modal field overlap, is achieved by electro-optically inducing a channel waveguide in region 2, thus providing a modulated transmission between regions 1 and 3. If the voltage polarity is reversed, the optical waves are scattered away from the output guide, resulting in a further reduction in the transmission. A branch structure at the end of the slab region assists in separating the scattered and output modes. The modulator can be considered a derivative of an active 3-branch waveguide switch reported earlier [8].

IV-3. Theoretical Model and Analysis

A theoretical analysis of the modulator requires the calculation of the transmitted power across the slab region into the output guide as a function of the applied electrode voltage. The theoretical method used previously [7] was based on a mode matching technique and did not properly account for the scattered modes in the slab region. Furthermore, the electrode analysis was based a conformal mapping solution of the potential problem which neglected the attenuating influence of the buffer layer used to separate the electrodes from the crystal surface. The more sophisticated theoretical model developed in the previous chapters will now be used for a design oriented analysis of the mode confinement modulator.

The effective index distribution describing the device is found by replacing each point along the crystal surface with a homogeneous slab waveguide of an effective index $n_{eff}(y,z)$, equivalent to the diffused waveguide, and solving the dispersion relation (II.8). The lower integration limit x_0 in equation (II.8) is zero for the ridge guide and equal to the milling depth d_{mil} in the milled regions. The refractive index distribution n(x,y,z) is assumed to follow a Gaussian distribution along the x-axis and is, below the electrodes, perturbed by the electro-optical effect (equation II.36). The attenuating influence of the SiO_2 buffer layer on the electric field is taken into account as outlined in section II-3.

Figure IV-2 shows the effective index distribution in the slab region for both voltage polarities (ON- and OFF-state). The optical field distribution in the device is then calculated by propagating an eigenmode along this two-dimensional effective index model using the BPM. The output power in a particular mode is determined from the BPM data by over-lapping the output modal field in region 3 with its normalized guided mode.

The effective index of the ridge structure can be controlled very accurately through the milling depth d_{mil}, which in turn determines the number of lateral modes (m+1) supported by a ridge waveguide of width w. According to [12],

$$m = \mathrm{INT}\left\{ 2\,\frac{w}{\lambda}\sqrt{\left[n_{eff}^{ridge}\right]^2 - \left[n_{eff}^{mil}\right]^2} \right\},\ m=0,1,2,\ldots \qquad \text{(IV.1)}$$

$\Delta N = \left\{\left[n_{eff}^{ridge}\right]^2 - \left[n_{eff}^{mill}\right]^2\right\}^{1/2}$ is plotted versus λ/w in Figure IV-3a with the number of modes supported as a parameter. The wavelength λ is chosen to be 0.6328μm. This curve can be used to estimate the maximum permitted value of ΔN for single-mode operation. n_{eff}^{ridge} is fixed by the diffusion conditions and can be determined from equation (II.8). It is independent of the milling depth so that the d_{mill} to match the desired ΔN can be found iteratively from equation (II.8). Figure IV-3b shows a plot of ΔN versus the milling depth for a Gaussian diffusion profile with a surface index increase Δn_s of 0.01 and 0.005, respectively, and a diffusion depth of D=2.0μm. These two curves are most useful in designing ridge waveguides supporting m+1 lateral modes.

Figures IV-4a and b show the optical field calculations for a TM mode propagating through a multi-mode modulator at an applied voltage of +5V and -5V (side electrode grounded). The device parameters are given in Table IV-1 and are consistent with those of an actual device fabricated (section IV-5, sample 2). The confinement of the optical mode in the induced channel waveguide, as it propagates through the slab region, is clearly observable in Figure IV-4a. The scattering of excess power along the branch structure, away form the mouth of the output ridge guide, is also visible, particularly for the OFF-state. Some conversion of optical power to second and third order modes is observable at the mouth of the output guide for both voltage polarizations. For this device, 10 to 15% of the transmitted power propagates in these higher order modes, that value having been calculated by overlapping the output modal field in region 3 with its normalized guided mode of appropriate order m.

Table IV-1: Fabrication parameters - 10 μm Line Modulator

Sample	*1*	*2*	*3*
Titanium film thickness	117Å	114Å	116Å
Δn_s	0.01	0.01	0.01
Diffusion depth	2.0	2.0	2.0
Milling depth [μm]	0.2	0.3	0.3
N_{eff} (ridge)	2.2038	2.2038	2.2038
N_{eff} (milled)	2.2031	2.2028	2.2028
Number of modes supported	2	3	3
Modulation length L		1.0mm	
Branch angle α		2.58°	
Branch length b		1.0mm	
Ridge width w		10.0μm	
Center electrode width		8.0μm	
Inter electrode gap		4.0μm	
Buffer layer [μm]	0.26	0.08	0.16

Comments: *Sample* 1 electrode misalignment <5μm
2 good electrode alignment
3 electrode misalignment <3μm

IV-4. Design Optimization

The design procedure developed in the previous chapters will now be used to redesign the line modulator for single-mode operation. The influence of varying certain design parameters on the modulation characteristics can be determined elegantly from the BPM simulation. Such calculations are most useful in optimizing the modulator design for a desired performance prior to the actual experimental work.

The desired device characteristics, in order of importance, are: 1) a good modulation depth (>90%) and linearity of the output intensity with respect to the applied voltage; 2) a small drive voltage (<±5V); and 3) compact device dimensions. Fabrication tolerances, however, may impose limitations on the achievable device design.

The width of the input/output ridge guide was chosen to be 6μm with an initial corresponding center electrode width and inter-electrode gap of 4μm. The latter value reflects the resolution limit of our mask aligner (Cobilt CA 400). The maximum permitted milling depth for single-mode operation was then determined from Figures IV-3a and 3b to be 0.17μm, with Δn_s=0.01 and D=2.0μm. The SiO_2 buffer layer used to separate the electrodes from the crystal surface was chosen to be 0.1μm thick.

Based on these parameters, the influence of the modulation length L and the branch angle α on the device performance are shown in Figure IV-5a and 5b, respectively. Clearly, increasing the modulation length reduces the drive voltage required to achieve a total extinction of power in the output guide (OFF-state) and leads thus to a high modulation depth. Reducing the branch angle α from the value of 2.58° used in [7] somewhat improves the device performance. In particular, an examination of the optical field distribution in the device indicates that, if α is chosen too large, the guided and scattered modes are not properly separated along the branch structure. This results in large radiation mode amplitudes appearing in the vicinity of the output field, particularly when the modulator is driven in its OFF-state. This point is illustrated in Figure IV-5c for a single-mode device based on the photo-mask used in [7] with an α of 2.58°. The optical field evolution for the corresponding multi-mode device is shown Figure IV-5d. The same branch structure succeeds here in separating the guided and scattered fields. Large branch angles (>1.5°) can consequently be used in multi-mode devices with a larger ridge height. For single-mode operation, an angle of 1.0° provides good separation of the scattered modes and is, from a fabrication point of view, easily achievable. The length of the branch structure b has little influence on the device performance provided its dimension is similar to that of the modulation length L. In Figure IV-5e, the modulation characteristics for different milling depths are shown. Accordingly, the device performance is critically dependent of the milling depth and an "optimal" value within the range permitted for single-mode operation can be determined for a particular device design.

The resolution limit of our mask aligner does not permit the reliable fabrication of structures smaller than 4μm. With respect to fabricating the electrodes, we are already operating at that resolution limit and only a limited optimization of the electrode parameters is feasible. Figure IV-5d show the modulation characteristics for center electrode widths of 4μm and 5μm with inter electrode gaps of 4μm. Increasing the center electrode width to 5μm improves the device performance slightly.

From such considerations it is possible, in an iterative manner, to deduce those device parameters required to realize a desired performance. Figure IV-6a shows the modulation characteristics for various modulation lengths L after optimizing the other design parameters. The modulation characteristics change only marginally for lengths greater than 2.5mm, indicating a limit to the extent L can be used to adjust the OFF-state drive voltage. The modulator design which best matches the desired device characteristics mentioned earlier is summarized in Table IV-2. Its modulation characteristics for various milling depths are also shown in Figure IV-6b. This optimized design has a theoretical modulation depth 95% at a required drive voltage of ±5V, with an effective device length L of only 2.5mm.

In a similar manner, the performance of a modulator based on the mask design used in [7] can be improved by optimizing its mask-independent parameters. With a buffer layer of 0.1μm and diffusion parameters of Δn_s=0.01 and D=2.0μm, the influence of the milling depth is shown in Figure IV-7 for devices supporting up to 3 lateral modes.

Table IV-2 Device parameter of an optimized 6μm line modulator

Surface index change Δn_s	0.005
Diffusion depth D	2.0μm
Ridge height d_{mill}	0.1μm
Modulation length L	2.5mm
Branch angle α	1.0°
Branch length b	1.0mm
Ridge width w	6.0μm
Center electrode width	5.0μm
Inter electrode gap	4.0μm
Buffer layer thickness d	0.1μm
Number of lateral modes supported in in/output guide	1

The device performance is best for single-mode operation. However, a milling depth of less than 0.05μm is difficult to achieve experimentally and the input coupling using a prism to such a shallow ridge guide somewhat problematic. Also, since the mask design is based on a branch angle of 2.58°, the separation of scattered and guided modes will be poor, as discussed earlier. To avoid these difficulties, a milling depth of 0.3μm is chosen. The resulting modulator supports 3 lateral modes and provides good modulation depth and linearity with a relatively small drive voltage of ±10V. This result will be verified experimentally in the following sections.

IV-5. Fabrication of a Ridge Line Modulator

Three line modulators with a ridge width of 10μm were fabricated from the original mask design [7]. First, a titanium thin film was evaporated onto a cleaned $LiNbO_3$ substrate and the metal diffused into the crystal at 975°C for 4 hours in a flowing argon atmosphere and a further 2 hours in flowing oxygen to prevent out-diffusion. This creates a single-mode slab waveguide with an estimated diffusion depth and surface-index change at λ=0.6328μm of 2.0μm and 0.01, respectively. Using photo-lithography, the appropriate ridge structure of height d_{mil} was ion-beam milled out of the slab waveguide. The milling process was calibrated for an argon/oxygen (7:3) pressure of $4*10^{-4}$ torr with an angle of incidence of the ion beam with respect to the sample of 30°. A milling rate of 0.03μm/hr was determined at a beam energy and ion current of 7 keV and 30 A, respectively. The sample was consequently annealed for 2 hours at 500°C to repair the surface damage created during the milling process. At this point, the designated output end of the substrate was optically polished to permit endfire coupling.

Next, a thin SiO_2 buffer layer was RF sputtered onto the sample, followed by further annealing in oxygen for 2 hours. Finally, the electrodes were formed by evaporating an aluminum film on top of the buffer layer, and, using photo-lithography, removing the redundant metal with a ($H_3PO_4:HNO_3:CH_3COOH:H_2O$ = 16:1:2:1) chemical solution. Table IV-1 summarizes the achieved fabrication parameters of the three devices. A micrograph of a sample after the ion-milling step is shown in Figure IV-8. The photo mask allows for several modulators to be fabricated on one substrate. The individual modulators have common slab regions to permit a higher packing density of the devices. Figure IV-9 shows a micrograph of slab and output regions of the completed device designated Sample 1. A misalignment of the center electrode with respect to the modulator axis is clearly visible (<5μm). Sample 3 displays a similar but smaller electrode misalignment (<3μm). The micrograph of Sample 2, given as Figure IV-10, shows perfect alignment of the electrodes with the ridge waveguide.

The fabricated devices were then mounted on holders for proper connection of the electrodes. The electrodes were connected using 50μm gold wire and a silver conductive epoxy. Figure IV-11 shows a fabricated device together with its holder.

IV-6. Measurement of a line modulator

The experimental setup used to measure the modulation characteristics of the fabricated devices is shown in Figures IV-12a and 12b. A 0.6328μm He-Ne laser beam was TM-polarized and focussed through a microscope objective lens onto a prism which was used to couple light into the input ridge guide. At the output end, light leaving the ridge guide was focussed through a second microscope lens onto a photo-detector connected to an oscilloscope. The drive voltage applied to the electrodes from the function generator was a slowly varying ramp.

Figures IV-13a through 13c show the measured output intensity against the applied drive voltage for samples 1,2, and 3, respectively. The measured performance of all three devices is included in Table IV-3. All devices display good modulation depths (>90%) and linearity with respect to the applied voltage. The higher drive voltage required for samples 1 and 3 of ±15 V is partly due to the slightly thicker buffer layer and the electrode misalignment, compared to that of sample 2. The drive voltage for device 2 has been reduced to ±8V. This result constitutes a considerable improvement over previously published results [7]. This is primarily due to a thinner buffer layer and a reduced ridge height (permits less lateral modes). The fabricated modulators support 2 and 3 modes, respectively. The optical field distributions for sample 2 for an applied voltage of +5V and -5V are given in Figure IV-4 and were discussed in section IV-3.

Figures IV-14a through 14c compare the theoretical modulation characteristics of the devices with experiment. Both qualitative and quantitative agreement between the two can be observed. The theoretically predicted drive voltage necessary for maximum modulation depth in sample 2 (good electrode alignment) is slightly higher than the experimental result. Saturation of the output power in both the ON- and OFF-state of the modulator is reached at ±8V, somewhat earlier than the theoretically predicted level of ±10V. Increasing the voltage beyond the saturation point actually leads to a decrease in device performance due to increased scattering in the device. The good correspondence between experiment and theory, never reached with the previous device in [7], confirms the validity of the BPM model and its applicability for design optimization purposes.

Table IV-3: Comparison between experimental & theoretical results

	Drive voltage range [V]		*Modulation depth*	
	theor.	*exp.*	*theor.*	*exp.*
Sample 1	-17.5V, +20V	-20V, +15V	97%	91%
Sample 2	-10V, +10V	-8V, +8V	99%	97%
Sample 3	-15V, +20V	-15V, +15V	95%	98%

IV-7. Discussion and Conclusion

An improved ridge waveguide modulator with a modulation depth of 97% and a drive voltage of -8V to +8V has been presented. The improvement in the experimental performance of this modulator over the results reported in [7] is mainly due to a reduced buffer layer thickness and an optimization of the ridge height. A theoretical analysis based on an accurate effective index model combined with the Beam Propagation Method was used to predict the performance of the device. This model provides an elegant tool for determining the influence of various device parameters (modulation length, guide width etc.) on the modulation characteristics. Such calculations are useful in optimizing a particular device design for a desired performance prior to the actual experimental work. This procedure was used successfully to optimize the performance of a modulator based on the photo-mask design used in [7]. The good correspondence between experiment and theory confirms the validity of the BPM model and its applicability for design optimization purposes.

This design procedure was also used to redesign the line modulator for single-mode operation. The resulting smaller modulator with a 6μm guide width and an optimized geometry has a theoretical modulation depth of 95% with a drive voltage of ±5V. Experimental results for this device are, however, not available.

The optimization of the line modulator presented here was based on pure device performance parameters such as the modulation depth, output linearity and the drive voltage. For direct application in a single-mode fiber system, the problem of efficient fiber to waveguide coupling would also have to be considered in the design process. Possible tradeoffs between the diffusion and milling parameters required for good coupling and those for efficient modulation could be compensated for by increasing the device length, thus reducing the drive voltage to the desired level. The design procedure used here can be applied to a wide variety of integrated optical devices and should prove to be very useful in the future. The experimental results presented in this chapter led to a conference presentation [13], and a more detailed paper has been submitted for publication [14].

References:

1 Sueta, T., and Izutsu, M., 'High speed guided-wave optical modulators,' *J. Opt. Commun.*, 3, pp. 52-58, 1982.

2 Auracher, F., Schicketanz, D., and Zeiller, K.-H., 'High-speed $\Delta\beta$-reversal directional coupler modulator with low insertion loss for 1.3μm in $LiNbO_3$,' *J. Opt. Commun.*, 5, pp. 7-9, 1984.

3 Becker, R.A., 'Travelling-wave electrooptic modulator with maximum bandwidth-length product,' *Appl. Phys. Lett.*, 45, pp. 1163-1170, 1984.

4 Neyer, A. and Sohler, W.,'High speed cutoff modulator using a diffused $LiNbO_3$ channel waveguide,' *Appl. Phys. Lett.*, 35, 3, pp. 256-258, 1979.

5 Ashley, P.R., and Chang, W.S.C., 'Improved mode extinction modulator using a Ti in-diffused $LiNbO_3$ channel waveguide,' *Appl. Phys. Lett.*, 45, 8, pp. 840-842, 1984.

6 Bélanger, M., and Yip, G.L., 'Novel Ti:$LiNbO_3$ linear mode confinement modulator,' *Electron Lett.*, 22, 5, pp. 252-253, 1986.

7 Bélanger, M., and Yip, G.L., 'A novel Ti:$LiNbO_3$ ridge waveguide linear mode confinement modulator fabricated by reactive ion-beam etching,' *J. Lightwave Techn.*, LT-5, 9, pp. 1257-1263, 1987.

8 Bélanger, M., and Yip, G.L., 'Theoretical and experimental investigation of an active 3-branch Ti:$LiNbO_3$ waveguide switch,' *Appl. Optics*, 28, 1, pp. 53-59, 1989.

9 Neyer, A., Mevenkamp, W, Thylén, L., and Lagerström, B., 'A beam propagation method analysis of active and passive waveguide crossings,' *J. Lightwave Techn.*, LT-3, pp. 635-642, 1985.

10 Hocker, G.B., and Burns, W.K., 'Mode dispersion of diffused channel waveguides by the effective index method,' *Appl. Opt.*. 16, 1, pp. 113-118, 1977.

11 Thylén, L., and Granestrand, P., 'Integrated optic electrooptic device electrode analysis: the influence of buffer layers,' *J. Opt. Commun.*, 7, 1, pp. 11-14, 1986.

12 Tamir, T., *Integrated Optics*, Springer Verlag, New York, 23, 1974.

13 Sekerka-Bajbus, M.A., Goto, N., and Yip, G.L., 'An improved $LiNbO_3$ ridge waveguide linear mode confinement modulator by ion-beam milling,' *Proc. S.P.I.E. Integrated Optical Circuit Engineering VI*, 993, pp. 102-109, 1988.

14 Sekerka-Bajbus, M.A., Yip, G.L., and Goto, N., 'BPM design optimization and experimental improvement of a Ti:$LiNbO_3$ ridge waveguide linear mode confinement modulator,' submitted for publication to the *J. Lightwave Techn.*

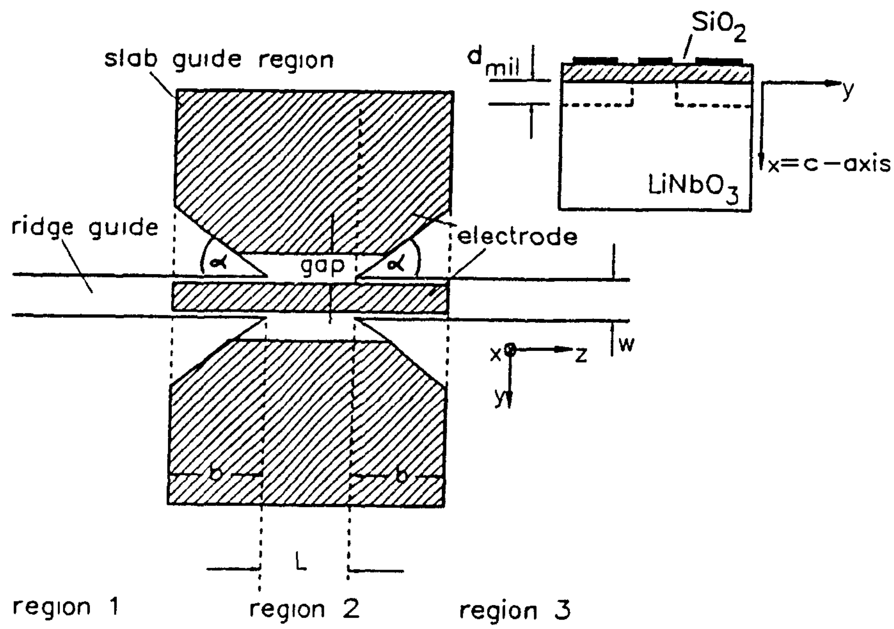

Figure IV-1 *Device configuration.*

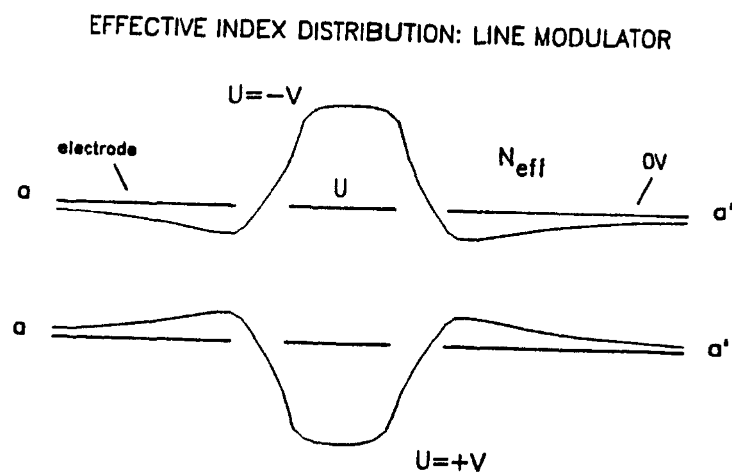

Figure IV-2 *Effective index distribution in the slab region for the ON- and OFF-state.*

(a)

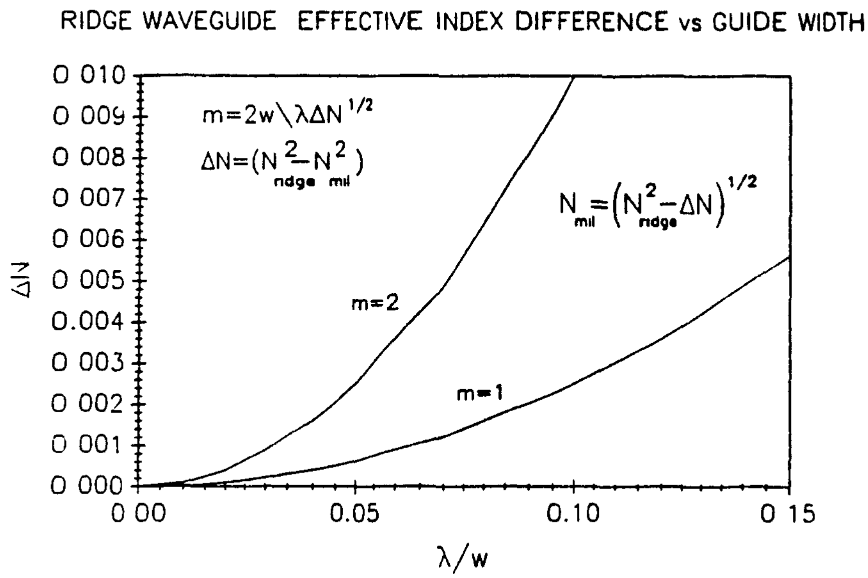

(b)

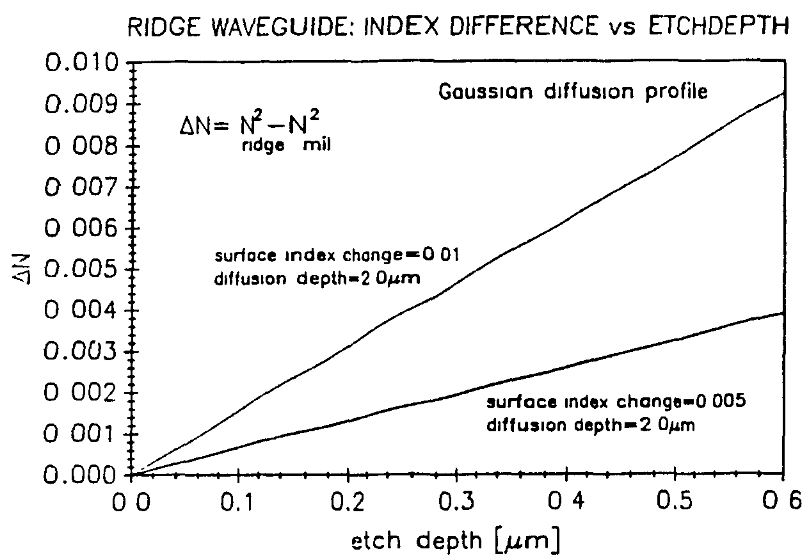

Figure IV-3 *Ridge waveguide design curves: (a) ΔN versus λ/w and (b) ΔN versus milling depth for a surface index change* Δn_s=0.01 *and* 0.005, *respectively, and a diffusion depth of* 2.0μm.

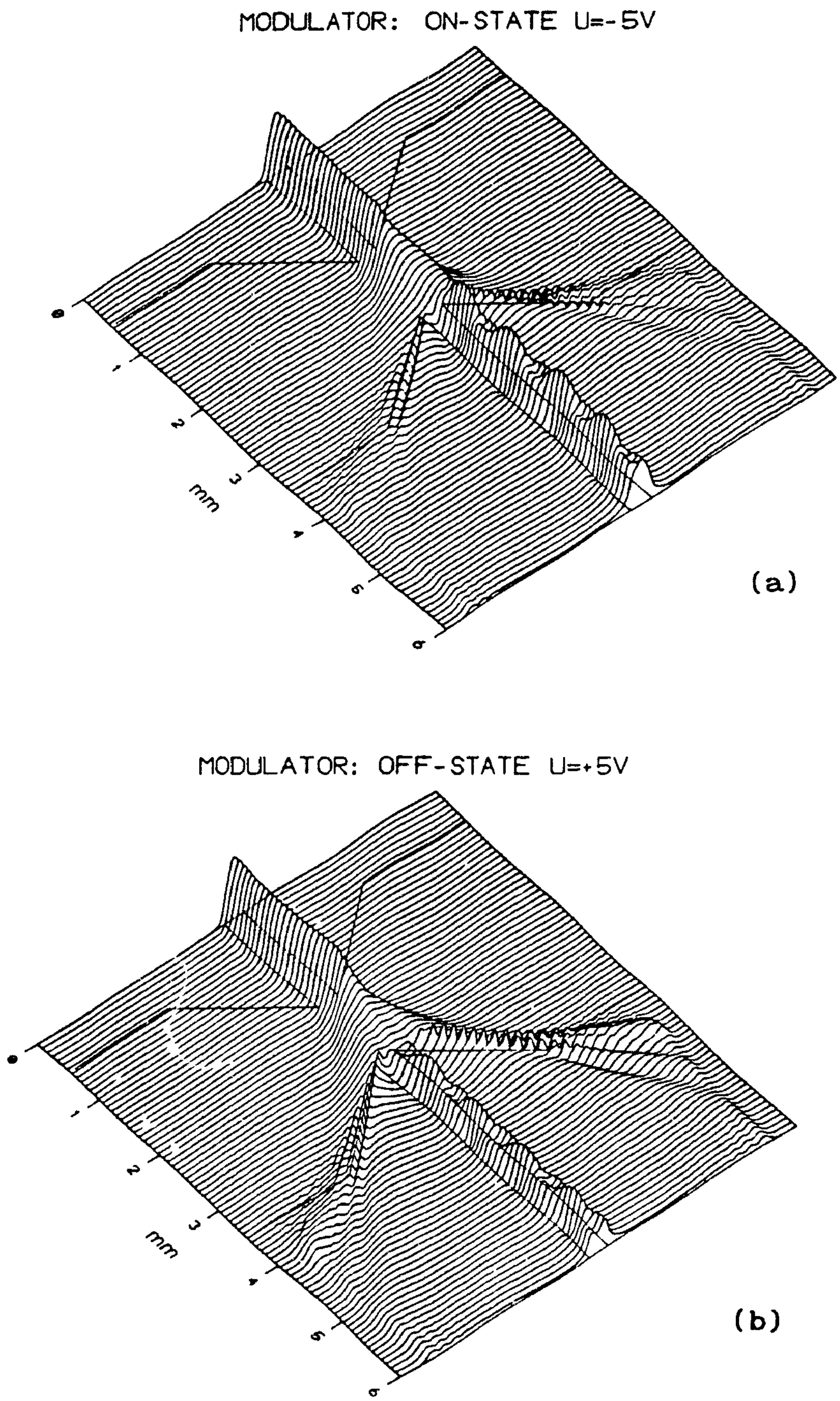

Figure IV-4 *Optical field distribution in the modulator for the (a) ON-state, and (b) OFF-state.*

(a)

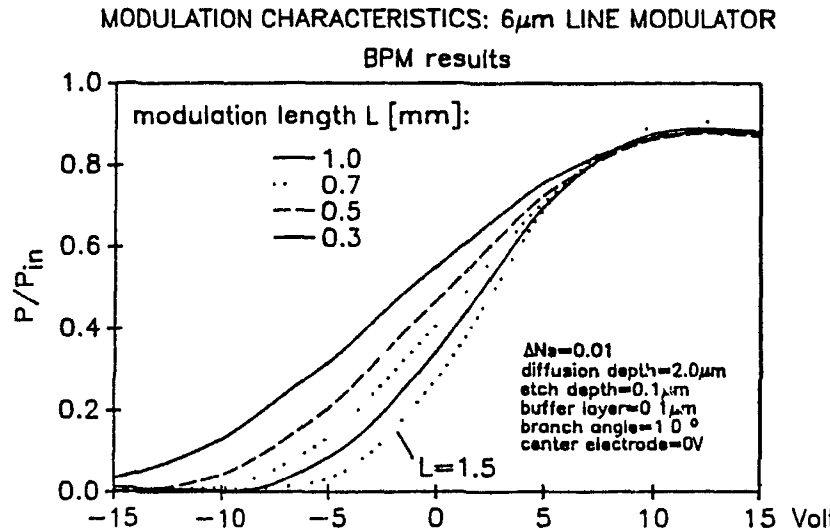

(b)

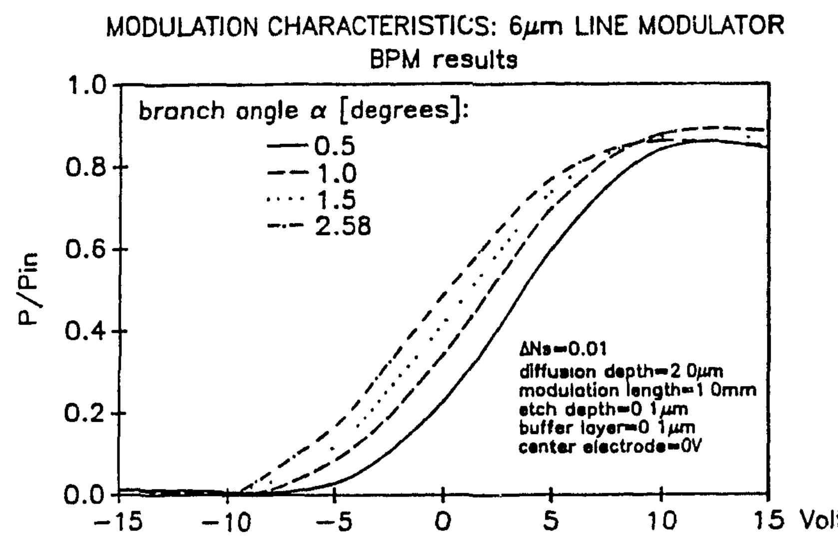

Figure IV-5 *Modulation characteristics of a 6μm modulator for various (a) modulation lengths L, (b) branch angles α.*

MODULATOR (OFF-state): SINGLE-MODE, LARGE ANGLE

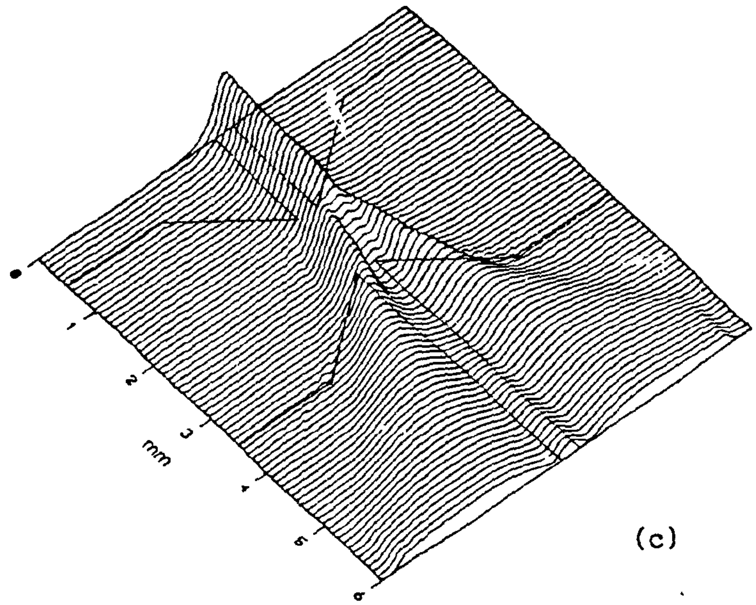

(c)

MODULATOR (OFF-state): MULTI-MODE, LARGE ANGLE

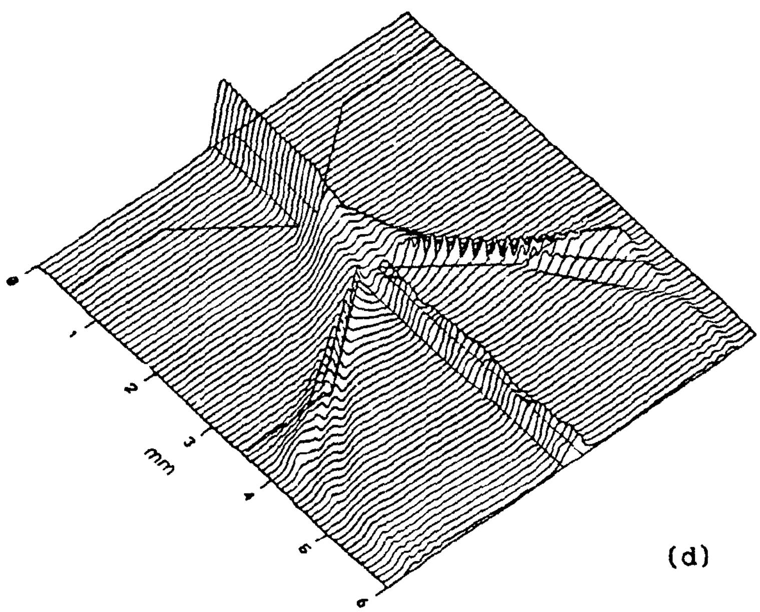

(d)

Figure IV-5 *(c) Optical field distribution for a single-mode modulator with a large branch angle (α=2.58°), (d) for the corresponding multi-mode device (3 lateral modes).*

(e)

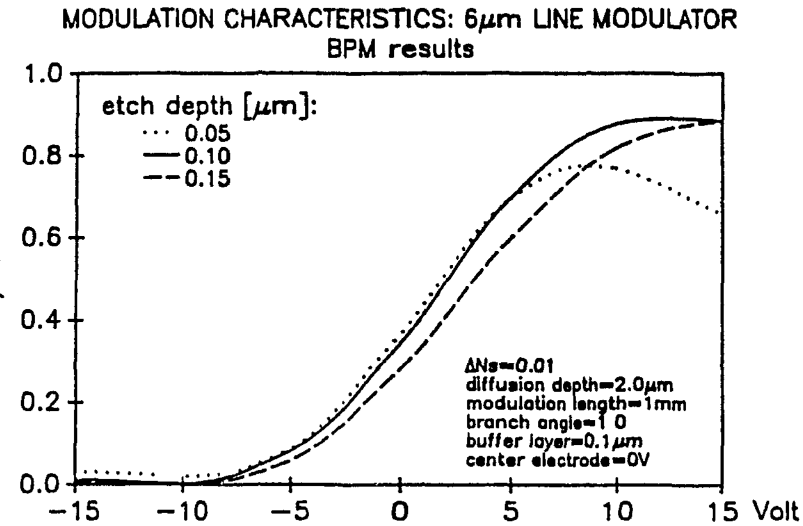

(f)

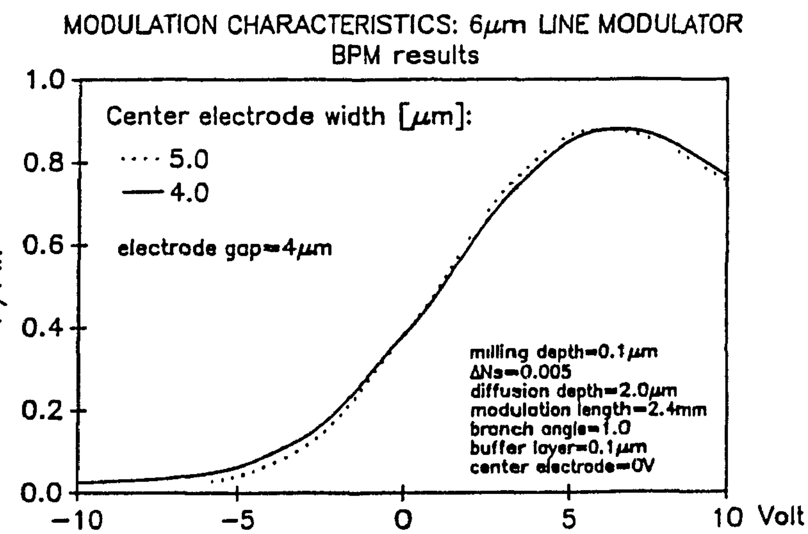

Figure IV-5 *(e) Modulation characteristics of a 6μm modulator for various milling depths, (f) for various center electrode widths.*

(a)

(b)

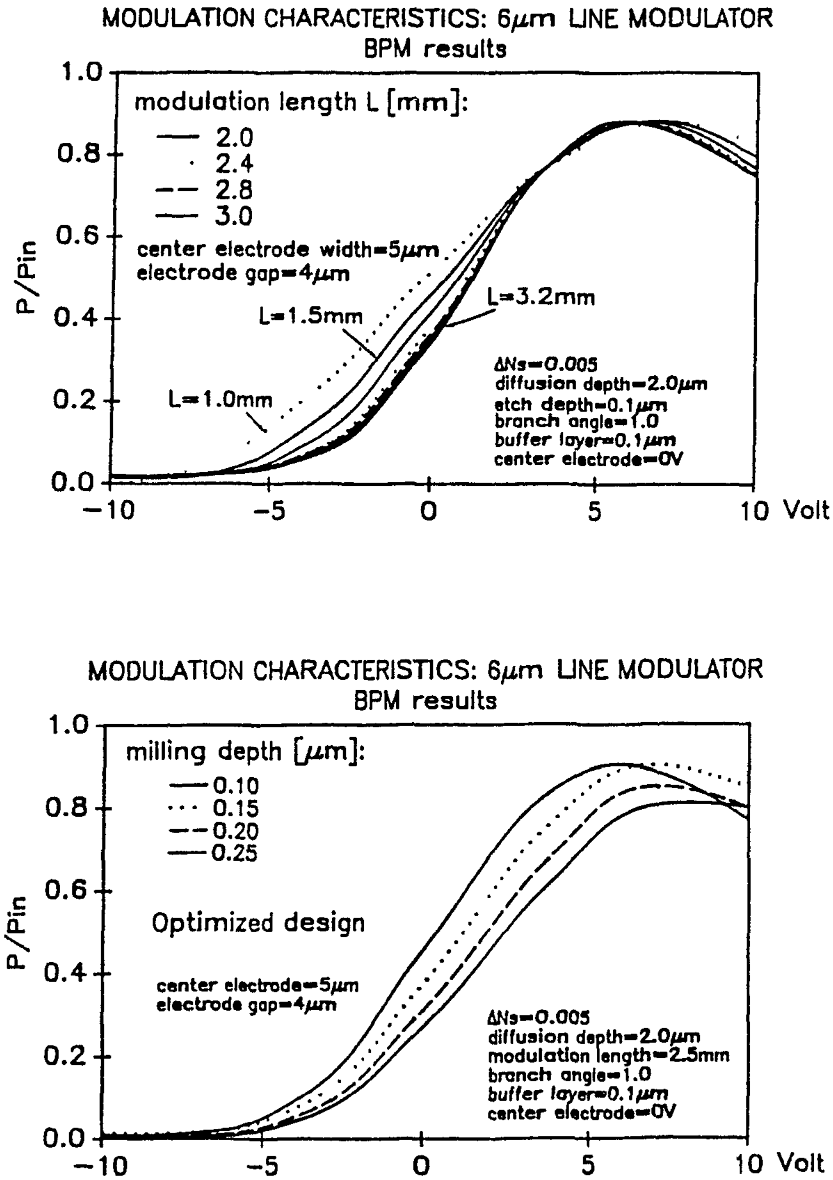

Figure IV-6 *Modulation characteristics of the optimized 6μm modulator for various (a) modulation lengths L, and for various (b) milling depths.*

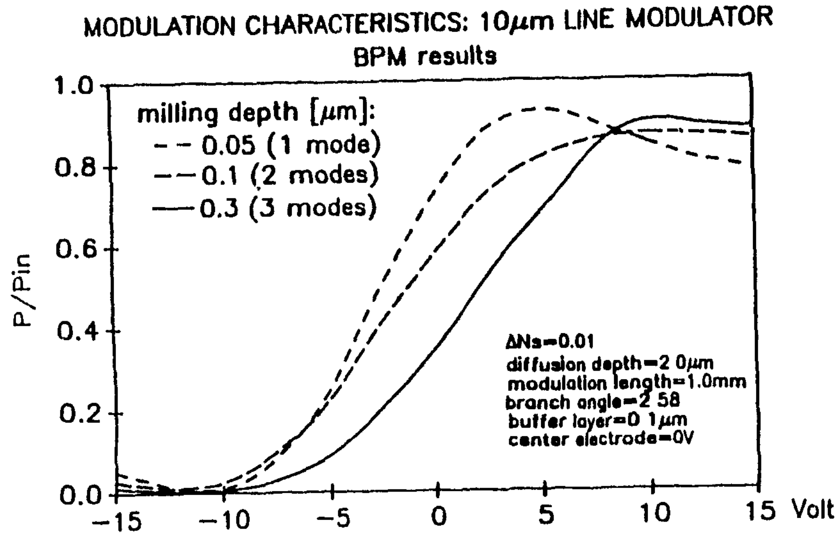

Figure IV-7 *Modulation characteristics of a 10μm modulator for various milling depths.*

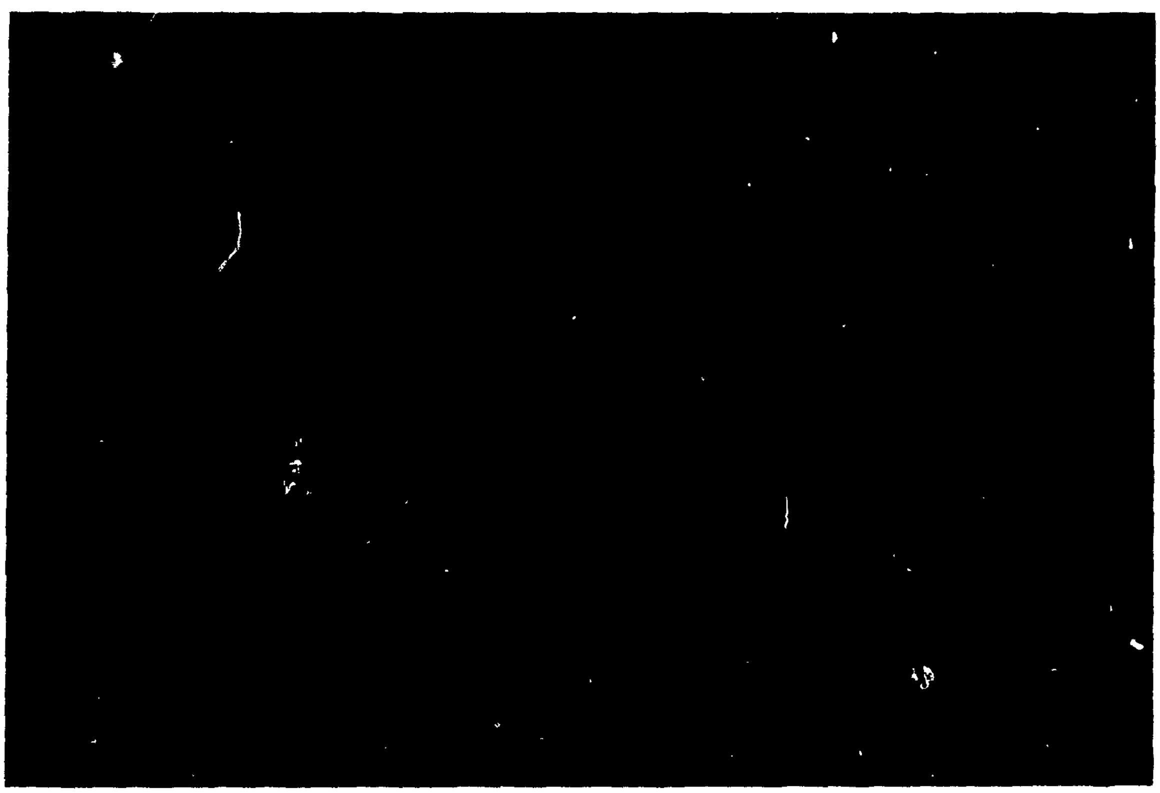

Figure IV-8 *Micrograph of a sample after the ion-milling step.*

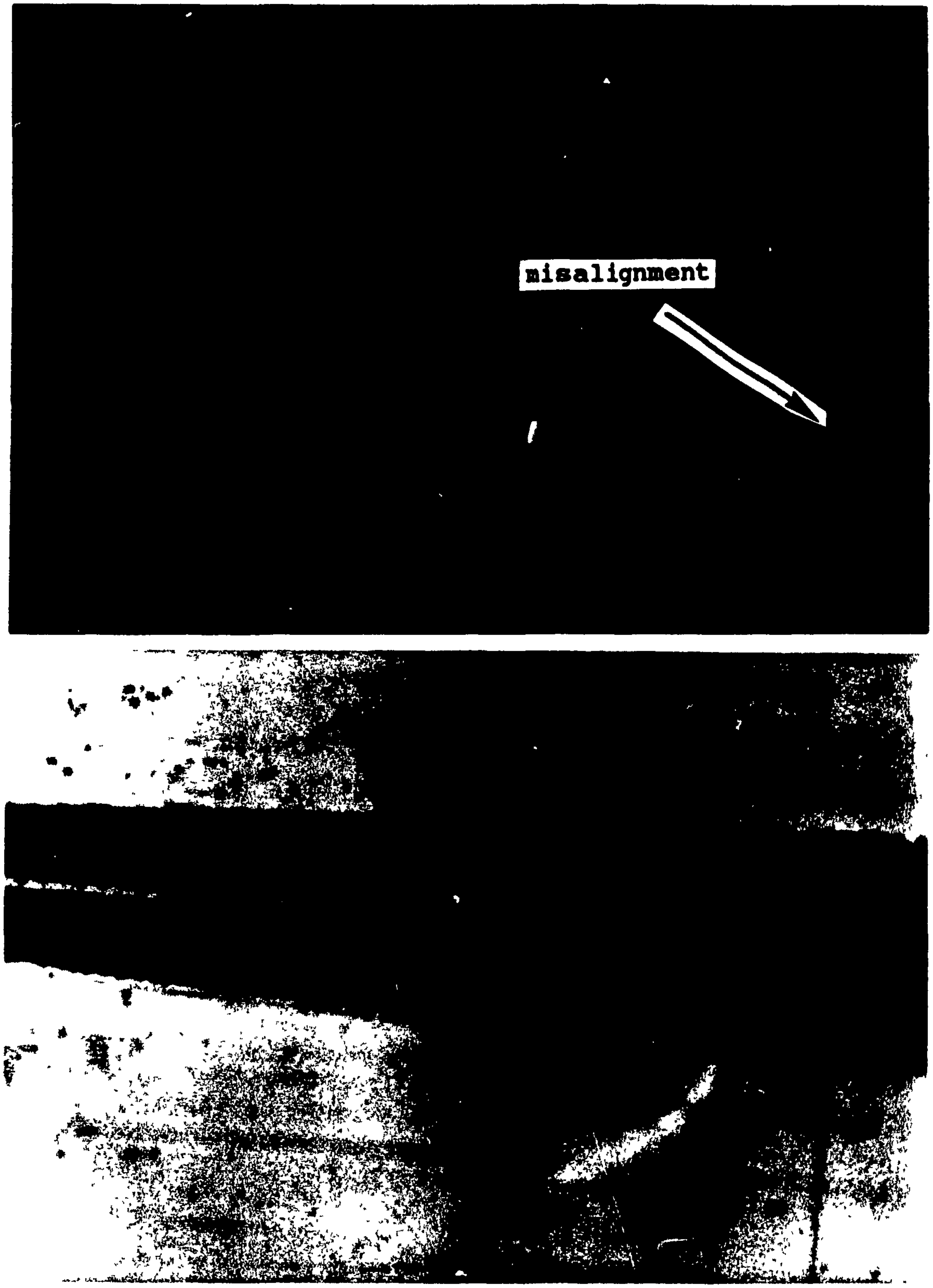

Figure IV-9 *Micrographs of sample 1 with axial electrode misalignment visible.*

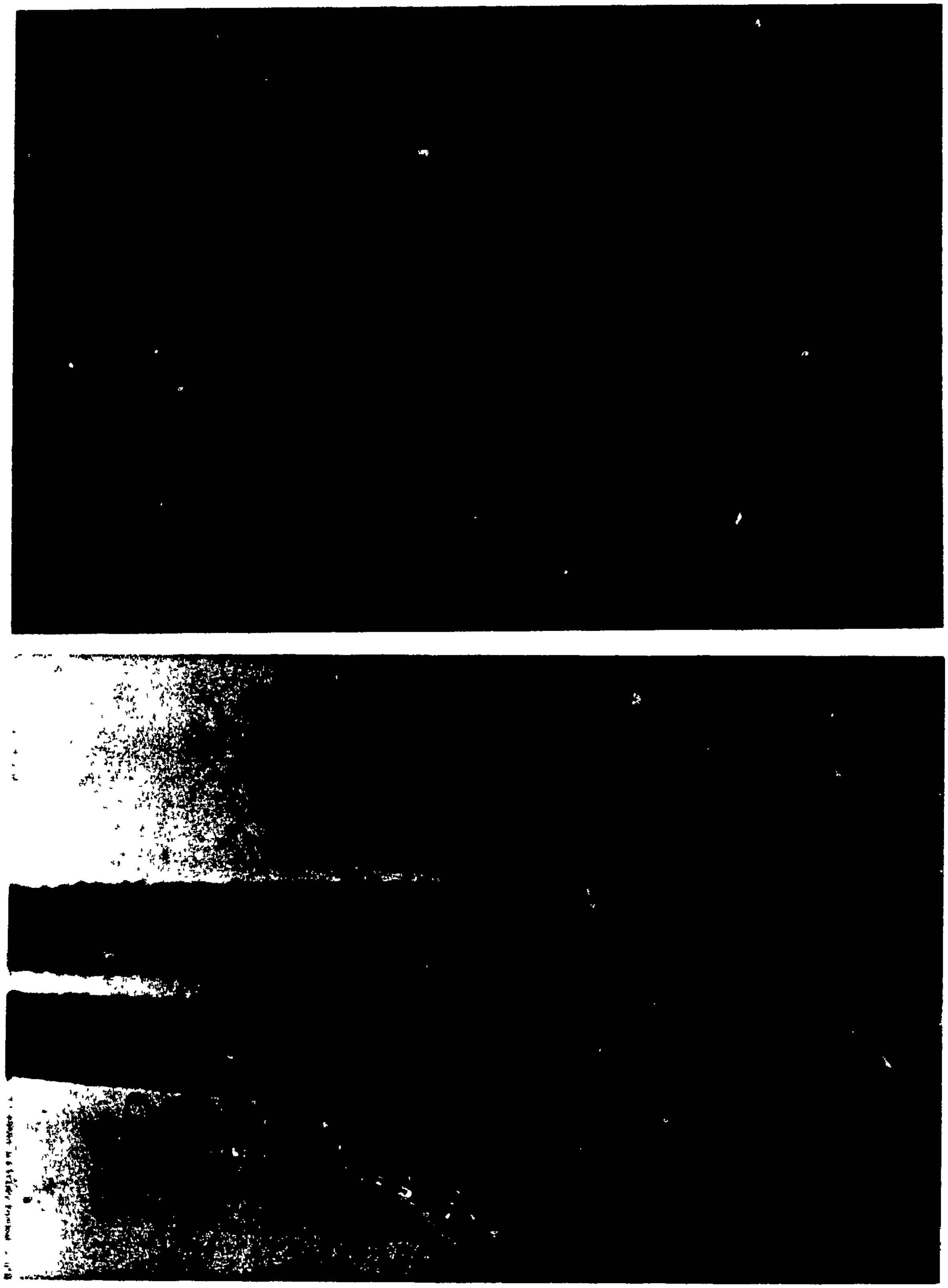

Figure IV-10 *Micrographs of sample 2 (good electrode alignment).*

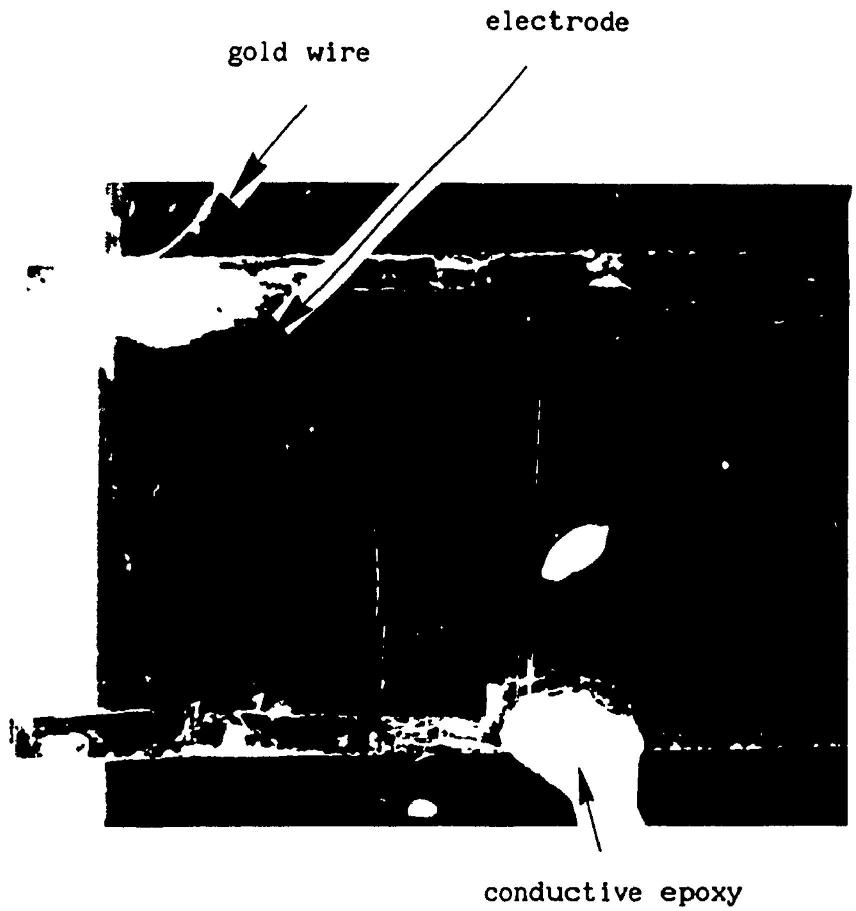

Figure IV-11 *Mounted device with connected elelectrodes.*

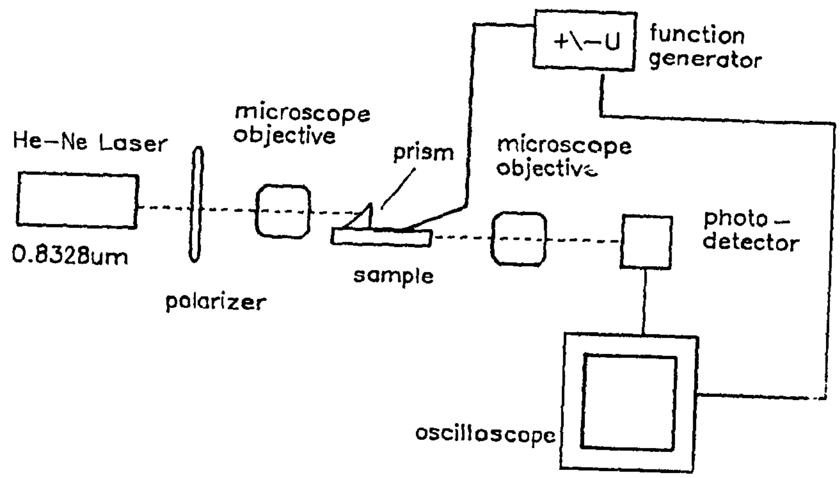

Figure IV-12 *(a) Experimental setup.*

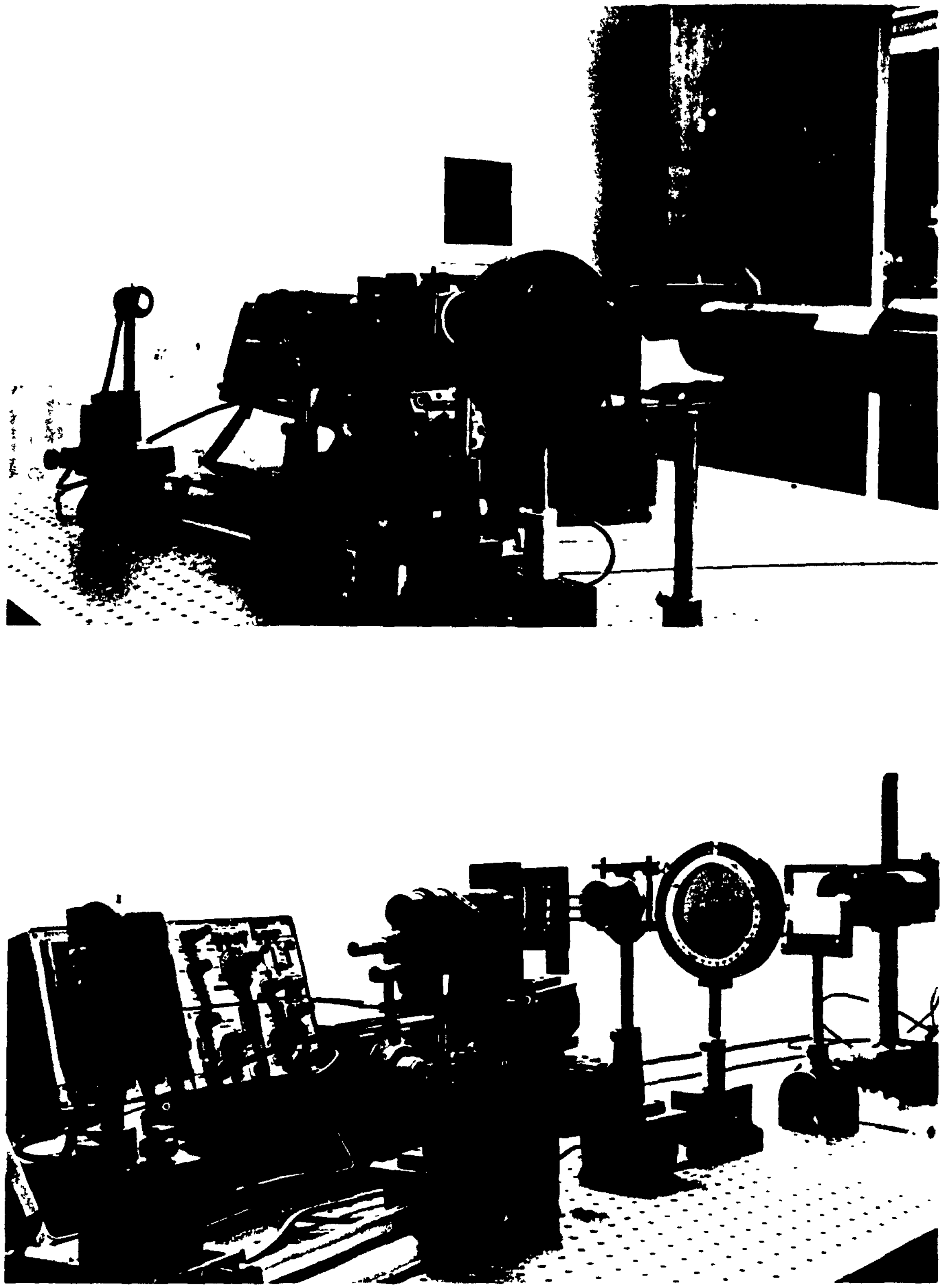

Figure IV-12 *(b) Experimental setup.*

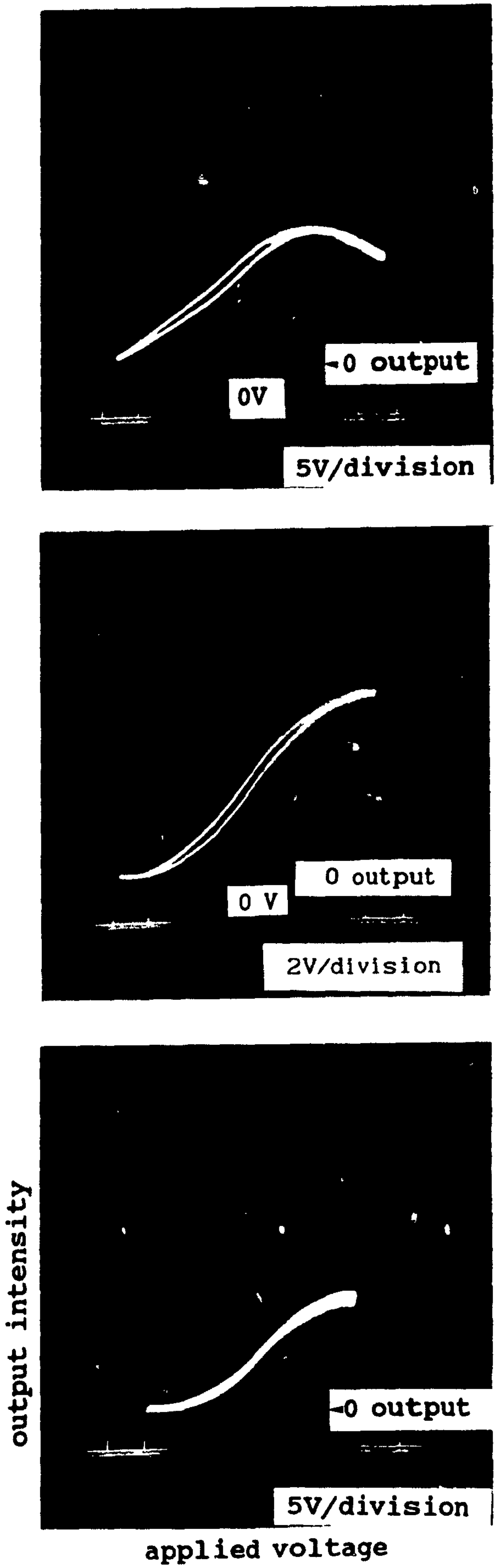

(a)

Sample 1

(b)

Sample 2

(c)

Sample 3

Figure IV-13 *Measured output intensity against the applied electrode voltage for (a) device 1, (b) device 2, and (c) device 3.*

(a)

(b)

(c)

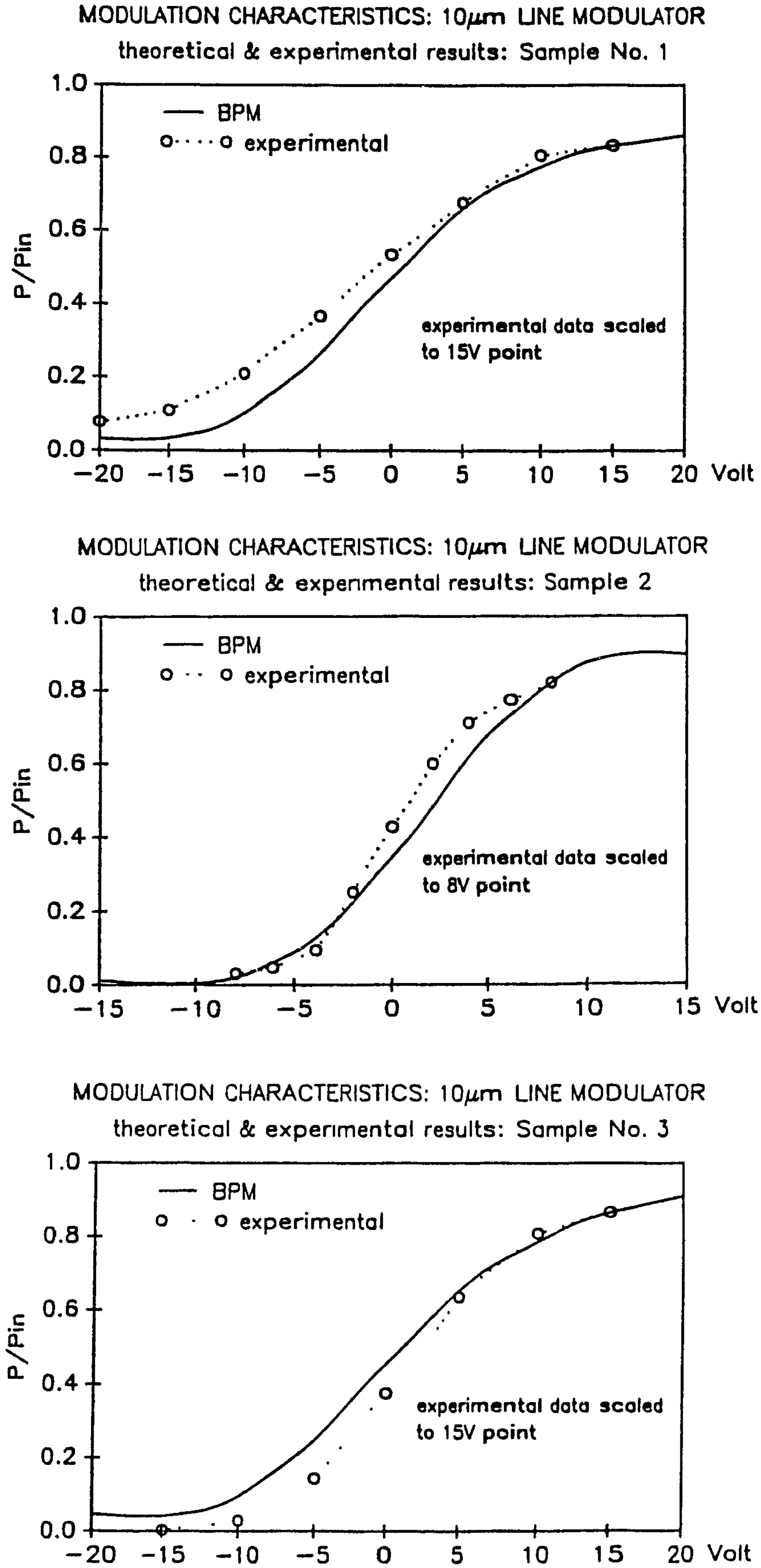

Figure IV-14 *Comparison of the theoretical modulation characteristics with experimental ones for (a) sample 1, and (b) sample 2, (c) sample 3.*

CHAPTER V. DESIGN OPTIMIZATION OF A $Ti:LiNbO_3$ 3-BRANCH OPTICAL SWITCH

V-1. Introduction

The use of 3-branch junctions for optical power division was investigated earlier in Chapter III. The realization of an optical multi-mode 3-branch switch by electro-optically changing the index distribution in a 3-branch power divider was also proposed and investigated in [1] for light with a 0.6328μm wavelength. This switch, shown in Figure V-1a, was fabricated in Ti-indiffused z-cut $LiNbO_3$ from a symmetric 3-branch junction. The optical switching behavior of the device was controlled solely by the electro-optic effect which led to the fabricated device exhibiting a strong bias to switch into the central branch, making the switch somewhat impractical. It was consequently suggested [1] to redesign the device so that its power division characteristics, with zero voltage applied to the electrodes, are altered to favour transmission into the side branches in order to overcome the switching bias. This proposal will be investigated in the following for a switch designed for single-mode operation at 1.32μm.

V-2. Principle of operation

The device configuration of the 3-branch optical switch is shown in Figure V-1b. The device consists of an input guide and 3 output guides of width w. These are connected by a shallow input taper. The optical power distribution in the neutral state (0V applied) is controlled by depositing a dielectric cladding on the outer branch areas, as shown in

Figure V-2a and investigated for ion-exchanged waveguides in glass in Chapter III, and/or by introducing a width asymmetry between the outer and central branches. In the latter case, the width w_2 of the side branches is reduced back to the original guide width w by means of an output taper, as indicated in Figure V-2b. This creates an optical power divider with a specified division ratio.

The optical switch is then realized by depositing a 3-electrode structure onto the taper and branching regions of the device. The effective index in an individual branch can thus be increased electro-optically by applying an appropriate voltage to the respective electrode with the other ones grounded. This forces more optical power through the selected branch and results in the switching behavior of the device.

V-3. Theoretical model and analysis

A theoretical analysis of the 3-branch switch requires the calculation of the optical power transmitted from the input guide into each of the three branches as a function of the applied electrode voltage. The theoretical model used previously [1] was, as mentioned earlier, based on a field matching technique which ignores radiation modes, and the model did not properly account for the attenuating effect of the buffer layer on the electric field in the crystal.

The new BPM design approach will now be used to redesign the 3-branch switch in view of the suggested improvements. The theoretical analysis is again based on a two-dimensional effective index model of the device. The diffusion profile is assumed to follow a Gaussian distribution in the depth coordinate ($LiNbO_3$ c-axis) and is, below the electrodes, perturbed by the electro-optic effect which is calculated as outlined in Section II-3. The increase in the effective index due to the cladding is then calculated from equation (III.1) and added to the effective index values of the appropriate grid points.

One difficulty in calculating the electro-optic effect arises, however, from the use of both a low refractive index buffer layer and a high index dielectric cladding in the outer branch regions. The dielectric cladding introduces on one hand an asymmetry in the electrode plane, as indicated in Figure V-3a, and on the other hand, the high dielectric permitivity of the cladding material (100 for TiO_2 [2]) results in an additional attentuation of the electric field strength in the cladded regions.

The electrode configuration shown in Figure V-3a can not be solved in the same manner as that for the buffer layer problem described in Section II-3 due to the asymmetry in the electrode plane. The following approximations were therefore made in calculating the electro-optic effect. In regions not covered by a dielectric cladding, the effective index is calculated as before including the attenuating influence of the SiO_2 buffer layer and ignoring any asymmetry in the electrode plane. For grid points in the cladded regions, the SiO_2 buffer layer is ignored and the electro-optic index change is calculated for a waveguide covered by a "buffer layer" made of the cladding material (TiO_2). The same equations apply as for treating the SiO_2 buffer layer problem except that the dielectric permitivity ε_r of the cladding material is used in the calculations. Figure V-3b illustrates this approach. The change in the effective index induced electro-optically is shown in Figure 4 for both side and central switching. After the effective index values for all grid points have been calculated, the increase in the effective index due to the dielectric cladding, calculated from equation (III.1), is added to those grid point values in the cladded regions.

V-4. Design Optimization

The design optimization of the 3-branch switch will be discussed in three steps. First, the use of a dielectric cladding to change the initial power division ratio for a symmetric switch design will be considered. Next, the use of both a dielectric cladding and an asymmetric waveguide design will be investigated and finally, the optimal electrode design will be determined for the waveguide/branch design chosen from steps one and two of the optimization. As pointed out earlier in Chapter IV, the optimization is based on an investigation of the influence of various design and fabrication parameters on the device performance from which a favourable design is deduced in an iterative manner.

The desired device characteriztics, in order of importance, are: 1) good switching behavior, i.e. high power extinction ratios between the branches for both side and central switching; 2) a small switching voltage, preferably symmetric for side and central switching with respect to the neutral state; 3) a small device insertion loss and; 4) compact device dimensions. Again, the feasibility of the design is limited by the fabrication tolerances, in particular the 4μm resolution limit of our mask-aligner.

The switch design will be based on an input/output guide width w of 8μm for single mode operation at a wavelength of 1.32μm. This allows some freedom in designing the electrodes which are most strongly limited by the resolution of our mask aligner. A SiO_2 buffer layer of 0.1μm thickness is assumed in all calculations. A shallow input taper of 3mm length was chosen to avoid mode conversion problems in that region. This choice was confirmed by later BPM simulations which do not indicate any mode conversion in the taper region. Longer taper regions have no particular effect on the switching characteriztics of the device. The diffusion parameters were chosen to provide reasonable fiber-waveguide coupling. For fiber core sizes used in light-wave communication applications at 1.32μm, a deep diffusion into the $LiNbO_3$ is required to provide efficient fiber-waveguide coupling by maximizing the overlap between the diffused guide mode and the large fiber mode [3]. On the other hand, a well confined optical mode generally reduces the drive voltage of electro-optic devices [3] which makes a large refractive index change desirable. A deep, well confined mode also reduces the propagation loss due to surface scattering and metallic loading [4]. This, however, results in a mode size miss-match with the fiber mode. Consequently, a tradeoff between efficient fiber-waveguide coupling and drive voltage has to be made.

A surface index change Δn_s of 0.007 and a diffusion depth of 3.0μm

were chosen to comply with the above considerations, and to also allow limited use of the diffusion characterization data at λ=0.6328μm provided in [5]. A recent study of wavelength dispersion on Ti:$LiNbO_3$ characterization data [6] indicates that the diffusion depth is independent of both the initial Ti metal strip thickness and the wavelength λ, whereas the surface refractive index change is reduced somewhat for longer wavelengths, compared to its value at λ= 0.6328μm.

The value of 0.007 was determined by first calculating the maximum surface index change Δn_s permissible for a 8μm wide diffused waveguide to support only one lateral mode at λ=1.32μm. This can be determined by solving for the effective index of the channel guide n_{eff} just below the cut-off point of the second order mode (m=1) in

$$m = \mathrm{INT}\left\{ 2\,\frac{w}{\lambda}\sqrt{n_{eff}^2 - n_b} \right\}, \qquad m=0,1,2,\ldots, \qquad \text{(V.1)}$$

with n_b, the substrate index, equal to 2.15 [2] at λ=1.32μm and w equal to the width of the channel waveguide. Equation (V.1) is the equivalent formulation for diffused waveguides of equation (IV.1). The largest permissible surface index change Δn_s to obtain a single-mode waveguide can then be calculated from equation (II.6) in an iterative manner with

$$n(x) = n_b + \Delta n_s \exp\,(-x^2/D^2), \qquad \text{(V.2)}$$

assuming a Gaussian diffusion profile.

For the parameters given above, the surface index Δn_s has to be smaller than 0.009 to yield a single-mode waveguide. Since the diffusion depth D is invariant with respect to the wavelength λ, the data given in

[6] can be used to crudely estimate the corresponding surface index change at $\lambda=0.6328\mu m$. Δn_s at $\lambda=1.32\mu m$ is approximately 25% to 30% [6] smaller than the corresponding index change at $\lambda=0.6328\mu m$. The fabrication parameters used in the characterization [5] to yield a waveguide with $D=3.0\mu m$ and $\Delta n_s=0.01$ will consequently provide the desired waveguide parameters ($\Delta n_s=0.007$, $D=3.0\mu m$) at $\lambda=1.32\mu m$.

The influence of using a dielectric cladding of TiO_2 to change the initial power division ratio of a power divider/switch with a symmetric waveguide design on the switching characteristics is shown in Figures V-5a to V-5d for a branching angle α of 0.01 RAD. Larger branch angles significantly impair the power division behavior of the device. The cladding thicknesses were chosen to reflect the following power division ratios: 1:1:1 [2450Å], 1:2:1 [2150Å], 1:3:1 [1850Å], and 1:7:1 [no cladding]. The required cladding thickness to achieve such particular power division ratios were determined from Figure V-6. An examination of Figures V-5a to V-5d allows the following conclusions to be made:

1) increasing the cladding, and thus the power in the side branches in the zero voltage state, improves the side switching and overcomes the switching bias mentioned earlier.
2) Increasing the cladding, however, also makes central switching more difficult. A switch design based on an equal power divider is therefore not feasible.
3) Even power division ratios such as [1:3:1], which produce a reasonable switching behavior, require a relatively large cladding thickness (1500-2000Å). This is problematic because it a) causes a

large attenuation of the electric field due to the high dielectric constant of the cladding material, and b) creates a large asymmetry in the electrode plane.

Next, the use of both a dielectric cladding and a waveguide asymmetry will be investigated. To describe the asymmetry in the design, we introduce a parameter *asym* defined as the ratio of the outer waveguide width w_2 to the central guide width w. Thus, a symmetric design will produce a value of 1 and an outer guide width of twice the central guide width results in a value of 2. The power division behavior of the device with an increasing cladding thickness for various asymmetry values are shown in Figures V-7a and V-7b. An increase in asymmetry clearly reduces the cladding thickness required to achieve a specific power division ratio. This is particularly obvious for low division ratios such as [1:3:1] due to the smoother behavior of the power in the central branch with increasing cladding thickness. A thinner cladding would reduce both the asymmetry in the electrode plane and the additional attenuation of the electric field due to the cladding. The introduction of an asymmetry into the branch design, however, also increases the insertion loss of the power divider. Table V-1 summarizes the cladding thicknesses required for various division ratios for asym values of 1, 1.5, and 2.

Table V-1: Cladding thicknesses

	[1:1:1]	[1:2:1]	[1:3:1]	no cladding
Asym = 1	2450Å	2150Å	1850Å	[1:7:1]
Asym = 1.5	2200Å	1650Å	1000Å	[1:(4.2):1]
Asym = 2	1850Å	1100Å	200Å	[1:(3.3):1]

The switching behavior for device designs with different cladding thicknesses and asymmetry values are given in the following Figures:

Asym = 1.5 ($w=8\mu m$, $w_2=12\mu m$)

Cladding	0Å	Figure V-8a
	1000Å [1:3:1]	V-8b
	1650Å [1:2:1]	V-8c
	2200Å [1:1:1]	V-8d

Asym = 2 ($w=8\mu m$, $w_2=16\mu m$)

Cladding	0Å	Figure V-9a
	200Å [1:3:1]	V-9b
	1100Å [1:2:1]	V-9c
	1850Å [1:1:1]	V-9d.

The examination of these Figures allows the following conclusions to be made:

1) The switching behavior for a specific division ratio is significantly improved with increasing asymmetry (compare for example Figures V-8b and V-9b [1:3:1] or V-8c and V-9c [1:2:1].

2) Increasing the asymmetry, however, results in a somewhat larger device insertion loss for side switching.

3) The best switching behavior, both for side and central switching, occurs for an initial power division ratio of [1:3:1] (Figures V-8b, 9b), the same ratio as found for the symmetric design (Figure V-5c).

Consequently, an asymmetric switch design with a power division ratio of around [1:3:1] will be chosen. Since the cladding thickness to achieve this particular division condition for an asymmetry ratio of 2 is only 200Å, the cladding can be removed completely so that the initial power division ratio is only determined by the asymmetry and the diffusion conditions. The switching characteristics of the device are not significantly altered as can be verified by comparing Figures V-9a and V-9b. The removal of the dielectric cladding has the advantages of making the device fabrication simpler and eliminating the asymmetry in the electrode plane. The approximations made in Section V-3 for calculating the electro-optic effect in the presence of a dielectric cladding are not required which improves the accuracy of the theoretical model. The beam evolution in such an asymmetric power divider / switch for the zero voltage state is shown in Figure V-10. No excitation of higher order modes in the taper regions is observable which validates the initial choice of taper lengths.

Finally, the optimal electrode configuration for our power divider design will be considered. Recently, the optimization of the electrode design of a single-mode crossing channel electro-optic switch in $LiNbO_3$ operating at 1.32μm was used to reduce its switching voltage from an initial 50V [7] to one as low as 20V [8]. The design parameters available for our 3-electrode configuration are the center and side electrode widths and the inter electrode gap. Reducing the latter parameter generally results in a lower switching voltage [3,8]. The electrode gap is therefore chosen to reflect the fabrication limit of our facilities (4μm).

Figures V-11a to V-11c show the switching characteristics of the device for center electrode widths of 4, 6 and 7μm. The corresponding extinction ratios for each case are summarized in Table V-2. The desired switching behavior (see page 99) are best matched for an electrode width of 7μm. The choice of the side electrode width for a specific center electrode is not expected to influence the switching behavior for central switching since the side electrodes are grounded and have no influence on the electric field. We therefore choose to optimize the side electrode width for side switching based on the choice of the center width and gap. Figures V-12a to V-12c show the respective switching behavior for side electrode widths of 4 to 18μm. Their extinction ratios are summarized in Table V-3. The best side switching is achieved for a side electrode width of 9μm.

The optimized switch design has a theoretical drive voltage of ±30V with a power extinction ratios of 18.5dB (P_1/P_2) and 10.3dB (P_1/P_3) for side switching, and 18.5dB for central switching. Its switching characteristics are shown in Figure V-12c. The configuration of the optimized switch is shown in Figure V-13a. The optical field evolution for both side and central switching with 30V applied to the appropriate electrodes are given as Figures V-13b and V-13c, respectively. No mode conversion can be observed in the taper regions for either switching conditions.

Table V-2: Electrode optimization - center electrode width

asym = 2 cladding = 0 [1:3:1] resolution limit = 4μm

electrode width center	side	gap	voltage	switching behavior central $P_{1,3}/P_2$	side P_1/P_2	P_1/P_3	
μm	μm	μm	V	dB	dB	dB	
4	9	4	20	10.6	5.5	27.4	
			30	13.8	6.9	15.6	
			40		7.2	12.5	
6	9	4	20	12.0	7.3	15.0	
			30	17.6	13.2	12.9	
			40	24.9	6.6	9.4	
7	**9**	**4**	**20**	**12.3**	**7.2**	**11.9**	*
			30	**18.5**	**18.5**	**10.3**	
			40	**22.7**	**8.6**	**8.4**	

*=best switching behavior

Table V-3: Electrode optimization - side electrode width

asym = 2 cladding = 0 [1:3:1] resolution limit = 4μm

electrode width center	side	gap	voltage	switching behavior central $P_{1,3}/P_2$	side P_1/P_2	P_1/P_3	
μm	μm	μm	V	dB	dB	dB	
7	4	4	20	12.3	6.9	12.3	
			30	18.5	15.7	10.3	
			40	22.7	7.7	8.0	
7	6	4	20	12.3	7.1	12.0	
			30	18.5	16.9	10.2	
			40	22.7	7.9	8.2	
7	**9**	**4**	**20**	**12.3**	**7.4**	**11.9**	*
			30	**18.5**	**18.5**	**10.3**	
			40	**22.7**	**8.6**	**8.4**	
7	18	4	20	12.3	7.1	13.3	
			30	18.5	18.1	9.6	
			40	22.7	9.6	7.8	

Finally, the influence of varying the diffusion parameters, specifically the surface index change Δn_s, on the device performance will be determined. Since only limited characterization data for the Ti diffusion process is available, it is useful to determine how critically the device performance is linked to Δn_s. Figures V-13d and V-13e show the switching behavior of the optimized device design for a Δn_s of 0.006 and 0.008. The value of Δn_s is limited to values below 0.009 for single mode operation at 1.32μm and a diffusion depth of 3.0μm. The device performance for different Δn_s is summarized in Table V-4. As expected, a slightly smaller or larger surface index change increases or decreases the switching voltage, respectively. However, the switching behavior of the device itself is not significantly altered.

Table V-4: Device performance for different Δn_s

Gaussion diffusion profile, D=3.0μm		switching behavior		
		central	side	
surface index change	V	$P_{1,3}/P_2$ dB	P_1/P_2 dB	P_1/P_3 dB
0.006	20	17.7	6.4	10.2
	30	19.6	18.2	9.2
	40	23.2	7.6	8.3
0.007	20	12.3	7.2	11.9
	30	18.5	18.5	10.3
	40	22.7	8.6	8.4
0.008	20	13.3	8.5	12.9
	30	16.5	19.4	11.8
	40	24.9	6.6	9.4

V-5. Fabrication of a 3-branch optical switch

A 3-branch optical switch with a input/output guide width of 8μm was fabricated from the optimized design determined in Section V-4 (Figure 13a) on a z-cut y-propagating $LiNbO_3$ plate. First, using photo-lithography and a lift-off technique, a waveguide pattern of evaporated titanium was formed on the cleaned $LiNbO_3$ substrate. The metal was consequently diffused into the crystal at 975°C for 6 hours in a flowing argon atmosphere and a further hour in flowing oxygen to prevent out-diffusion. This creates a channel waveguide at λ=0.6328μm with an estimated surface index change of 0.11 [5] and a diffusion depth of 3.0μm. For light at 1.32μm, the surface index change in n_e was estimated to be about 25% lower than that at 0.6328μm [6], thus Δn=0.0085 at 1.32μm. At this point, the ends of the crystals were optically polished to permit endfire coupling.

Next, a thin SiO_2 buffer layer was RF sputtered onto the sample, followed by annealing at 500°C in flowing oxygen for 2 hours to reoxidize both the SiO_2 and the substrate, and to recover from the damage to the crystal surface due to the sputtering process. Finally, the electrodes were formed by evaporating an aluminum film on top of the buffer layer, and, using photo-lithography, removing the redundant metal with an appropriate chemical solution (H_3PO_4:HNO_3:CH_3COOH:H_2O = 16:1:2:1). Table V-5 summarizes the achieved fabrication parameters of the device. A micrograph of the titanium waveguide pattern before the diffusion step in the vicinity of the branching point is shown is shown in Figure V-14.

The fabricated device was then mounted on a holder for proper connection of the electrodes. The electrodes were connected using 50μm gold wire and a silver conductive epoxy. Figure V-15 shows the mounted sample with connected electrodes.

Table V-5: Fabrication parameters

Ti thickness	131Å
Surface index change at 0.6328μm	0.011
Estimated surface index change at 1.32μm	0.0085
Diffusion depth	3.0μm
Buffer layer thickness	0.12μm
Number of lateral modes supported at 0.6328μm	4
Number of lateral modes supported at 1.32μm	1
Guide width w	8μm
Asymmetry	2
Taper	3mm
Output taper	2mm
Branch angle α	0.01 RAD
Center electrode width	7μm
Side electrode width	9μm
Electrode gap	4μm

V-6. Measurement of a 3-branch active switch

The experimental setup used to measure the switching characteristics of the fabricated devices is shown in Figures V-16a and 16b. Laser light was TM-polarized and endfire coupled into the input guide of the 3-branch switch. At the output end, the light leaving the respective guides was focused through a microscope objective onto a camera/monitor system or an appropriate photo-detector connected to an oscilloscope. The voltage applied to the electrodes from the function generator, while measuring the switching characteristics, was a slowly varying ramp. The device performance was measured for wavelengths of 0.6328μm and 1.32μm.

Figures V-17a through 17c show the near field light spots of the switch, operating at 0.6328μm, and the corresponding light intensity scans for side and central switching, and for the zero voltage state. At this wavelength, the passive device acts essentially as an equal power divider. Power extinction ratios of >25dB (P_1/P_2) and 15.6dB (P_1/P_3) were obtained at 12V for the side switching condition. A poorer performance of 13.6dB ($P_2/P_{1,3}$) at 20V, compared to a theoretical value of 16.6dB at 20V, was measured for central switching. These results are consistent with the findings of the BPM analysis in Section V-4 which predicted a much improved side switching performance at the expense of poorer central switching for a switch design based on an equal power divider. Figures V-18a and 18b show the switching characteristics for both voltage states together with the theoretical results. Reasonably good qualitative and quantitative agreement between the two can be observed. The experimental switching voltage determined from Figure 18a of 9V (intensity peak) corresponds very well to the theoretical value of 10V for the side switching condition. The poorer extinction ratio of 13.6dB for central switching and the high drive voltage of 20V, compared to a theoretical value of 16.5dB at 20V, could be due to increased mode conversion and mode coupling in the branching region since, at 0.6328μm, the device is strongly multi-moded. The optical field calculation at 0.6328μm for both switching states are shown in Figures V-19a and 19b. Table V-6 summarizes the power distribution in the first 3 modes in each branch for the different switching conditions. For the central switching condition, 98% of the power in the central branch propagates in the first order mode. For side switching, however, 31% of the output power in the selected branch propagates in higher order modes.

Table V-6: Modal power in individual branches at 0.6328μm

[% of total Power in indiv. branch]		P_1	P_2	P_3
Neutral state:	P_{branch}	0.27	0.37	0.27
	m=0	57%	97%	62%
	m=1	41%	1%	33%
	m=2	2%	2%	5%
Side switching:	P_{branch}	0.73	0.04	0.17
	m=0	69%	70%	60%
	m=1	29%	29%	34%
	m=2	2%	1%	6%
Central switching:	P_{branch}	0.02	0.92	0.02
	m=0	18%	98%	35%
	m=1	76%	1%	53%
	m=2	6%	1%	12

Figures V-20a through V-20d show the light intensity scans for side switching into arm 1 and arm 3, for central switching, and for the neutral state, for light at 1.32μm. Power extinction ratio of 15.9dB (P_1/P_2) and 20.1dB (P_1/P_3) were obtained at a voltage of 32V for side switching into arm 1 (left branch). These voltage values were determined from the peak value of light intensity in the selected branch, as displayed on the oscilloscope. A poorer performance of 5.8dB (P_3/P_2) and 14.0dB (P_3/P_1) for side switching into arm 3 (right branch) was obtained at 35V. This inferior result, compared to side switching into arm 1, could be due to a slight waveguide asymmetry, caused by small irregularities in the edges of the titanium waveguide pattern and the particular side electrode in the branching region of the device. These irregularities may cause the incomplete coupling of the optical power during side switching into the right arm. This problem, however, was not observed for side switching at 0.6328μm. Since the device is strongly multi-moded at that wavelength, additional mode conversion may be "compensating" for the waveguide irregularities.

Central switching at 1.32μm required a voltage of 35V to achieve a 16.1dB (P_2/P_1) extinction ratio. This result compares well with the theoretical value of 15.9dB at 35V. In the neutral state, the switch acts as a power divider with a division ratio of 1:2:1. This compares very favourably to the theoretical value of 1:1.9:1. The device performance results at both 0.6328μm and 1.32μm are summarized in Table V-7. Figure V-21 shows the theoretical switching characteristics of the fabricated device at λ=1.32μm. The experimental switching characteristics could regrettably not be measured due to alignment difficulties arising from the use of a 1.32μm laser diode with a multi-mode fiber pig-tail instead of an actual laser. Since light at 1.32μm is invisible, it is necessary to align a 0.6328μm (visible) laser beam with the output of the 1.32μm laser so that the two beams coincide. This can then be used as a reference when adjusting the photo-detector used to measure the characteristics. This is, however, not possible with the pig-tailed laser diode which makes a successful alignment of the photo-detector with the output guides of the switch nearly impossible.

The optical field calculations at 1.32μm for both switching states and the neutral voltage state are shown in Figures V-22a through 22c.

The device insertion loss measurements were unsuccessful since it proved impossible to couple any significant amount of light into a straight waveguide of 8μm width fabricated on the same substrate as the device. This could be due to a fault in the waveguide metal pattern (crack) or due to damage to the input or output region of the waveguide from end-fire polishing. The polishing procedure has not yet been developed in our laboratory to the level required to produce consistent results of a high quality. The straight waveguide was to be used as

Table V-7: Device performance

	theoretical [dB] [V]	*experimental* [dB] [V]	λ
Neutral state	1.4dB [1:1.3:1]	0.4dB [1.1:1.1:1]	
Central switching	16.6dB[1], 20V	13.6dB, 20V	0.63μm
Side switching	12.6dB[2], 6.3dB[3], 10V	>25db, 15.6dB, 12V	
Neutral state	2.8dB [1:1.9:1]	3.0dB [1:2:1]	
Central switching	15.9dB, 35V	16.1dB, 35V	1.32μm
Side switching	17.2dB, 14.1dB, 28V	15.9db, 20.1dB, 32V	

[1] $P_2/P_{1,3}$, [2] P_1/P_2, [3] P_1/P_3

a reference to compare the optical power in the selected arm of the switch with the power in the straight waveguide.

The theoretical results for the device indicate a relatively low device loss (not accounting for fiber/waveguide coupling loss and other non-device design related losses) of about 10% for operation at 1.32μm.

Higher loss values of close to 30% for side switching could be expected for operation at 0.6328μm.

V-7. Discussion and conclusion

A 3-branch optical power with its power division behavior modified to favour more optical power being coupled into the side branches was used as the design basis of an electro-optical 3-branch switch. The BPM design method was employed to optimize the device design and fabrication parameters. The theoretical performance predictions were then compared to those of a fabricated device.

Power extinction ratio of 15.9dB (P_1/P_2) and 20.1dB (P_1/P_3) were obtained experimentally at a voltage of 32V for side switching into arm 1 (left branch) for light at a wavelength of 1.32μm. A poorer performance of 5.8dB (P_3/P_2) and 14.0dB (P_3/P_1) for side switching into arm 3 (right branch) was achieved at 35V. This inferior result, compared to side switching into arm 1, could be due to small irregularities in the edges of the titanium waveguide pattern in the branching region of the device, causing incomplete coupling of the optical power during side switching into the right arm. Central switching at 1.32μm required a voltage of 35V to achieve a 16.1dB (P_2/P_1) extinction ratio. These experimental results correspond well to the theoretical predictions. The central switching bias of the previous device based on a symmetric power divider design [5] has been overcome with the new design.

The device performance was also measured for light at 0.6328μm. Power extinction ratios of >25dB (P_1/P_2) and 15.6dB (P_1/P_3) were obtained at 12V for the side switching condition. A poorer performance of 13.6dB ($P_2/P_{1,3}$) at 20V was measured for central switching. This result is consistent with the results of the BPM analysis in Section V-4 which predicted a much improved side switching performance at the expense of poorer central switching for a switch design based on a equal power divider. The performance of the new design at 0.6328μm constitutes a considerable improvement over that of the previous device (for a comparision, see Table V-8), particularly for the side switching condition.

Table V-8: Device performance comparison

expermimental results:	previous device [5] [dB] [V]	new device [dB] [V]
Neutral state	-	0.4dB [1.1:1.1:1]
Central switching	16.6dB^1, 20V	13.6dB, 20V
Side switching	12.6dB^2, 6.3dB^3, 10V	>25db, 15.6dB, 12V

^{1} $P_2/P_{1,3}$, ^{2} P_1/P_2, ^{3} P_1/P_3

It should be possible to improve the device performance further with better fabrication facilities. The relatively large resolution limit of the current mask-aligner makes an optimal design of the electrodes (by, for example, reducing the electrode gap to 2μm) and a reliable fabrication of branching structures with angles as small as 0.01 rad difficult.

The lack of sufficient characterization data for titanium indiffusion into $LiNbO_3$ at wavelengths between 1.1μm and 1.55μm introduces a further margin of error in the fabrication parameters. The surface index change of the waveguides had to be estimated relatively crudely by using available characterization data at 0.6328μm and information given in reference [6]. A detailed characterization of Ti diffusion is required for further design work at these wavelengths.

The problem of efficient fiber to waveguide coupling was treated only briefly in this Chapter. For actual fiber system oriented design work, the topics of efficient fiber coupling and of device insertion loss reduction would also have to be tackled in greater detail. Restrictions on the waveguide design (diffusion parameters, guide width etc.) to provide efficient coupling will pose further restraints on the achievable device design and performance. These considerations will have to be incorporated into the design procedure.

The successful optimization and experimental implementation of the 3-branch switch, and the good correspondence between the experimental and theoretical performance of the new device design, confirm the usefulness and accuracy of the new BPM design method as a CAD tool for design oriented studies in integrated optics. The results discussed in this chapter have been accepted for presentation at a forthcoming conference [9].

References:

1 Bélanger, M. and Yip, G.L., 'Theoretical and experimental investigation of an active 3-branch Ti:$LiNbO_3$ waveguide switch,' *Appl. Optics*, 28, 1, pp. 53-59, 1989.

2 Weast, R.C., *Handbook of Lasers*, CRC Press, Cleveland, 1971.

3 Alferness R.C., Ramaswamy, V.R., Korotky, S.K., Divino, M.D. and Buhl, L.L., 'Efficient single-mode fiber to titanium diffused $LiNbO_3$ waveguide coupling for λ=1.32μm,' *J. Quant. Electron.*, QE-18, 10, pp. 1087-1813, 1982.

4 Murphy, E.J., 'Fiber attachment for guided wave devices,' *J. Lightwave Techn.*, LT-6, 6, pp. 862-871, 1988.

5 Bélanger, M., *Theoretical and Experimental studies on active and passive 3-branch waveguides and their derivatives*, Ph.D. Thesis, Dept. of Elec. Eng., McGill University, Montréal, Canada, pp. 165-170, 1986.

6 Fouchet, S., Carenco, A., Daguet, C., Guglielmi, R., and Riviere, L., 'Wavelength dispersion of Ti induced refractive index change in $LiNbO_3$ as a function of diffusion parameters,' *J. Lightwave Techn.*, Lt-5, 5, pp. 700-708, 1987.

7 Neyer, A., Mevenkamp, W., Thylén, L., and Lagerström, B., 'A BPM analysis of active and passive waveguide crossings,' J. Lightwave *Techn.*, LT-3, pp. 635-642, 1985.

8 Goel, K., Wooten, E.. and Chang, W.S.C., 'Design considerations for low switching voltage crossing channel switches,' *J. Lightwave Techn.*, LT-6, 6, pp. 881-885, 1988.

9 Sekerka-Bajbus, M.A. and Yip, G.L., 'Design optimization of a 3-branch optical switch by the Beam Propagation Method,' to be presented at *S.P.I.E. Integrated Optical Circuit Engineering VI*, Boston, Mass., 6 Sept. 1989.

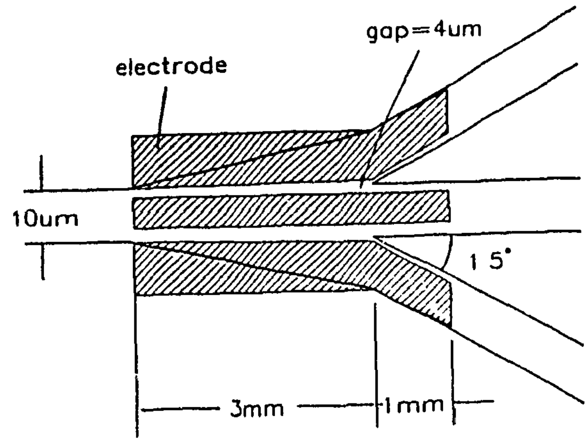

Figure V-1 *(a) Device configuration used in [1].*

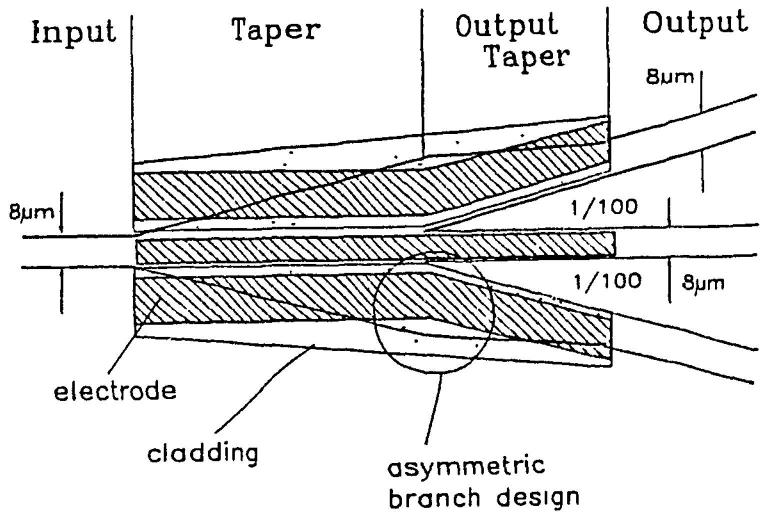

Figure V-1 *(b) Device configuration with power division ratio changed to favour transmission into side branches.*

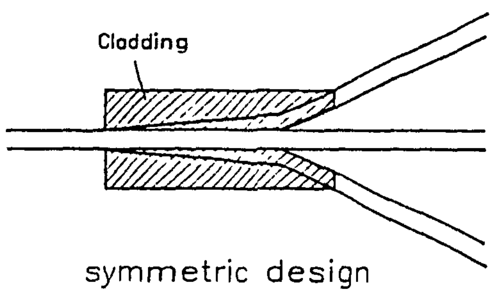

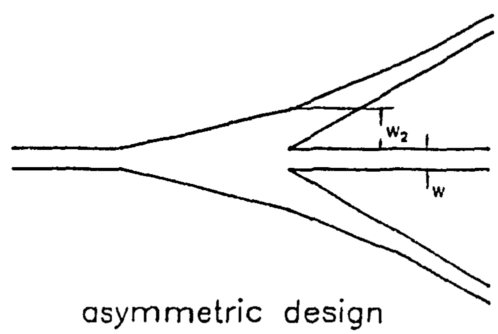

Figure V-2 *(a) Symmetric power divider with a dielectric cladding.*

Figure V-2 *(b) Asymmetric power divider design.*

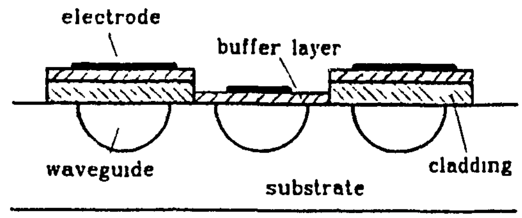

Figure V-3 *(a) Electrode configuration in the presence of a dielectric cladding and a buffer layer.*

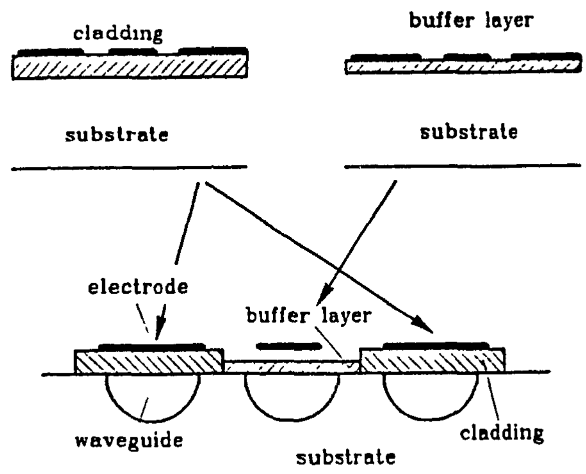

Figure V-3 *(b) Illustration of the approach used to approximate the electrode configuration shown in* V-3a.

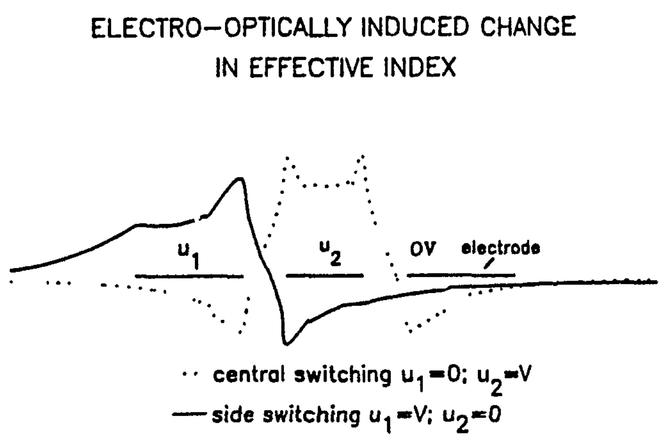

Figure V-4 *Electro-optically induced change in the effective index for both side and central switching.*

(a)

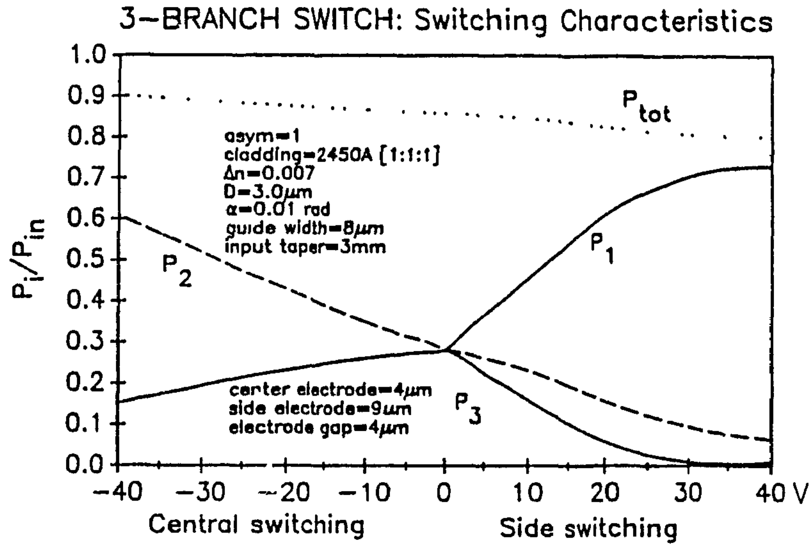

λ=1.32μm

(b)

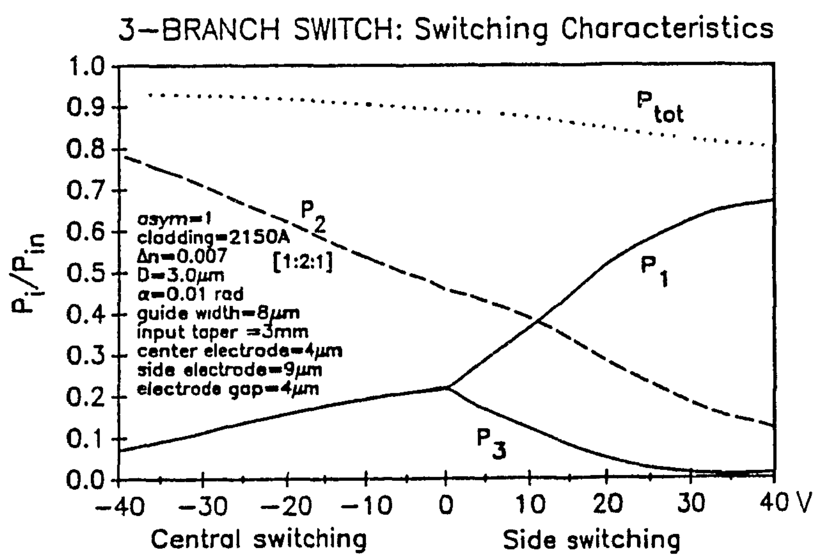

Figure V-5 *Switching characteristics for symmetric switch design with power division ratios of (a) [1:1:1] and (b) [1:2:1].*

(c)

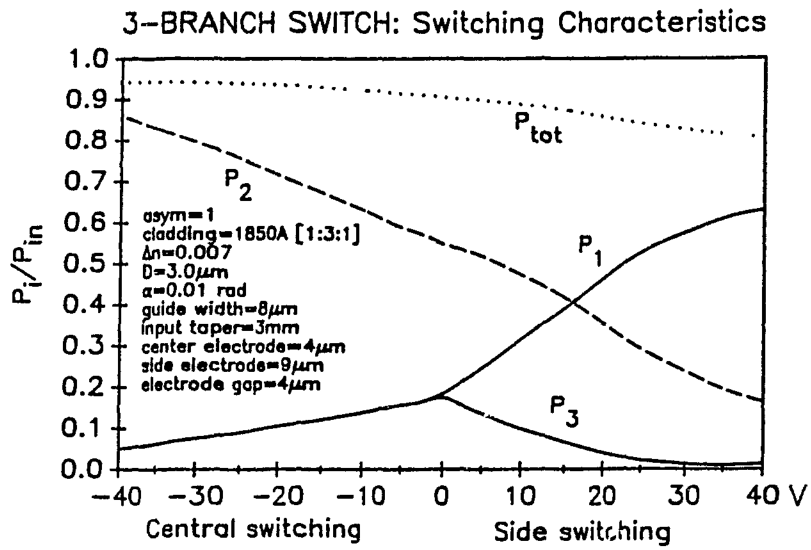

λ=1.32μm

(d)

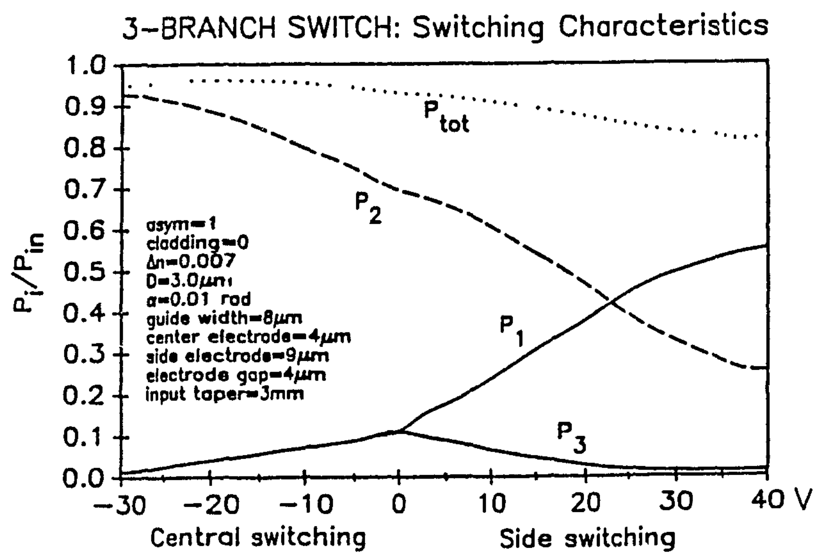

Figure V-5 *Switching characteristics for symmetric switch design with power division ratios of (c)* [1:3:1], *and (d)* [1:7:1].

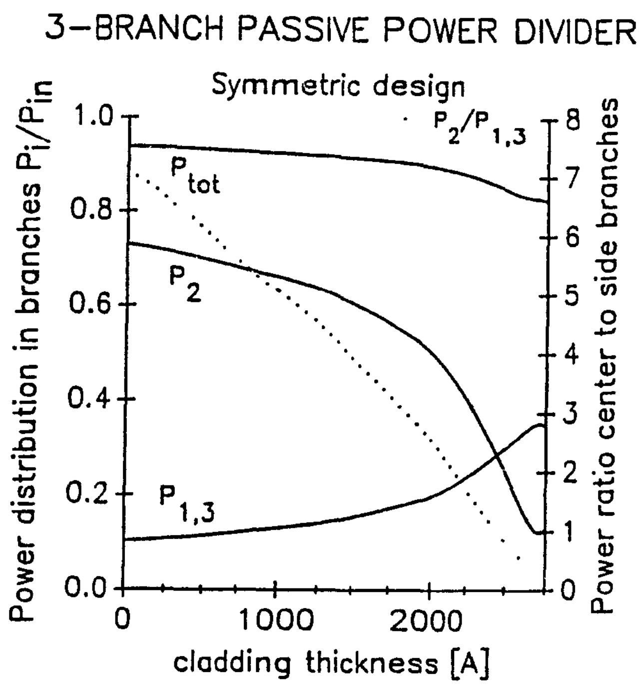

Figure V-6
Power division ratio for a symmetric power divider as a function of the cladding thickness.

λ=1.32μm

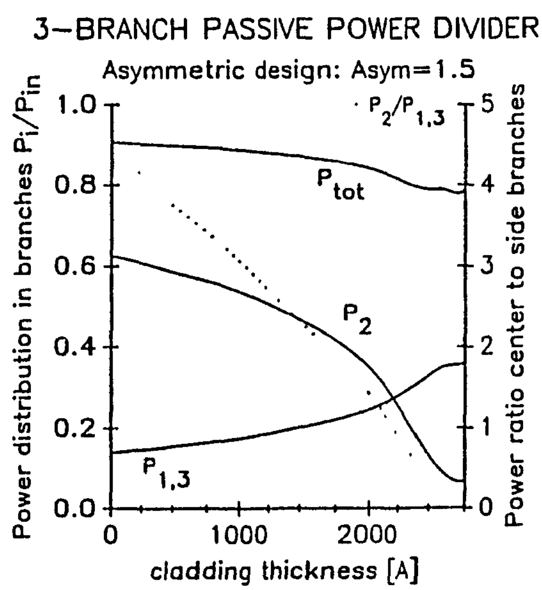

(a)

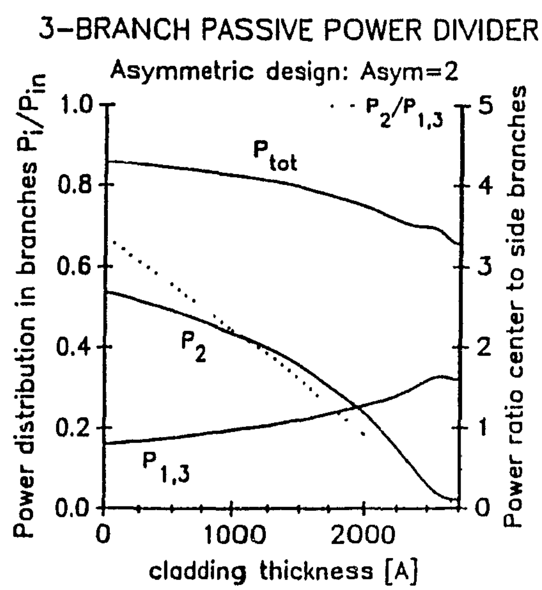

(b)

Figure V-7 *(a) Power division ratio for an asymmetric power divider as a function of cladding thickness: (a) (asym=1.5) and (b) (asym=2) .*

(a)

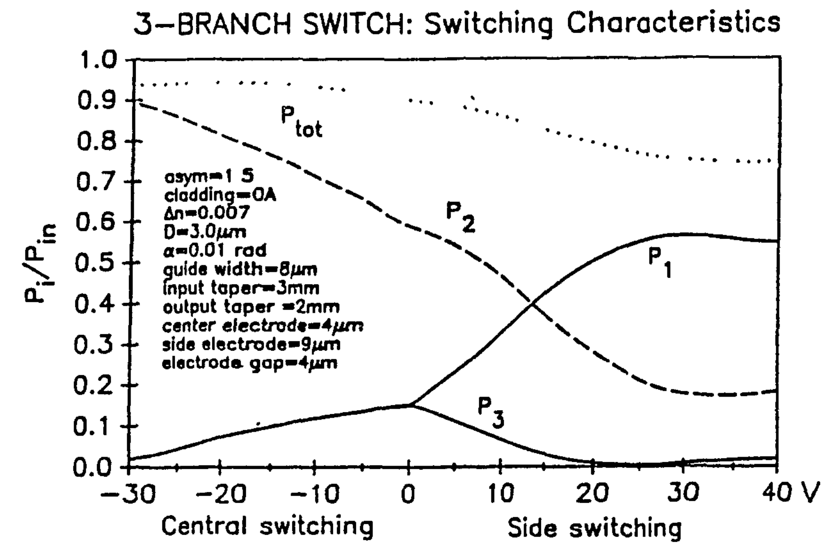

λ=1.32μm

(b)

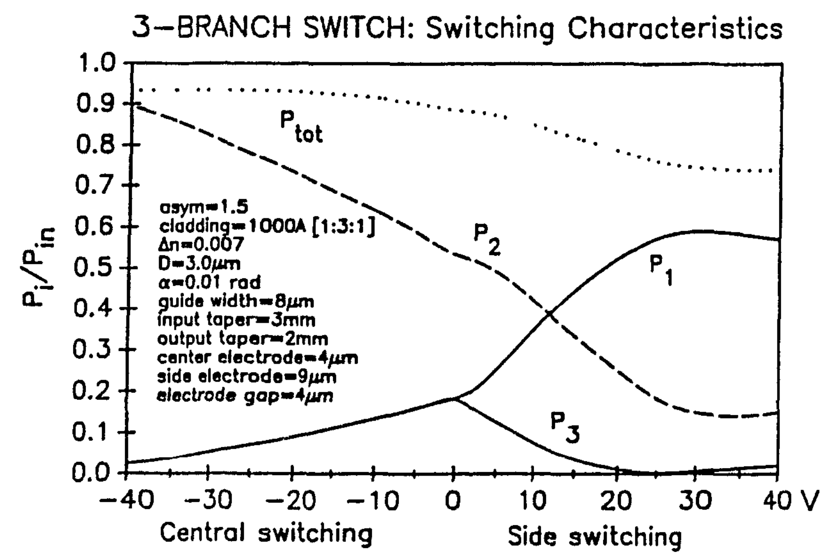

Figure V-8 *Switching characteristics for an asymmetric switch (asym=1.5) design with (a) no cladding, (b) with a power division ratio of [1:3:1].*

(c)

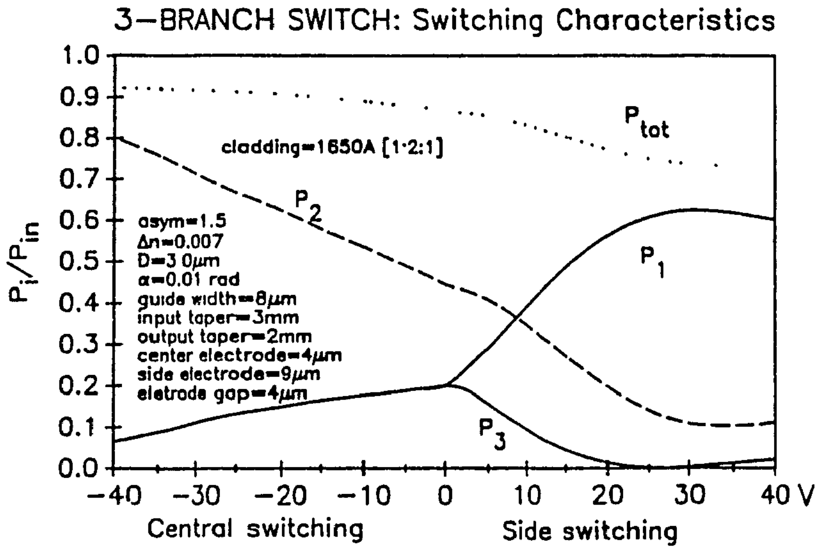

λ=1.32μm

(d)

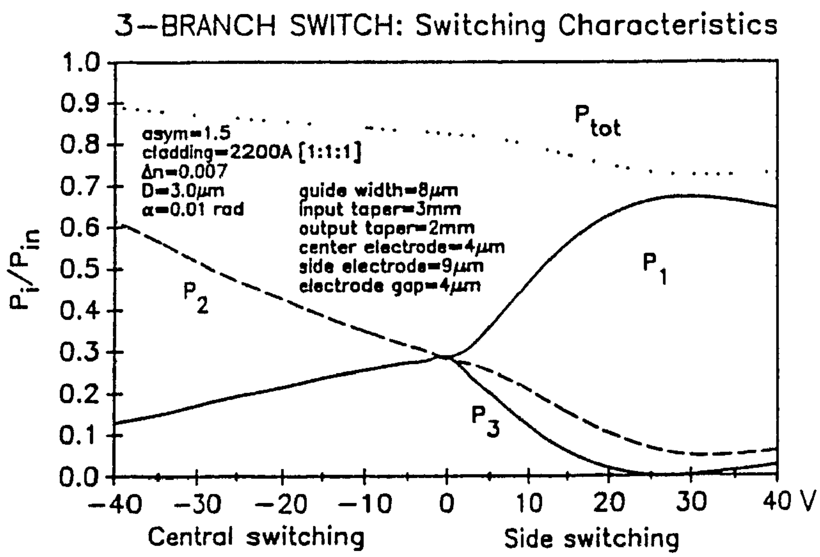

Figure V-8 *Switching characteristics for an asymmetric switch (asym=*1.5*) design with a power division ratio of (c)* [1:2:1] *and (d)* [1:1:1]

(a)

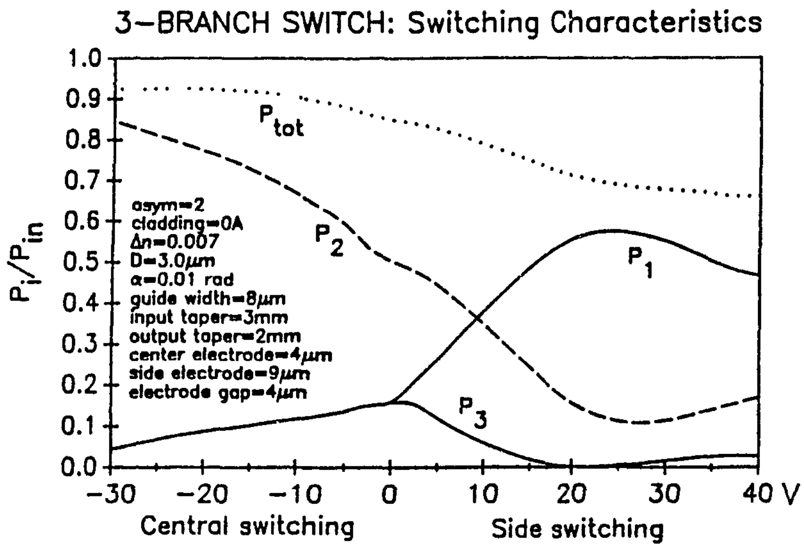

λ=1.32μm

(b)

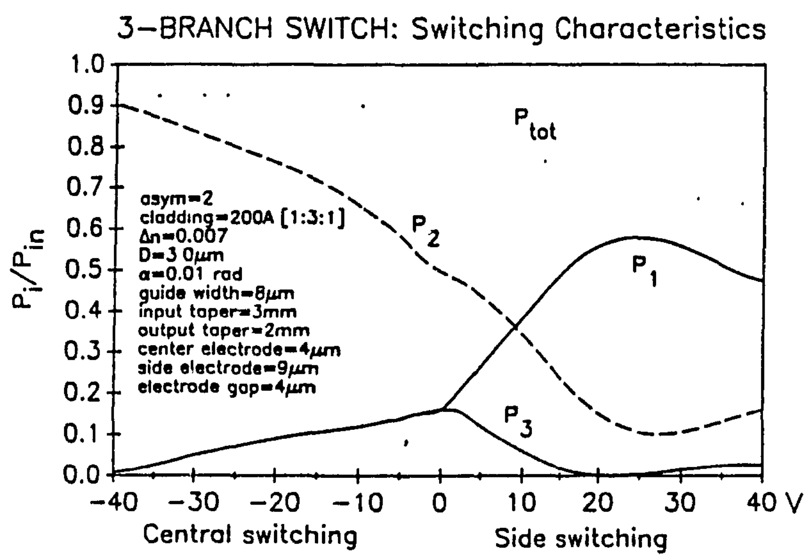

Figure V-9 *Switching characteristics for an asymmetric switch (asym=2) design with (a) no cladding, (b) with a power division ratio of [1:3:1].*

(c)

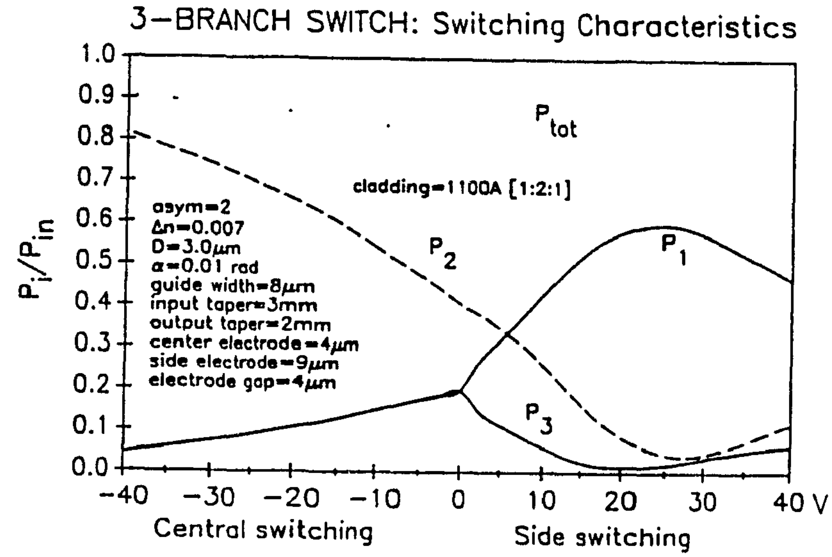

λ=1.32μm

(d)

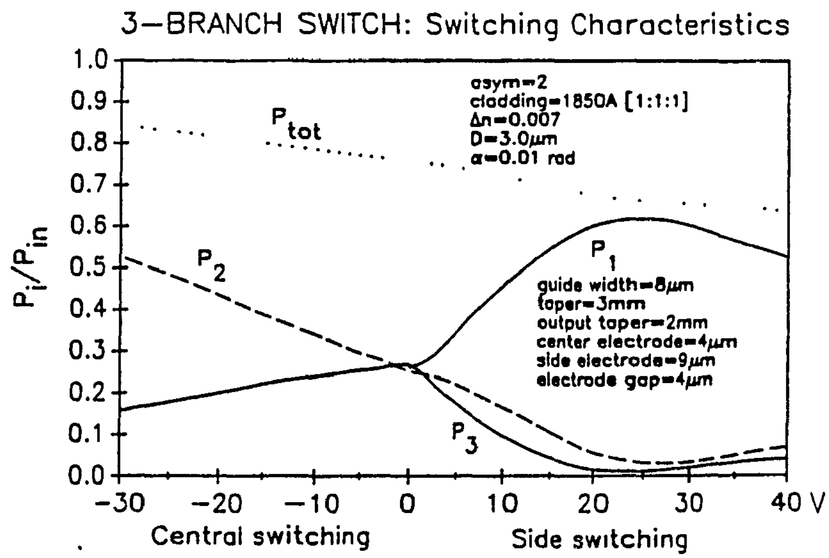

Figure V-9 *Switching characteristics for an asymmetric switch (asym=2) design with a power division ratio of (c) [1:2:1] and (d) [1:1:1].*

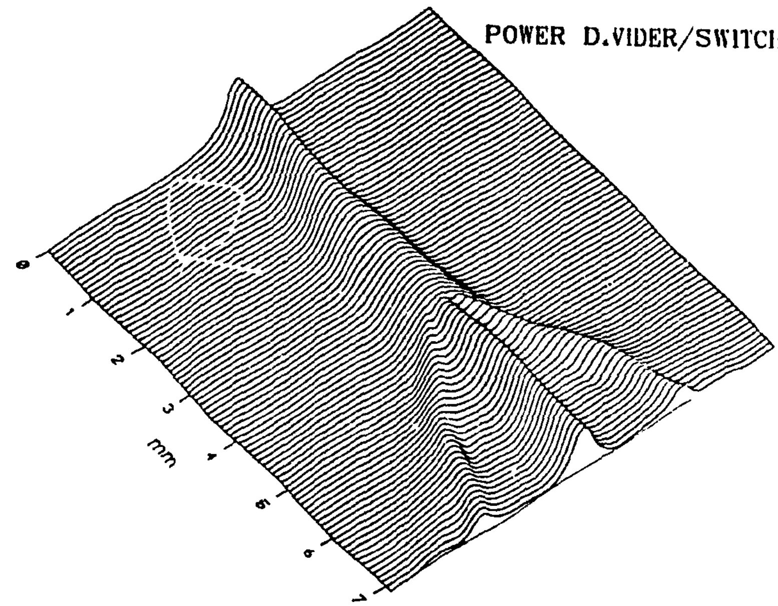

Figure V-10 *Optical field evolution in the switch for zero volts applied to the electrodes.*

(a)

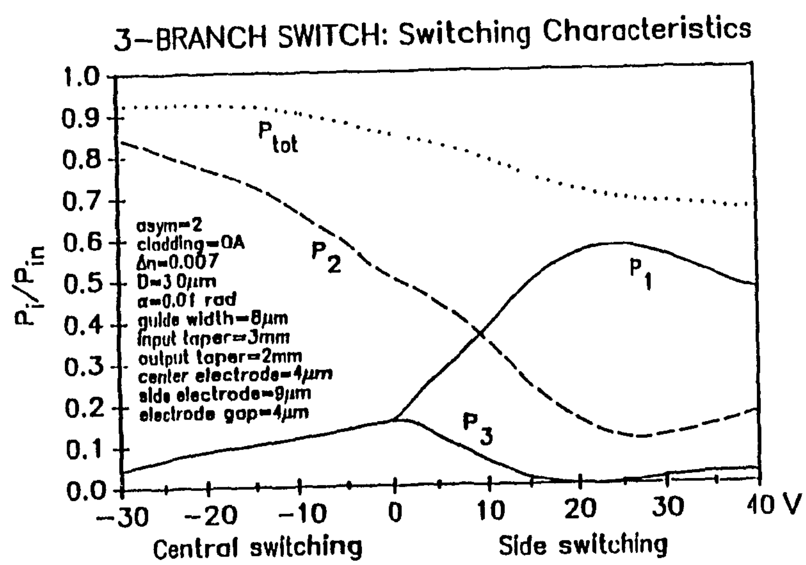

λ=1.32μm

Figure V-11 *Switching characteristics for an asymmetric switch (asym=2) design with a center electrode width of (a) 4μm.*

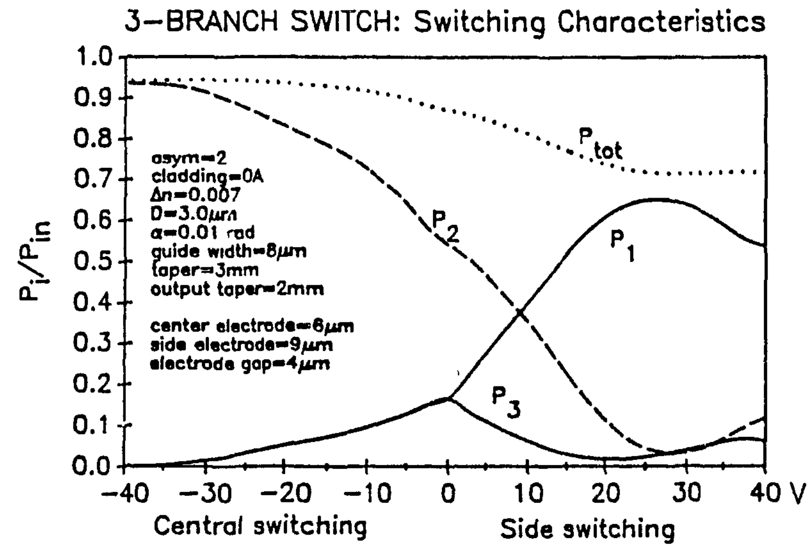

(b)

λ=1.32μm

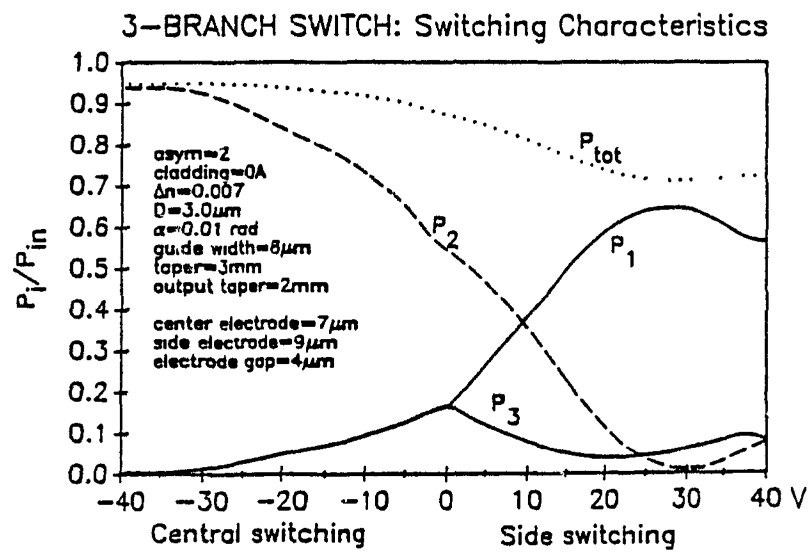

(c)

Figure V-11 *Switching characteristics for an asymmetric switch (asym=2) design with a center electrode width of (b) 6μm and (c) 7μm.*

(a)

(b)

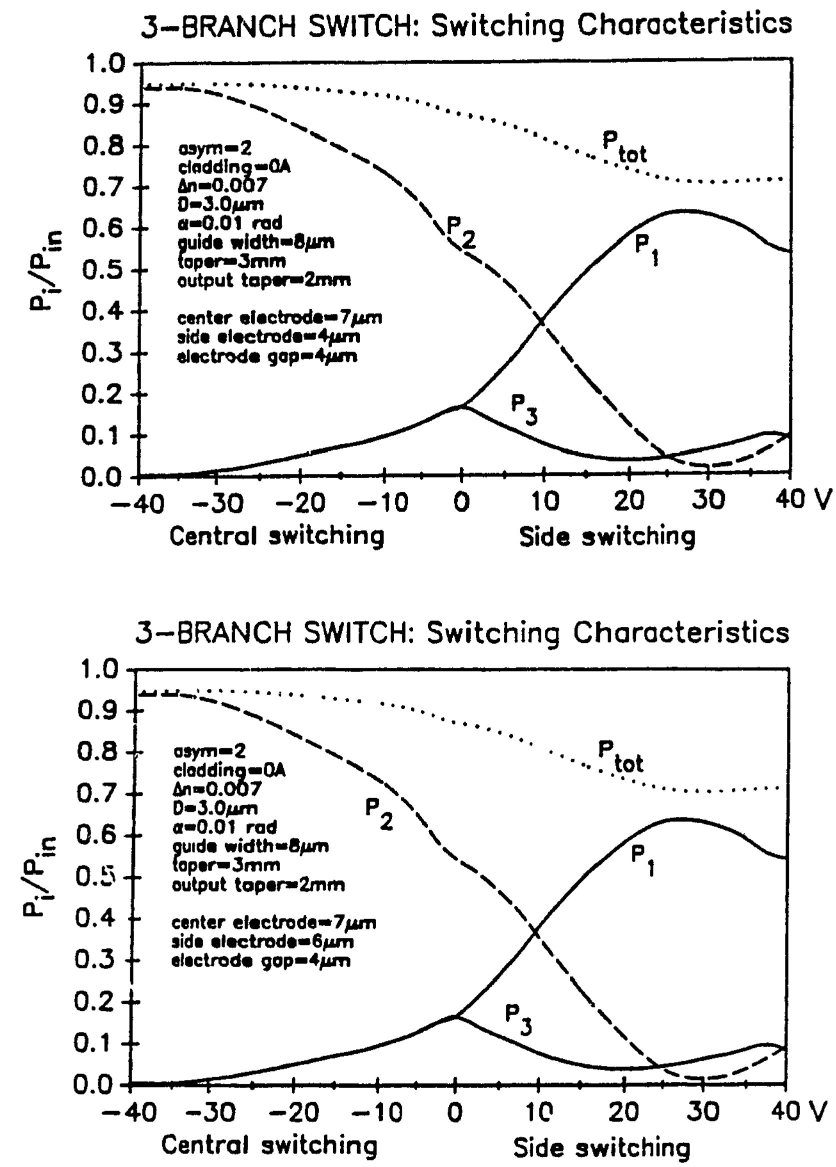

λ=1.32μm

Figure V-12 *Switching characteristics for an asymmetric switch (asym=2) design with a side electrode width of (a) 4μm and (b) 6μm.*

(c)

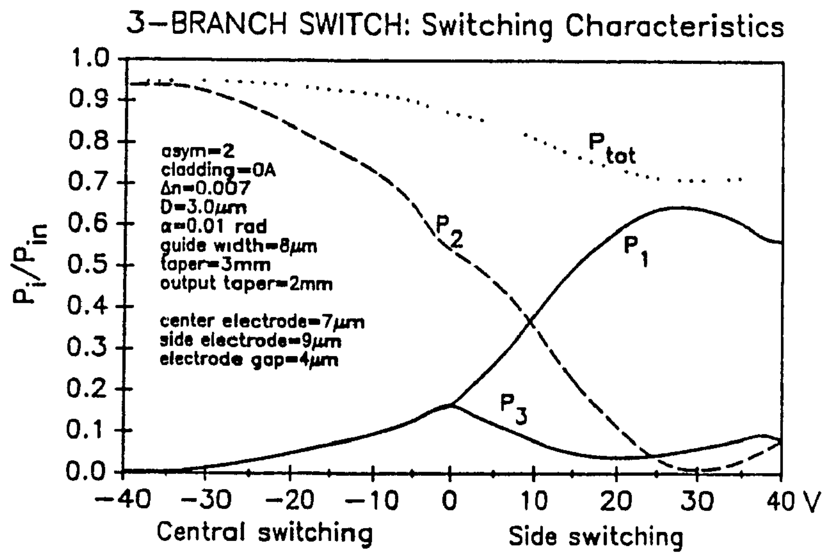

λ=1.32μm

(d)

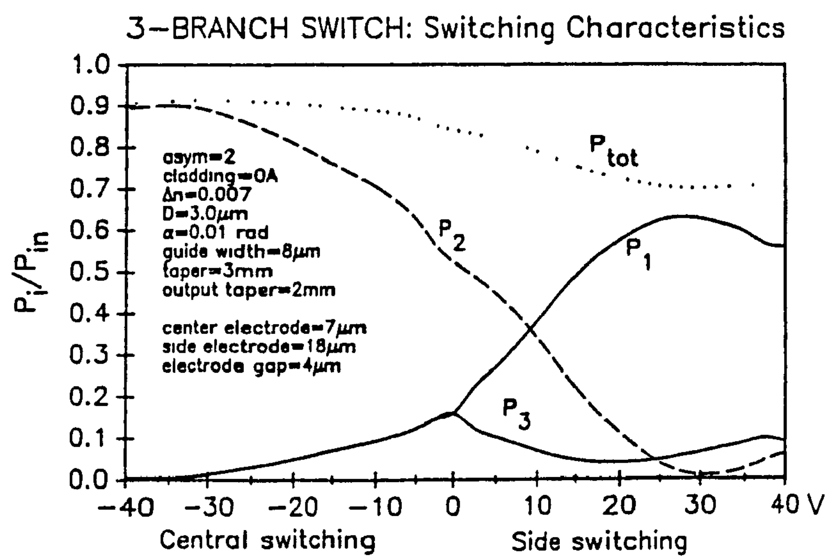

Figure V-12 *Switching characteristics for an asymmetric switch (asym=2) design with a side electrode width of (c) 9μm and (d) 18μm.*

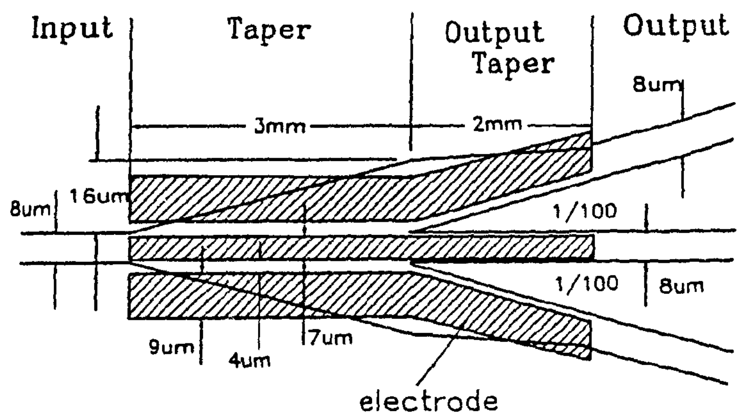

Figure V-13 *(a) Optimized device configuration (Characterisics given as Fig.* V-12c).

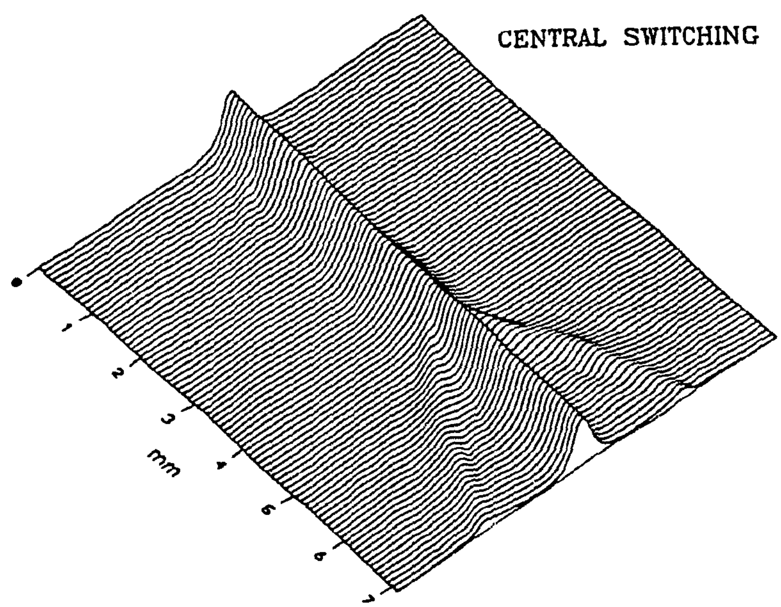

Figure V-13 *(b) Optical field evolution in switch for central switching.*

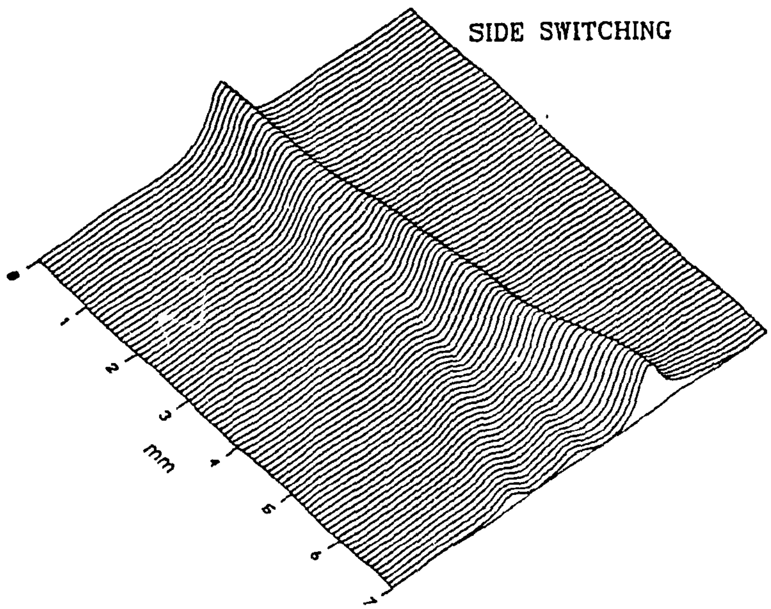

Figure V-13 *(c) Optical field evolution in switch for side switching.*

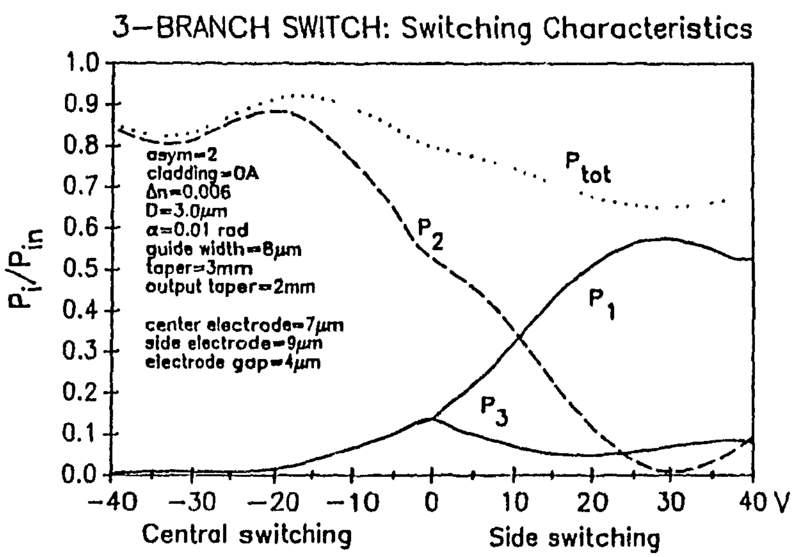

Figure V-13 *(d) Switching behavior of the optimized device design for a* Δn_s *of* 0.006.

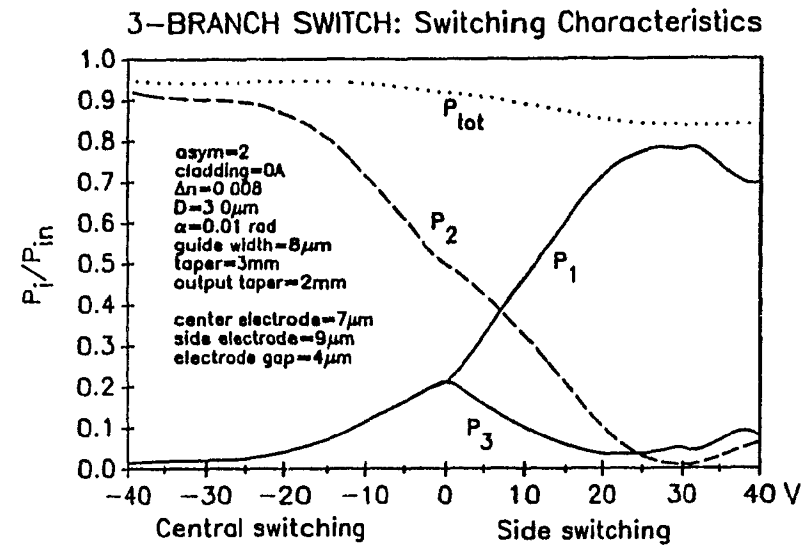

Figure V-13 *(e) Switching behavior of the optimized device design for a* Δn_s *of* 0.008.

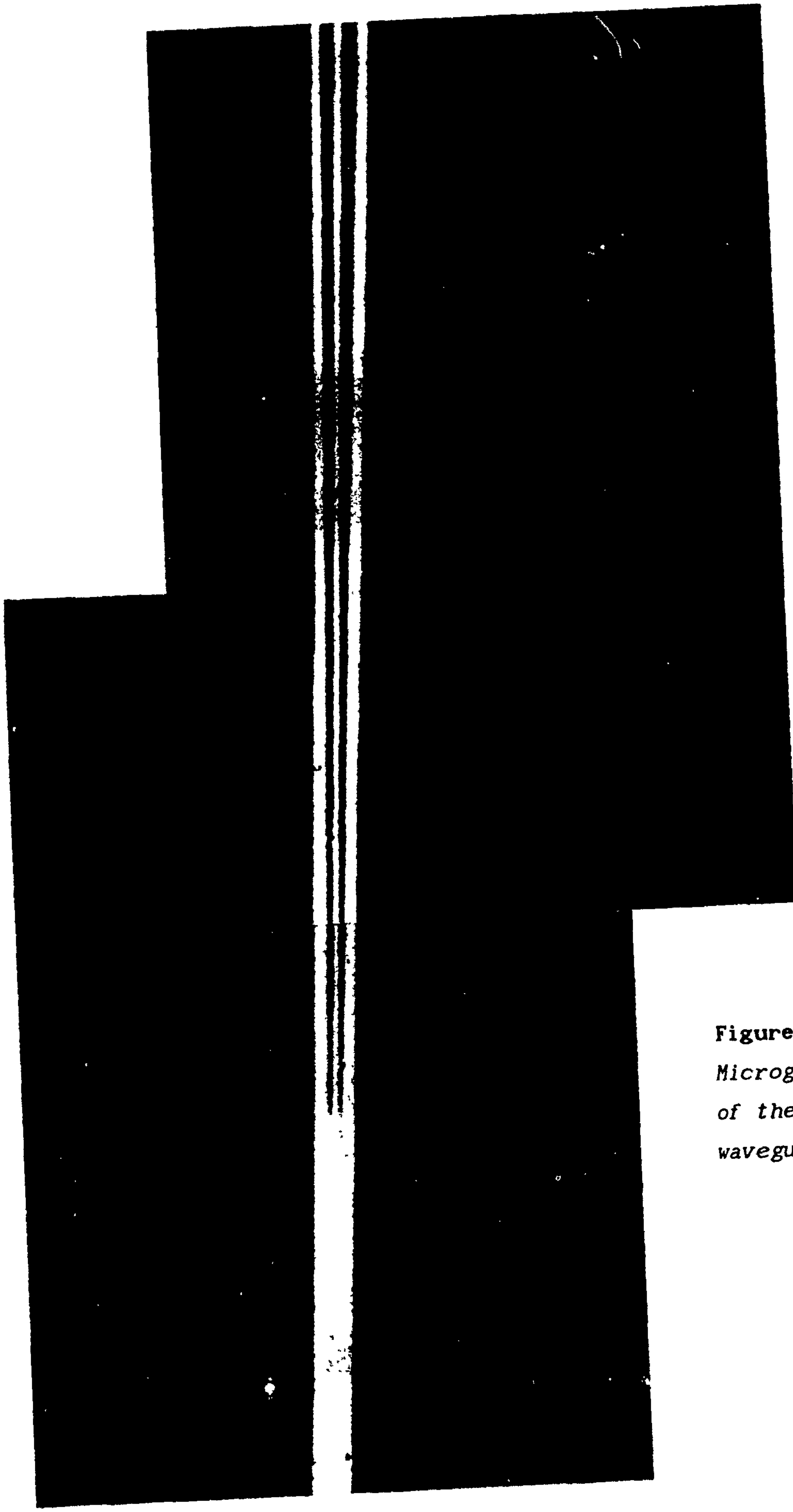

Figure V-14
Micrograph of the titanium waveguide pattern.

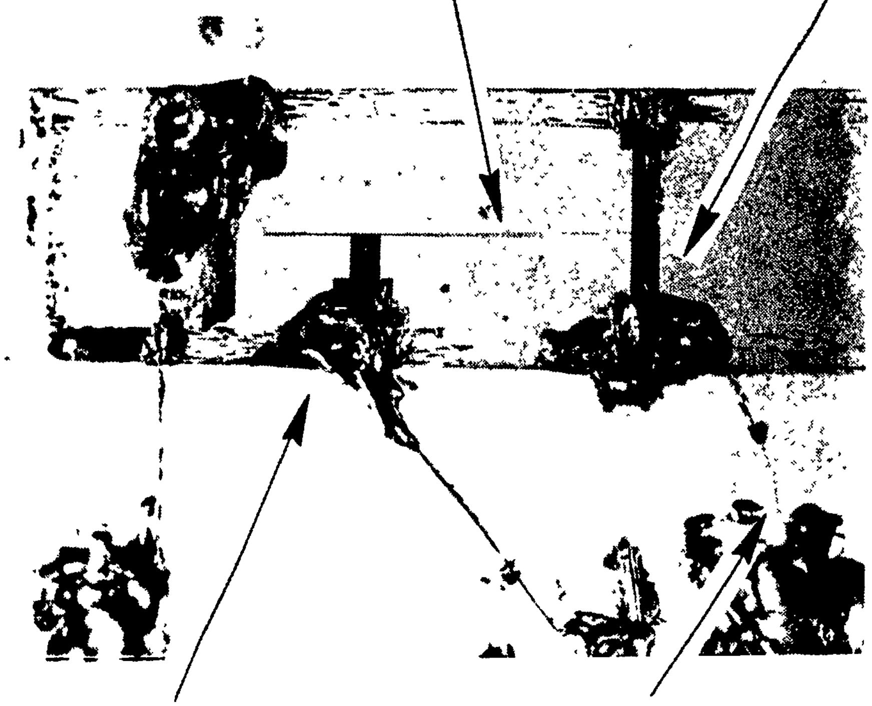

Figure V-15 *Micrograph of the mounted device.*

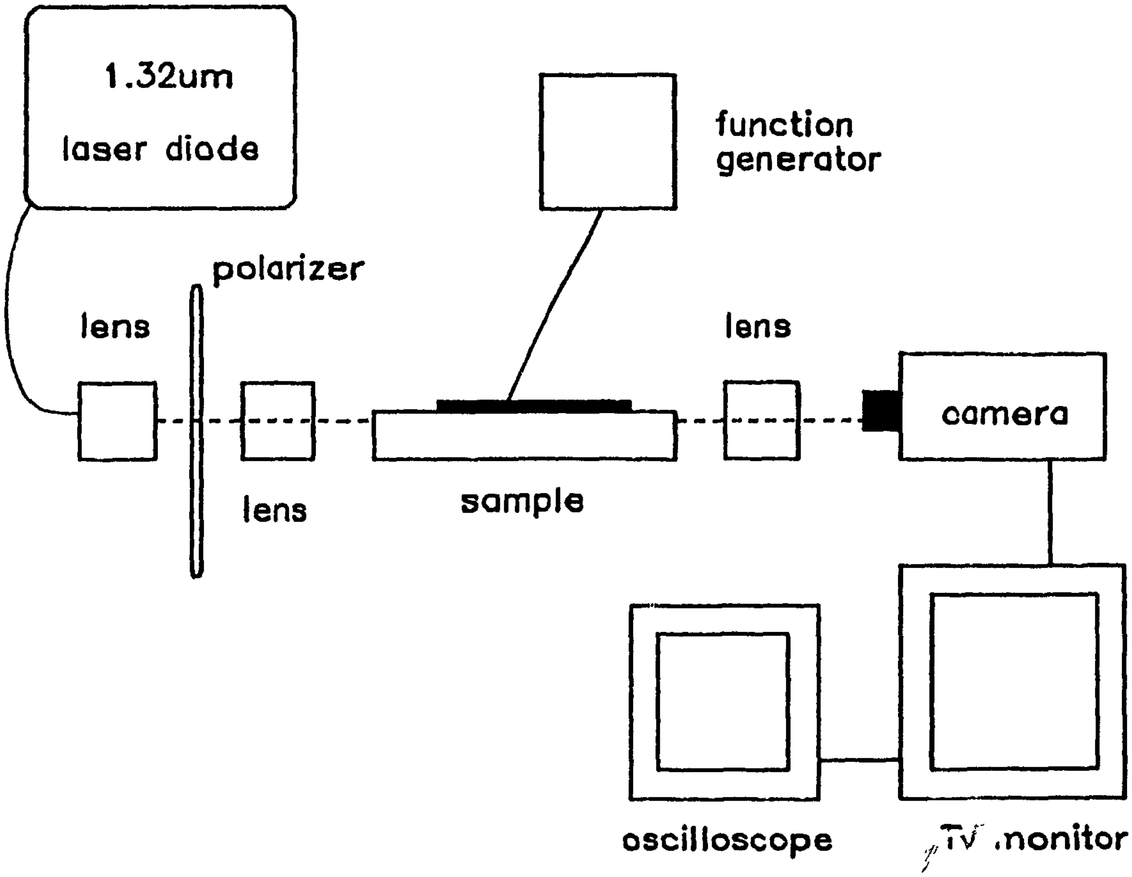

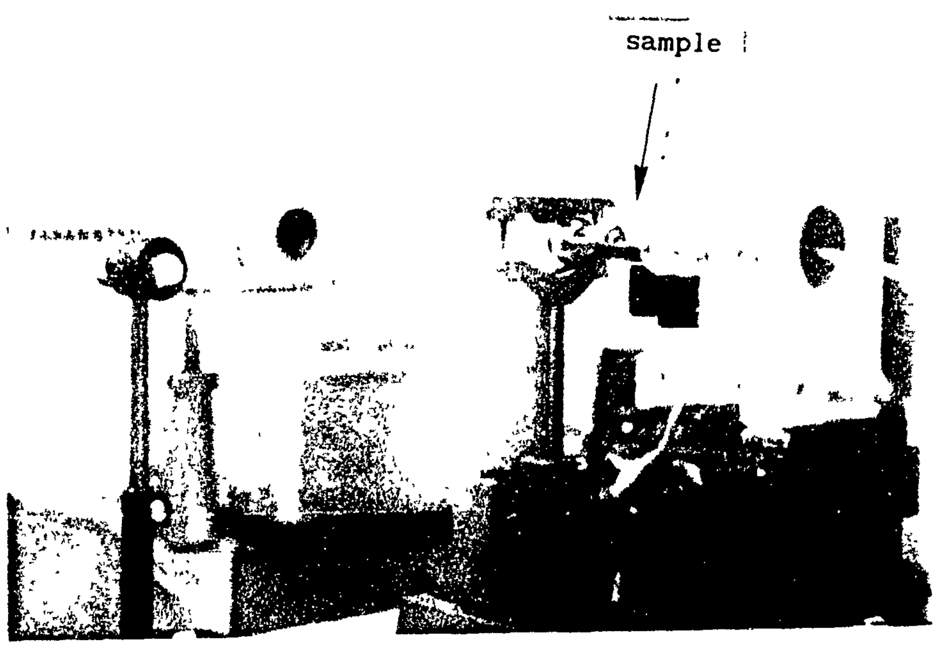

Figure V-16 *Experimental setup.*

(a) U=20V

U=12V

(b)

Figure V-17 *Near field light spots and corresponding intensity scans for (a) central switching and (b) side switching at* λ=0.6328μm.

Figure V-17 *Near field light spots and corresponding intensity scans for (c) the neutral state at λ=0.6328μm.*

U=±15V

(a)

U=±15V

(b)

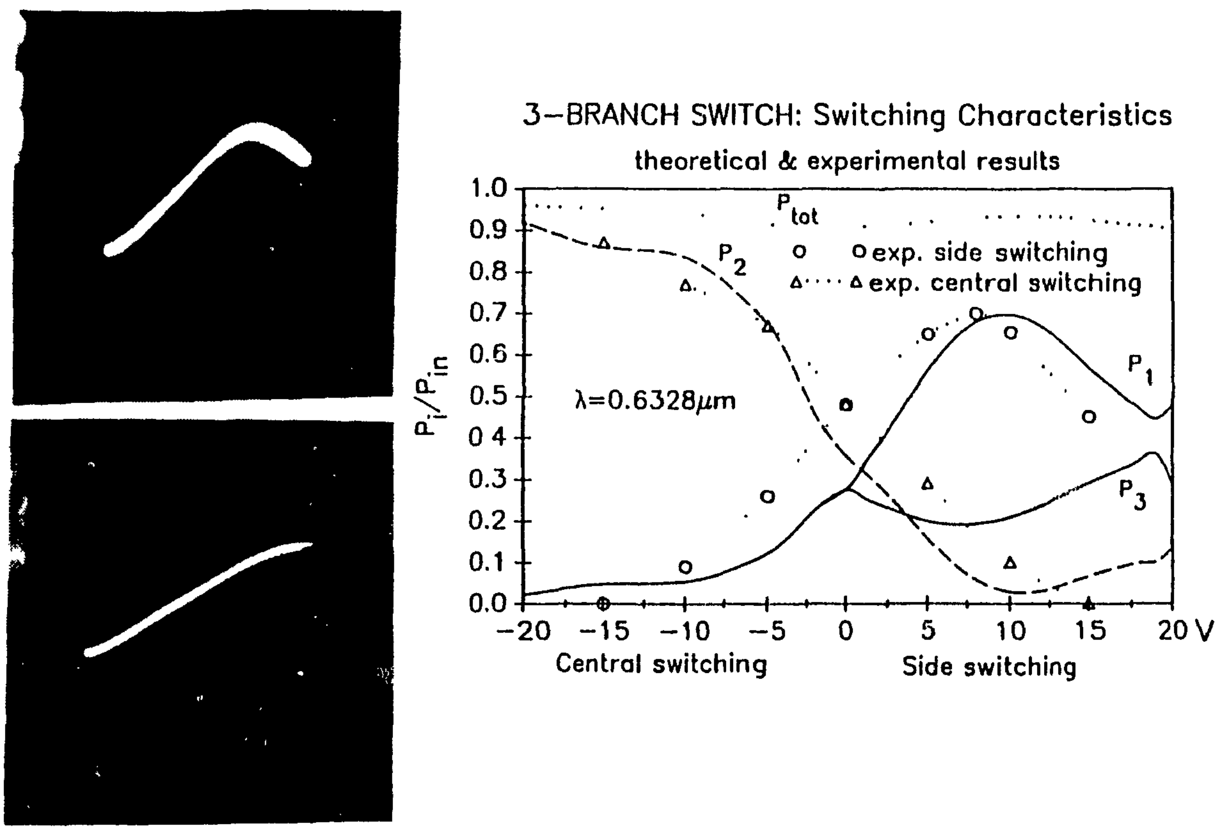

Figure V-18 *Measured switching characteristics, together with the theoretical results, for (a) side switching and (b) central switching for the fabricated device (Table V-5).*

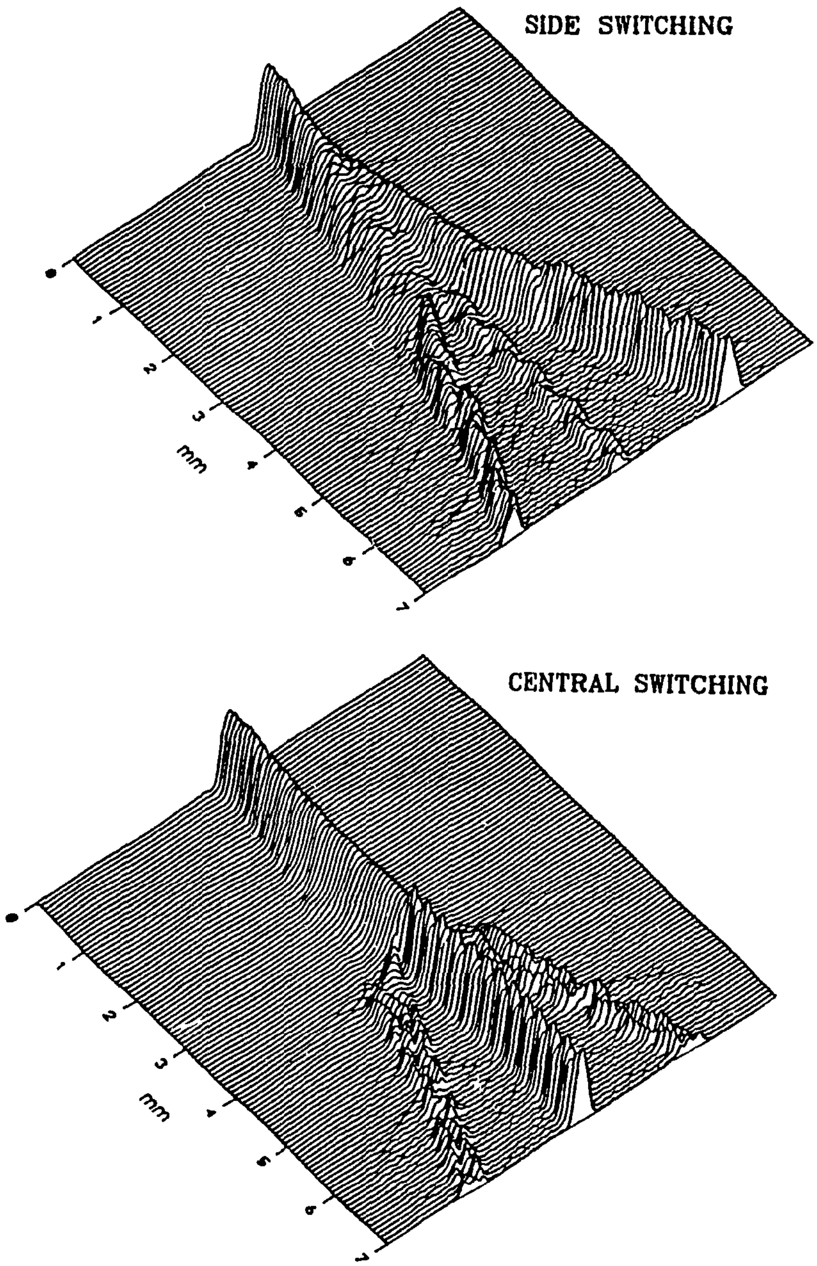

Figure V-19 *Optical field distribution in the device for both voltage states at* λ=0.6328μm.

(a)

(b)

(c)

(d)

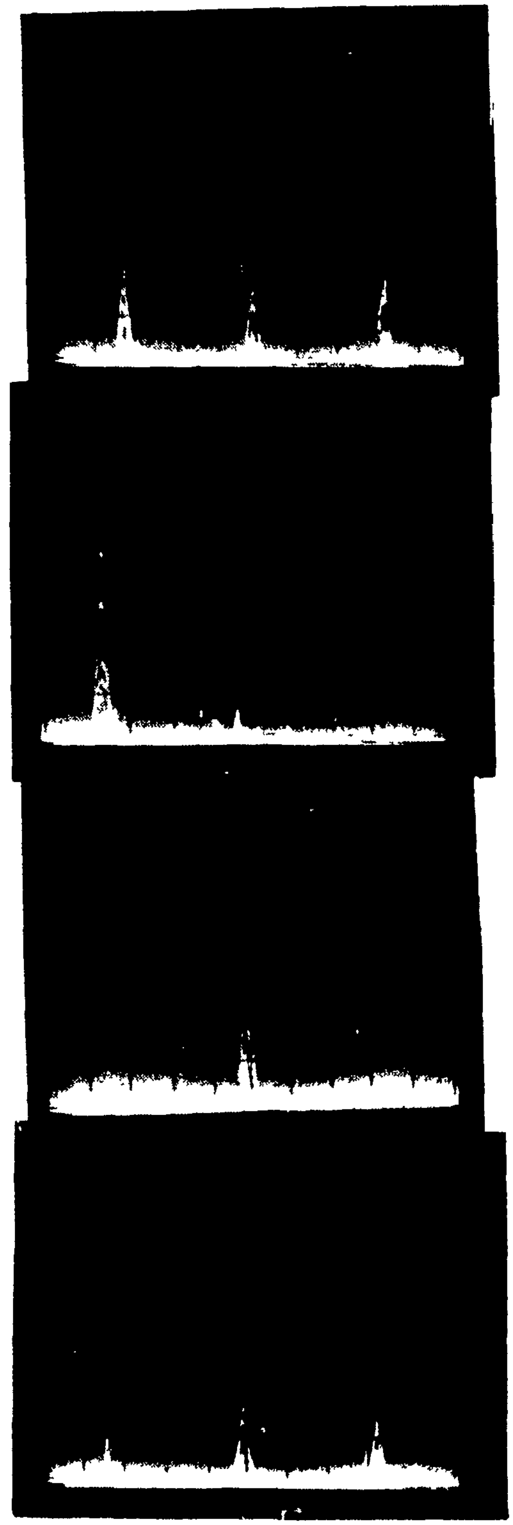

Figure V-20 *Light intensity scans for (a) the neutral state, (b) side switching (left)* U=32V, *(c) central switching* U=35V, *and (d) side switching (right)* U=35V *at* λ=1.32μm.

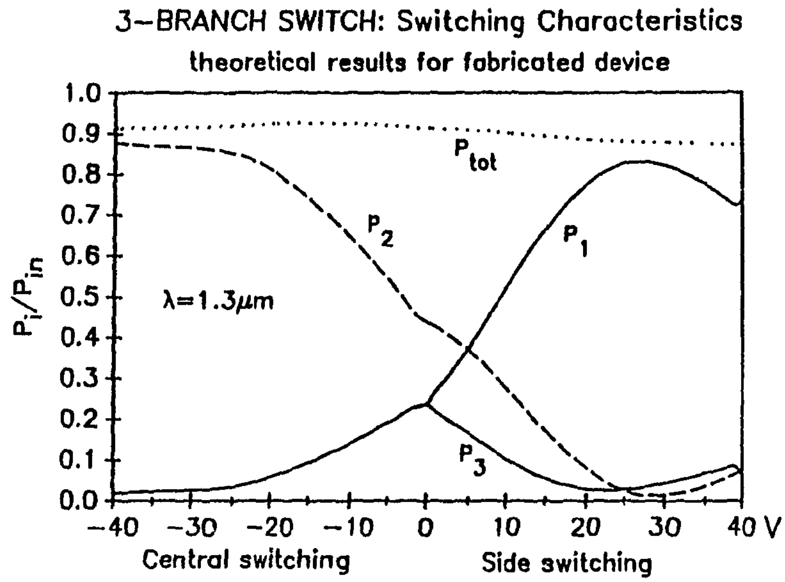

Figure V-21 *Theoretical switching characteristics for the fabricated device at λ=1.32μm.*

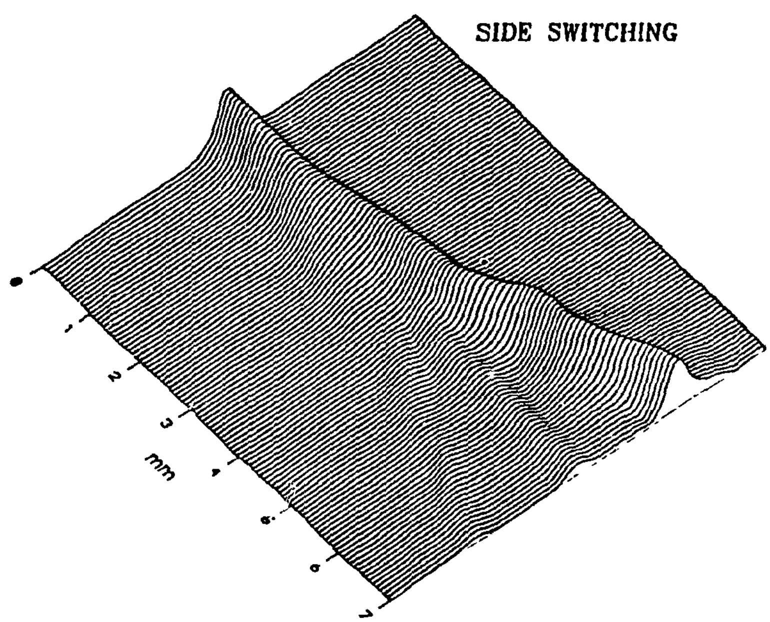

Figure V-22 *Optical field distribution in the device for (a) side switching at λ=1.32μm.*

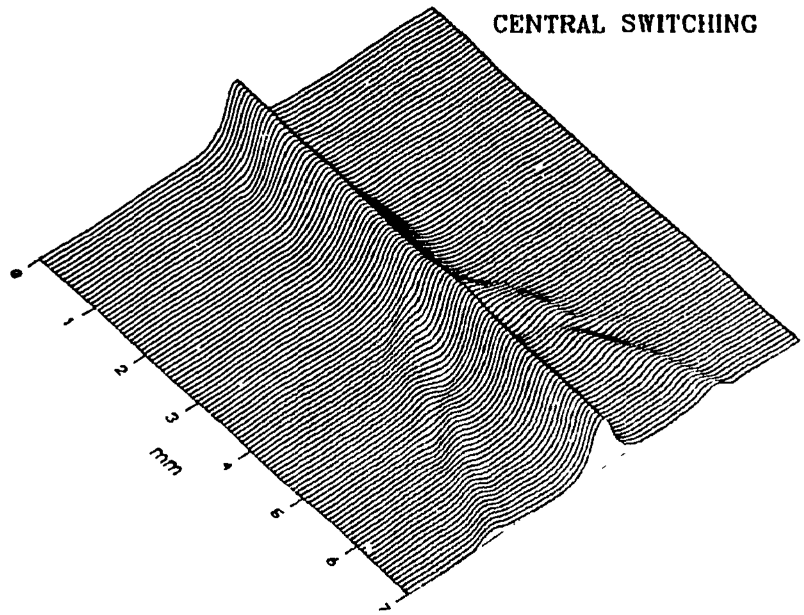

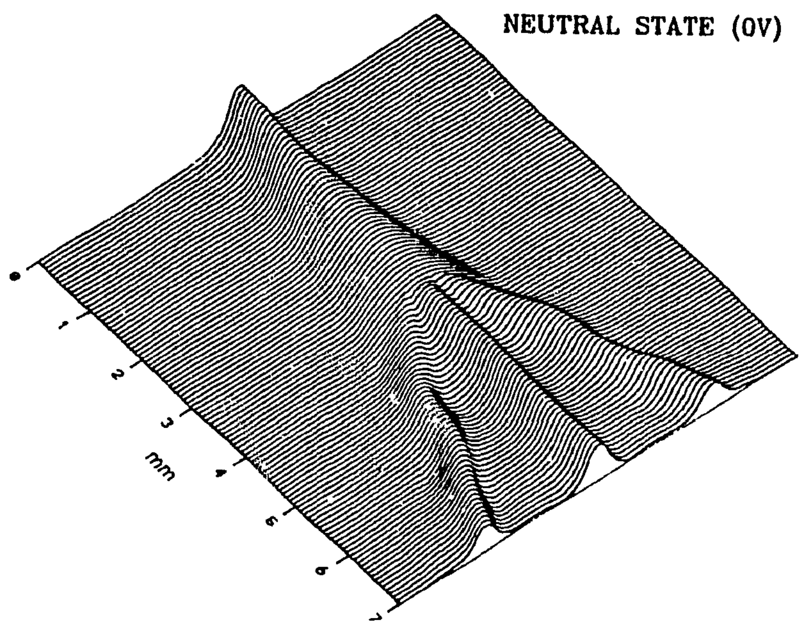

Figure V-22 *Optical field distribution in the device for (b) central switching and for (c) the neutral state at* λ=1.32μm.

CHAPTER VI. DISCUSSION AND CONCLUSION

The goal of this thesis was to develop a sophisticated theoretical model for the design oriented analysis and optimization of integrated optical (IO) devices. The accuracy and applicability of the new design tool was then demonstrated by studying 3-branch active and passive waveguide devices. The resulting optimized designs led to a substantial experimental improvement of the device performance over previously obtained results.

The theoretical design tool was realized by using the novel *Beam Propagation Method* together with an accurate *Effective Index* modelling of the IO structure. The modelling of active devices was further improved by using a new method of solving the electrode problem which accounts for the attenuating effect of the low-index buffer layer between the metal electrodes and the substrate surface on the electric field.

The accuracy of the BPM approach was first established in Chapter III by comparing the theoretical performance predictions of a passive 3-branch power divider with previously published experimental results. It was demonstrated that, if accurate characterization data on the fabrication processes is available, the BPM modelling technique provides highly accurate theoretical results. The theoretical cladding thickness of 0.215μm compares extremely well with the measured value of 0.2μm for equal power division among the three branches. The BPM model is consequently well suited for design analysis and optimization purposes.

The BPM modelling technique was then used to optimize the designs of a linear mode confinement modulator and an active 3-branch switch. Good qualitative and quantitative agreement between theory and experiment was established. The experimental result for a multi-mode ridge waveguide modulator was improved to a modulation depth of 97% and a drive voltage of only -8V to +8V. This improvement in the experimental performance over the results reported earlier is mainly due to a reduced buffer layer thickness and an optimization of the ridge height. The BPM design procedure was also used to redesign the line modulator for single-mode operation. The resulting smaller modulator with a 6μm guide width and an optimized geometry has a theoretical modulation depth of 95% and a drive voltage of ±5V. Experimental results for this device are, however, not available.

In the same manner, the 3-branch optical switch was redesigned for single-mode operation at 1.32μm. An asymmetry in the branch structure was used to overcome the central switching bias observed for an earlier device based on a symmetric branch design. The new device exhibited power extinction ratios of 15.9dB (P_1/P_2) and 20.1dB (P_1/P_3) for side switching at 32V, and of 16.1dB ($P_2/P_{1,3}$) at 35V for central switching at 1.32μm. These results compare favorably to the theoretically predicted values. The central switching bias of the earlier device has been overcome with the new design.

The device performance was also measured at 0.6328μm. Power extinction ratios of >25dB (P_1/P_2) and 15.6dB (P_1/P_3) were obtained at 12V for the side switching condition. A poorer performance of 13.6dB

($P_2/P_{1,3}$) at 20V was measured for central switching. This result is consistent with the results of the BPM analysis which predicted a much improved side switching performance at the expense of poorer central switching for a switch design based on an equal power divider. The experimental performance of the new switch at 0.6328µm constitutes a considerable improvement over the previous device (Chap.V, [5]), particularly for the side switching state.

The work presented in this thesis has demonstrated the usefulness and accuracy of the Beam Propagation method for design oriented research in integrated optics. The method is extremely versatile, allowing the modelling of a large variety of IO devices. The computer software is easily adapted to simulate new device configurations since the BPM routines used to propagate the optical field remain unchanged and only those sections of the program which calculate the effective index model have to be modified. The software package generated for this work was designed to accommodate such changes easily. The BPM modelling technique and the corresponding software can thus be considered a Computer Aided Design (CAD) tool for future use in our laboratory.

The success of the BPM simulations is, however, critically dependent on the availability of reliable characterization data on the different fabrication techniques used to realize the IO device. As was demonstrated in Chapter III, if accurate characterization data is available, excellent quantitative correspondence between the BPM simulation and the experimental results can be obtained. This is particularly important if the BPM is to find application as a CAD tool for the commercial design of IO devices.

The accuracy of the modelling technique used in this thesis could be further improved by accounting for lateral diffusion in the effective index modelling of diffused waveguides. Sideway diffusion was neglected in this work because only limited characterization data on the diffusion process was available. A detailed characterization of titanium diffusion into $LiNbO_3$ at wavelengths between 1.1μm and 1.52μm is necessary if further device optimization work is to be pursued at these wavelengths.

The device design optimization presented in Chapters IV and V was based on pure device performance considerations such as drive voltage, modulation depth, and power extinction ratios. The problem of efficient fiber to waveguide coupling and a minimization of the corresponding device coupling/insertion loss was only briefly touched on in Chapter V. Insertion loss considerations for a fiber system oriented device design will have to be included in the design process. In particular, the constraints on the diffused waveguide design dictated by the need to optimize the modal field matching between the fiber mode and the planar waveguide mode will establish further limitations on the device design and its performance. Possible trade-offs between the insertion loss, drive voltage, and device dimensions will have to be considered on an individual basis, depending on the fiber system requirements.

In summary, a sophisticated theoretical design tool based on the *Beam Propagation* and *Effective Index Methods* was used for the design oriented analysis of 3-branch waveguide devices and their derivatives. Good qualitative and quantitative agreement between theory and experiment was established, indicating the suitability of this IO modelling technique for the optimization of integrated optical devices.